

**DAMAGE DETECTION IN CONCRETE USING  
DIFFUSE ULTRASOUND MEASUREMENTS AND AN  
EFFECTIVE MEDIUM THEORY FOR WAVE  
PROPAGATION IN MULTI-PHASE MATERIALS**

A Thesis  
Presented to  
The Academic Faculty

by

Frederik Deroo

In Partial Fulfillment  
of the Requirements for the Degree  
Master of Science in Engineering Science and Mechanics in the  
School of Civil and Environmental Engineering

Georgia Institute of Technology  
December 2009

**DAMAGE DETECTION IN CONCRETE USING  
DIFFUSE ULTRASOUND MEASUREMENTS AND AN  
EFFECTIVE MEDIUM THEORY FOR WAVE  
PROPAGATION IN MULTI-PHASE MATERIALS**

Approved by:

Dr. Laurence Jacobs, Advisor  
School of Civil and Environmental  
Engineering  
*Georgia Institute of Technology*

Dr. Jin-Yeon Kim  
School of Civil and Environmental  
Engineering  
*Georgia Institute of Technology*

Dr. Jianmin Qu  
George W. Woodruff School of Mechanical  
Engineering  
*Georgia Institute of Technology*

Date Approved: August 14, 2009

## ACKNOWLEDGEMENTS

Without the help and support from a large number of people, this work would not have been possible.

First of all, I would like to thank Prof. Laurence Jacobs for making this exchange possible and for being a great advisor, supporter, teacher and friend. He opened a new door to ultrasonic wave propagation I might not have entered without him.

A huge 'Thank You' goes to Dr. Jin-Yeon Kim for his advice on experimental procedures and the sharing of his knowledge, but just as important for his moral support when times were not so bright.

I also want to express my gratitude to Prof. Dr.-Ing. Gaul at the University of Stuttgart for establishing this outstanding exchange program and for making my stay here at Georgia Tech possible. Also, I would like to thank Helge Sprenger at the Institut fuer Angewandte and Experimentelle Mechanik at the University of Stuttgart for organizing the exchange and his help to get through the necessary formalities to go to school on a different continent. The support of Jan Herrmann (also at the IAM) in the preparation of my stay here is also appreciated. My studies would not have been possible without the very generous financial support by the DAAD (German Academic Exchange Service).

Dr. Karim Sabra and Jun Chen deserve my gratefulness for helpful advice and support with experiments. I would also like to thank Robert Moser for supplying the samples employed in this research. Also, the people in the CEE and ME machine shop who manufactured the cones and the fixture have to be mentioned and their help is greatly appreciated.

I would like to express my gratitude to my labmates Martin Mueller, Alexander

Pertsch, Natalie Darraugh and Minghe Liu for the nice working environment and the fun we had together. Also I want to thank my friends and roommates who cheered me up when necessary and who will be missed when I leave Georgia Tech.

Last but not least, I want to express my loving gratitude to my family who always stood behind me and supported me. Their belief in me literally took me to new worlds.

# TABLE OF CONTENTS

ACKNOWLEDGEMENTS . . . . .	iii
LIST OF TABLES . . . . .	viii
LIST OF FIGURES . . . . .	ix
LIST OF SYMBOLS OR ABBREVIATIONS . . . . .	xii
SUMMARY . . . . .	xiii
I INTRODUCTION . . . . .	1
1.1 Microcrack detection using diffuse ultrasound methods . . . . .	1
1.2 Effective medium theory for multi-phase materials . . . . .	4
1.3 Outline . . . . .	4
II CEMENT-BASED MATERIALS . . . . .	6
2.1 Basic composition and properties . . . . .	6
2.2 Porosity, interfacial zone, alkali-silica reaction (ASR) and thermal damage . . . . .	7
III THEORETICAL BACKGROUND . . . . .	9
3.1 Wave propagation . . . . .	9
3.1.1 Linear elasticity and equation of motion . . . . .	9
3.1.2 Wave phenomena . . . . .	12
3.1.3 Harmonic waves . . . . .	13
3.1.4 Reflection and Transmission of 1D waves . . . . .	13
3.1.5 Reflections of 2D P- and SV-waves . . . . .	14
3.2 Attenuation . . . . .	16
3.2.1 Viscoelastic material behavior - Absorption . . . . .	17
3.2.2 Geometric spreading . . . . .	18
3.2.3 Scattering . . . . .	18
IV ULTRASOUND DIFFUSION APPROXIMATION . . . . .	20
4.1 Diffuse approximation and its governing equation . . . . .	21

4.1.1	Definitions . . . . .	23
4.1.2	Identification of the coefficients . . . . .	23
4.1.3	Special solutions of the diffusion equation . . . . .	24
V	EFFECTIVE MEDIUM THEORY (EMT) FOR MULTI-PHASE MATERIALS . . . . .	27
5.1	General scheme . . . . .	29
5.1.1	Solution of the one-particle problem . . . . .	31
5.1.2	Numerical solution . . . . .	36
VI	EXPERIMENTAL PROCEDURE FOR DIFFUSE MEASUREMENTS . . . . .	38
6.1	Signal generation . . . . .	38
6.2	Received signal amplification . . . . .	39
6.3	Source/receiver transducer . . . . .	40
6.4	Waveform acquisition . . . . .	40
6.4.1	Signal-to-noise ratio (SNR) and averaging . . . . .	42
6.4.2	Sampling rate and record length . . . . .	43
6.5	Specimens . . . . .	43
6.5.1	Description . . . . .	43
6.5.2	Impedance mismatch . . . . .	46
VII	RESULTS . . . . .	48
7.1	Diffusion approximation . . . . .	48
7.1.1	Measurement setup description . . . . .	50
7.1.2	Simulation of the energy density evolution $\langle E(x, t, f) \rangle$ . . . . .	50
7.1.3	Calculation of the energy density evolution $\hat{E}(x, t, f)$ from measurement data . . . . .	53
7.1.4	Estimation of the expected fluctuations . . . . .	55
7.1.5	2D Semi-infinite plate . . . . .	57
7.1.6	Model accuracy . . . . .	59
7.1.7	Finite 3D cuboid . . . . .	69
7.1.8	Conclusions . . . . .	75

7.2	Velocity measurements . . . . .	77
7.2.1	Measurement setup description . . . . .	78
7.2.2	Calculation of the velocity . . . . .	78
7.2.3	Conclusion . . . . .	79
7.3	Effective medium theory . . . . .	79
7.3.1	Two-phase composite . . . . .	79
7.3.2	Concrete as a multi-phase composite . . . . .	82
VIII	CONCLUSIONS AND OUTLOOK . . . . .	85
8.1	Diffuse measurements . . . . .	85
8.1.1	Conclusion . . . . .	85
8.1.2	Outlook . . . . .	86
8.2	Effective medium theory . . . . .	87
8.2.1	Conclusion . . . . .	87
8.2.2	Outlook . . . . .	88
	REFERENCES . . . . .	89

## LIST OF TABLES

2.1	Typical properties of concrete . . . . .	7
3.1	Angle relations for reflection on a stressfree surface . . . . .	16
6.1	Mix design for concrete samples . . . . .	45
6.2	Gradation of fine aggregate . . . . .	46
6.3	Gradation of coarse aggregate . . . . .	46
6.4	Acoustic properties of concrete constituents . . . . .	46
7.1	Time windows for 2D curve fit . . . . .	59
7.2	Weighting intervals for 3D curve fit . . . . .	70
7.3	Velocities of ASR damaged samples . . . . .	79
7.4	Material properties for lead/epoxy composite . . . . .	80

## LIST OF FIGURES

3.1	Momentum balance of arbitrary volume $V$ . . . . .	9
3.2	Reflected and transmitted 1D wave . . . . .	13
3.3	Wave reflections . . . . .	15
5.1	Illustration of Kanaun’s self-consistency approach . . . . .	28
5.2	Illustration of this research’s self-consistency approach . . . . .	28
6.1	Receiving transducer with cone . . . . .	41
6.2	Fixture for receiving transducer . . . . .	41
6.3	Fixture clamped to sample with receiving transducer . . . . .	41
6.4	Expansion data of ASR damaged concrete samples . . . . .	44
7.1	Setup for diffuse ultrasound measurement . . . . .	49
7.2	Simulation of the energy density evolution with the infinite plate solution	51
7.3	Simulation of the energy density evolution with the finite cuboid solution	52
7.4	Typical timesignal of diffuse measurement . . . . .	53
7.5	Hanning window . . . . .	55
7.6	Curve fit with the semi-infinite model with the expected deviation as bars . . . . .	60
7.7	Curve fit with the semi-infinite model with the expected deviation as bars . . . . .	61
7.8	Curve fit with the semi-infinite model with the expected deviation as bars . . . . .	62
7.9	Diffusivity $D$ for two ASR damaged samples with same damage level with 2D semi-infinite plate model . . . . .	65
7.10	Dissipation $\sigma$ for two ASR damaged samples with same damage level with 2D semi-infinite plate model . . . . .	65
7.11	Diffusivity $D$ for ASR damaged samples with 2D semi-infinite plate model . . . . .	66
7.12	Dissipation $\sigma$ for ASR damaged samples with 2D semi-infinite plate model . . . . .	66
7.13	Diffusivity $D$ for thermal damaged samples with 2D semi-infinite plate model . . . . .	67

7.14	Dissipation $\sigma$ for thermal damaged samples with 2D semi-infinite plate model . . . . .	67
7.15	Curve fit with the finite model with the expected deviation as bars for 0.635 MHz . . . . .	70
7.16	Curve fit with the finite model with the expected deviation as bars . . . . .	71
7.17	Curve fit with the finite model with the expected deviation as bars . . . . .	72
7.18	Diffusivity $D$ for ASR damaged samples with 3D finite cuboid model . . . . .	73
7.19	Dissipation $\sigma$ for ASR damaged samples with 3D finite cuboid model . . . . .	74
7.20	Diffusivity $D$ for thermal damaged samples with 3D finite cuboid model . . . . .	74
7.21	Dissipation $\sigma$ for thermal damaged samples with 3D finite cuboid model . . . . .	75
7.22	Setups for velocity measurement . . . . .	77
7.23	Effective longitudinal wave speed versus frequency for lead/epoxy (5% volume fraction) composite and experimental data by Kinra et al. . . . .	80
7.24	Coherent attenuation of longitudinal wave speed versus frequency for lead/epoxy (5% volume fraction) composite . . . . .	81
7.25	Effective longitudinal wave speed versus frequency for lead/epoxy (15% volume fraction) composite and experimental data by Kinra et al. . . . .	81
7.26	Coherent attenuation of longitudinal wave speed versus frequency for lead/epoxy (15% volume fraction) composite . . . . .	81
7.27	Longitudinal wave speed of concrete specimen 1 . . . . .	83
7.28	Attenuation of concrete specimen 1 . . . . .	83
7.29	Longitudinal wave speed of concrete specimen 2 . . . . .	83
7.30	Attenuation of concrete specimen 2 . . . . .	84
7.31	Longitudinal wave speed of concrete specimen 3 . . . . .	84
7.32	Attenuation of concrete specimen 3 . . . . .	84

## LIST OF SYMBOLS OR ABBREVIATIONS

NDE	Nondestructive evaluation
EMT	Effective medium theory
ASR	Alkali-silica reaction
MK	Metakaolin
FA	Fly-ash
w/cm	Water/cement ratio
$D$	Diffusivity coefficient
$\sigma$	Dissipation coefficient
$E$	Young's modulus
$\nu$	Poisson's ratio
$\rho$	Density
$\lambda, \mu$	Lamé constants
$K$	Bulk modulus
$\mathbf{t}; t_i$	traction per unit area
$\sigma; \sigma_{ij}$	stress tensor
$\epsilon; \epsilon_{ij}$	strain tensor
$\mathbf{u}; u_i$	particle displacement vector
$\mathbf{n}; n_i$	outward unit normal vector
$\mathbf{f}; f_i$	body force per unit mass
$V$	Volume
$S$	Surface, $\partial V$
$\delta_{ij}$	Kronecker delta
$\nabla$	Nabla operator
$\phi, \psi$	Potential functions

$c, c_L, c_T$	Wave speeds
$k, k_L, k_T$	Wave numbers
$\mathbf{p}; p_i$	Direction of wave propagation unit vector
$\mathbf{d}; d_i$	Direction of particle motion unit vector
$f$	Frequency
$\omega$	Circular frequency
$Z$	Acoustic impedance
$R$	Reflection coefficient
$T$	Transmission coefficient
$\tilde{k}$	Complex wavenumber
$\alpha$	Wave attenuation coefficient
$a$	Scatterer size
$E$	Spectral energy density
$P$	Spectral source energy density
$\langle \cdot \rangle$	Expected value operator
$C$	Stiffness tensor
$G$	Green's function
$\Lambda$	Linear operator
$L$	Differential operator
$a_n, b_n, c_n, d_n, e_n$	Coefficients of scattered field
$a'_n, b'_n, c'_n, d'_n, e'_n$	Coefficients of transmitted field
$f_s$	Sampling frequency

## SUMMARY

Heterogeneities in concrete caused by the random distribution of aggregate in the cement-paste matrix lead to strong scattering of ultrasonic waves at wavelengths on the order of the aggregate. Use of these high frequencies is necessary to detect damage at an early stage, something that is not possible with conventional ultrasonic methods. The ultrasound energy density in this regime can be described by the diffusion equation. The objective of this research is to develop a quantitative understanding of the effects of additional scattering sources, such as small cracks in the cement-paste matrix, on the parameters of the diffusion equation; these parameters are the diffusion and the dissipation coefficients. Experimentally measured ultrasonic waves are processed using the diffusion theory to determine the diffusivity and the dissipation coefficients as a function of frequency. The samples employed are made of a Portland cement-paste matrix and regular aggregate such as gravel and sand. The results provide a basic understanding of the repeatability and consistency of diffusion measurements, with an emphasis on the nondestructive evaluation of damage in concrete.

In addition, a method to describe concrete in the coherent regime is examined. Existing wave propagation models for inhomogeneous materials deal with two-phase mixtures, mostly the matrix-inclusion system such as fiber-reinforced composites. There are, however, numerous examples of multi-phase materials in which more than one phase is suspended in a matrix-phase. This research considers concrete, in which cement paste and aggregates with different sizes and mechanical properties are mixed together. Most of the models for two-phase composites cannot be extended to a multi-phase composite. Among others, the effective medium theory is considered

here for two reasons: first, the formalism in this theory can easily be extended to multi-phase cases; second, the theory does not strictly define a specific microstructure between phases, which allows for a simulation of the microstructure in which different inclusions are in contact. The mathematical formulation is presented that yields the formulae for the effective density and the effective bulk and shear moduli. Finally, the calculated wave speeds and attenuations for different materials are compared with experimental results.

# CHAPTER I

## INTRODUCTION

Ultrasonic waves propagating through heterogeneous materials with multiple length scales are subject to scattering. The degree of scattering depends on the ratio of the ultrasonic wavelength to the size of the scatterers. This ratio divides ultrasonic wave propagation into several domains, all of which are important for different practical applications, especially in the nondestructive evaluation (NDE) of materials. Since the scattering leads to very complicated waveforms, which make traditional coherent ultrasonic nondestructive evaluation techniques difficult to apply to concrete and other heterogeneous materials, current research concentrates on developing simplifying models of the behavior of the ultrasonic waves. There are two important, but very different approaches, both of which will be investigated in this thesis.

The first approach, the diffuse method, embraces the scattering of the waves – the method even requires it – and is applied when the wavelength and the size of the scatterer are on the same order.

The second idea – the effective medium theory (EMT) – forms a theoretical model of the material that transforms the heterogeneous material into an effective homogeneous material with on average, identical properties. This EMT method is applied when wavelengths are much larger than scatterers.

### ***1.1 Microcrack detection using diffuse ultrasound methods***

The quantitative nondestructive evaluation of cement-based materials is critical for the development of advanced inspection techniques for the civil infrastructure. The prevalence of concrete structures such as roads, bridges, dams and buildings signify the importance of nondestructive evaluation of concrete structures. Detecting damage

at a very early stage will drastically reduce maintenance costs of structures. The damage in that stage is signified by microcracks distributed throughout the material, where the crack size is comparable to the size of the aggregate. Prominent examples of microcrack damage are alkali-silica reaction (ASR), thermal damage, freeze-thaw, intrusion of water and acids, and even dynamic loading. ASR damage has been detected in concrete structures all around the world [8]. Due to the same order of size and thus very similar scattering effects, coherent ultrasonic evaluation methods have difficulty in distinguishing between the microstructure features (e.g. aggregate or porosity) and the damage. This difficulty is further increased by the random, multi-phase and heterogeneous nature of cement-based materials such as concrete, which not only leads to scattering, but to a very high attenuation of ultrasonic waves. Both effects (strong scattering and high attenuation) lead to complicated ultrasonic waveforms which make the application of coherent ultrasonic evaluation methods questionable.

Becker [5] gives an extensive overview of nondestructive evaluation methods for cement-based materials. However, most of the reviewed methods are limited to frequencies below 100 kHz which means the methods are only applicable to the detection of damage on length scales much bigger than the size of the scatterers. This limits the application because many damage types are characterized by distributed cracking on the scale of the aggregates – at least in the early stages of the deterioration process.

Diffuse measurements are a relatively new ultrasonic method compared to the coherent methods. First significant attempts were made in fluid acoustics studying the ultrasonic field, which is multiply scattered by a layer of randomly distributed glass spheres immersed in water [31, 38, 9, 46]. Important differences to cement-based materials are, however, the limitation to longitudinal waves and that the impedance mismatch between water and glass beads is very high. Most energy therefore, travels

through the water. The additional complication of mode conversion between longitudinal and transverse waves is, consequently, not an issue in these experiments, which is in contrast to experiments with ultrasonic waves in elastic solids. One big advantage of these setups [31, 38, 9, 46] is that it is very easy to measure a high number of different, statistically random configurations of glass beads with the same volume fraction, just by stirring the mix of glass beads and water; this is unfortunately not possible in the research on concrete presented here.

In elastic solids, first attempts at diffuse measurements were applied to characterize aluminum foam microstructure with varying pore sizes and distributions, and to polycrystals like heat-treated steel at very high frequencies [43, 44]. Anugonda et al. applies the method to concrete in [2] and determines the diffusion parameters, however a high uncertainty is present and only one type of concrete specimen is examined, while no variation in size, distribution or properties of the aggregate is investigated. Nonetheless, it is predicted that the diffusivity  $D$  will decrease with an increasing presence of distributed microcracking.

In [4], the diffuse method has successfully been applied to characterize the microstructure of cement-based materials, Punurai et al. [34] employed the method to characterize dissipation in cement paste, while Ramamoorthy et al. [35] used the diffuse method to detect large surface cracks and to quantify their depth.

The objective of this research is to develop a robust and reliable measurement method to detect microcrack damage in concrete by determining the two important parameters of the diffusion equation – diffusivity and dissipation – and comparing them for samples with different damage levels. The method is applied to two types of microcrack damage. The effects of geometric boundaries on the recovered parameters are investigated, and a comparison in terms of sensitivity is made to a coherent ultrasonic method.

## ***1.2 Effective medium theory for multi-phase materials***

Wave propagation through inhomogeneous materials is a very important problem with many practical applications, the most prominent one being nondestructive evaluation of the microstructure of composites such as fiber reinforced composites or concrete. Ultrasonic waves propagating in these media undergo multiple scattering which results in a frequency-dependent velocity and attenuation of the coherent wave. One approach to model the wave propagation is the so-called effective medium theory (EMT) assuming self-consistency, i.e. the scattered displacement field must vanish on average [19]. However, most effective medium theories that have been developed in the past deal with two-phase materials only, and cannot be extended to multiple phases.

The objective of this portion of the research is to develop an effective medium theory for multi-phase materials such as concrete. That way, the frequency dependent velocity and attenuation can be numerically determined, and are then compared to experimental data.

## ***1.3 Outline***

First, this thesis gives a brief introduction to cement-based materials, their composition and possible damage sources relevant to this research. After that, a short summary of the theory of wave propagation is given and important wave phenomena, which will help develop an intuitive understanding of wave propagation in elastic solids, will be presented. Next, the diffusion theory will be explained with a background of applications in the past and solutions to the diffusion equation that will be used later. Subsequently, a model to describe the effective properties of multi-phase materials will be derived. Afterwards, the experimental setup developed with the employed measurement equipment and concrete specimen of this research are

described. Finally, the results of the research will be presented. Recovered diffusivities  $D$  and dissipations  $\sigma$  of samples with different damage levels will be compared to develop a quantitative understanding of the effects of microcrack damage on said parameters. Also, a comparison of numerically determined effective parameters with measurement data will be given. This thesis ends with a concluding summary and provides an outlook on possible future work.

## CHAPTER II

### CEMENT-BASED MATERIALS

#### *2.1 Basic composition and properties*

Cement-based materials consist of multiple phases: the matrix material and several aggregate materials. In some literature, the aggregate and matrix phase are known as the filler and binder materials. Aggregate is typically sand and gravel of different sizes, geometries, properties and distributions. The matrix phase is a mixture of cement and water, that chemically react to form a cement paste. These constituents make concrete a heterogeneous, multi-phase material with multiple length scales. The following materials are known in the context of cement-based materials.

**Cement paste:** A cured mixture of cement and water in a certain ratio (depending on cement type and desired properties). Additives, normally in very small volume fractions, improve certain properties (like decreasing the susceptibility to cracking).

**(Portland) concrete:** A cured mixture of fine aggregate (sand), coarse aggregate (gravel) and (Portland) cement paste.

**Mortar:** A cured mixture of fine aggregate (sand) and cement paste.

Further information about the very complex microstructure and the elasticity and plasticity properties of cement-based materials is available in a number of monographs such as [26]. Some important mechanical properties of standard Portland concrete are summarized in Table 2.1.

Note that cement-based materials cause ultrasonic waves to attenuate significantly, with typical attenuation values of 25 to 75 dB/m for ultrasonic waves in the 100 –

**Table 2.1:** Typical properties of concrete

Property	Symbol	Value
Compressive strength	$\sigma_0$	35 MPa
Flexural strength	$\tau_0$	6 MPa
Tensile strength	$\sigma_0$	3 MPa
Young's modulus	E	28 GPa
Poisson's ratio	$\nu$	0.18
Density	$\rho$	1300 kg/m <sup>3</sup>
Strain at failure	$\epsilon$	0.001

200 kHz range, depending on the material composition [42].

## ***2.2 Porosity, interfacial zone, alkali-silica reaction (ASR) and thermal damage***

Concrete is a porous material (typically about 10 percent of the volume of concrete is occupied by pores) and, in saturated concrete, the pores contain a solution composed of alkali hydroxides (NaOH and KOH). The origin of the sodium (Na) and potassium (K) is, principally, the Portland cement. The equivalent alkali content of Portland cements produced in or imported into North America typically ranges from 0.20 to 1.20 % Na<sub>2</sub>Oe. Although the alkalies represent a small fraction of the Portland cement, they dominate the pore solution of concrete, which, as a result, is highly alkaline with a pH in the range of 13.2 to 13.8. Some forms of silica (SiO<sub>2</sub>) found in some aggregates are unstable at high pH and react with the alkali hydroxides to form an alkali-silica gel. This gel has the propensity to absorb large quantities of water and swell. Under certain conditions, the swelling pressures can cause expansion and, eventually, cracking of the concrete. [21, 40] give a very detailed description about the mechanisms of ASR and ways to prevent or reduce it.

Areas with increased porosity are the interfacial zones which surround the aggregate (gravel, sand) in the matrix material. This thin zone is mechanically weaker (lower Young's modulus, E) than the matrix material and the aggregate material.

This is another important factor in the heterogeneous property of concrete. In [5], a microscopic study of cement/glass-beads specimens was conducted and it was shown that the cracking usually starts at the interfacial zone and often connects aggregates.

Another source of microcrack damage besides ASR is thermal damage. The process of thermal damage of concrete is well understood [33]. In this research, samples are heated in an oven at 120° C. This causes the free water (some of which is part of the pore solution) in the concrete to evaporate which leads to an expansion resulting in cracking of the material.

## CHAPTER III

### THEORETICAL BACKGROUND

A number of comprehensive literature is available on wave propagation theory. Popular examples are [1], [13] and [6]. A short introduction of the fundamentals will be given in this chapter.

#### 3.1 Wave propagation

##### 3.1.1 Linear elasticity and equation of motion

The theory of linear elasticity gives the traction  $t_i$  on a plane with normal  $n_i$  by the equation

$$t_i = \sigma_{ji}n_j, \quad (3.1)$$

where  $\sigma_{ji}$  is the stress tensor.

Consider an arbitrary volume  $V$  with surface  $S$  as shown in Fig. 3.1. The balance of linear momentum can be expressed as

$$\int_S \sigma_{kl}n_k dS + \int_V \rho f_l dV = \int_V \rho \ddot{u}_l dV, \quad (3.2)$$

where  $\rho$  is mass density and  $f_i$  represents the body force. Applying the divergence

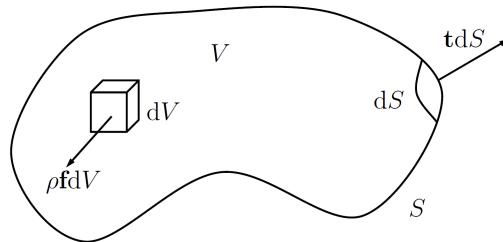


**Figure 3.1:** Momentum balance of arbitrary volume  $V$

theorem to the surface integral in Eq. (3.2) yields

$$\int_V (\sigma_{kl,k} + \rho f_l - \rho \ddot{u}_l) dV = 0. \quad (3.3)$$

Since Eq. (3.3) has to be true for arbitrary volumes, the integrand has to be zero which leads to the stress equation of motion described by

$$\sigma_{kl,k} + \rho f_l = \rho \ddot{u}_l. \quad (3.4)$$

This equation is usually referred to as Cauchy's equation of motion. In wave propagation theory it is usually more convenient to describe Eq. (3.4) only in terms of the displacement  $u_i$  instead of in terms of stress  $\sigma_{kj}$ . Using Hooke's law for a homogeneous, isotropic and linear elastic medium allows to achieve this. It is given by

$$\sigma_{ij} = \lambda \epsilon_{kk} \delta_{ij} + 2\mu \epsilon_{ij}, \quad (3.5)$$

where  $\epsilon_{ij}$  is the strain tensor, related to the displacement  $u_i$  by

$$\epsilon_{ij} = \frac{1}{2}(u_{i,j} + u_{j,i}), \quad (3.6)$$

and  $\mu$  and  $\lambda$  are the Lamé constants.

Neglecting body forces, substituting Eq. (3.6) into Eq. (3.5) and subsequently into Eq. (3.4) leads to Navier's equations of motion

$$\mu u_{i,jj} + (\lambda + \mu) u_{j,ji} = \rho \ddot{u}_i. \quad (3.7)$$

in index notation or

$$\mu \nabla^2 \mathbf{u} + (\lambda + \mu) \nabla \nabla \cdot \mathbf{u} = \rho \ddot{\mathbf{u}} \quad (3.8)$$

in vector form. Solving this partial differential equation (PDE) in Eq. (3.8) is difficult in general since it is a coupled partial differential equation. It can be uncoupled using the Helmholtz decomposition. The Helmholtz decomposition uses four potential functions  $\varphi, \psi_1, \psi_2$  and  $\psi_3$  which have to satisfy the following equation.

$$\mathbf{u} = \nabla \varphi + \nabla \times \boldsymbol{\psi}, \quad (3.9)$$

This represents a decomposition of the displacement into an irrotational or curl-free part (first term) and a solenoidal or divergence-free part (second term). For definiteness, we impose the requirement [24]

$$\nabla \cdot \boldsymbol{\psi} = 0 \text{ or } \psi_{i,i} = 0. \quad (3.10)$$

Plugging Eq. (3.9) into Navier's equation (3.8) leads to two uncoupled wave equations expressed in terms of the displacement potentials given by

$$\nabla^2 \varphi = \frac{1}{c_L^2} \ddot{\varphi}, \quad \nabla^2 \boldsymbol{\psi} = \frac{1}{c_T^2} \ddot{\boldsymbol{\psi}}. \quad (3.11)$$

$c_L$  represents the wave speed of the longitudinal wave and  $c_T$  the wave speed of the vertically and horizontally polarized (transverse) shear wave and they can be described with the Lamé constants and the mass density as

$$c_L^2 = \frac{\lambda + 2\mu}{\rho}, \quad c_T^2 = \frac{\mu}{\rho}. \quad (3.12)$$

It is always true that  $c_L > c_T$ . The Lamé constants  $\mu$  and  $\lambda$  can be described with the Young's modulus  $E$  and the poisson ratio  $\nu$  as

$$\lambda = \frac{E\nu}{(1+\nu)(1-2\nu)}, \quad (3.13)$$

$$\mu = \frac{E}{2(1+\nu)}. \quad (3.14)$$

The literature sometimes also uses the bulk modulus which is defined by

$$K = \lambda + \frac{2}{3}\mu \quad (3.15)$$

In analogy to the wave speed, one defines the longitudinal and the transverse wave numbers as

$$k_L^2 = \frac{\omega^2}{c_L^2}, \quad k_T^2 = \frac{\omega^2}{c_T^2}. \quad (3.16)$$

### 3.1.2 Wave phenomena

Under the assumption of a plane wave which means that a wave has constant properties  $(\epsilon, \sigma, u)$  on a plane perpendicular to its direction of propagation  $\mathbf{p}$  wave phenomena are discussed in this section. A mathematical representation of a plane wave is given in Eq. (3.17).

$$\mathbf{u} = f(\mathbf{x} \cdot \mathbf{p} - ct)\mathbf{d} \quad (3.17)$$

The unit vector  $\mathbf{d}$  defines the direction of particle motion and  $c$  is the wave speed, i.e. it is either  $c_L$  for a longitudinal wave or  $c_T$  for a transverse wave.

Plugging Eq. (3.17) into Eq. (3.8) yields

$$(\mu - \rho c^2)\mathbf{d} + (\lambda + \mu)(\mathbf{p} \cdot \mathbf{d})\mathbf{p} = 0. \quad (3.18)$$

There are two solutions to the above equation which both form the basis of wave propagation. Since  $\mathbf{p}$  and  $\mathbf{d}$  are two different unit vectors, the solution is either  $\mathbf{d} = \pm\mathbf{p}$  or  $\mathbf{p} \cdot \mathbf{d} = 0$ . This describes the following two cases.

1.  $\mathbf{d} = \pm\mathbf{p}$  leads to  $\mathbf{p} \cdot \mathbf{d} = \pm 1$  and together with Eq. (3.18) one obtains  $c = c_L$ . Since  $\mathbf{d}$  and  $\mathbf{p}$  are linearly dependent, this describes a particle movement in the direction of propagation which therefore describes a longitudinal or pressure (P) wave.
2.  $\mathbf{p} \cdot \mathbf{d} = \pm 0$  together with Eq. (3.18) leads to  $c = c_T$ . In this case the particle movement and the direction of propagation are perpendicular to each other which is described by the term transverse wave. Considering a two dimensional plane  $((x_1, x_2)$  plane), a wave with an in-plane displacement is called an SV-wave (vertically polarized), while a wave with an out-of-plane displacement is called an SH-wave (horizontally polarized).

### 3.1.3 Harmonic waves

In the previous section the shape of the travelling waveform  $f(x \cdot p - ct)$  can be of arbitrary form. Very often, it is convenient to consider a specific type of form of waves which show harmonic behavior in time and space and which are discussed in the following for the 1D case. The displacement can be described by

$$u(x, t) = A \cos \left[ \omega \left( \frac{x}{c} - t \right) \right] \quad (3.19)$$

where  $A$  is the amplitude and  $\omega = 2\pi f$  the circular frequency of the wave. Eq. (3.19) can also be written using a complex exponential expression which yields

$$u(x, t) = A e^{i(kx - \omega t)} \quad (3.20)$$

where

$$k = \frac{2\pi}{\lambda} = \frac{\omega}{c} \quad (3.21)$$

is the wavenumber of the harmonic length with wavelength  $\lambda$ . The term  $(kx - \omega t)$  in the exponent is often called phase of the wave.

In a homogeneous and isotropic material, transverse and longitudinal waves are nondispersive, i.e. their wave speeds are independent of frequency.

### 3.1.4 Reflection and Transmission of 1D waves

Travelling disturbances in a material are reflected and transmitted when the waves hit an ideal interface of two elastic media with different acoustic properties. The

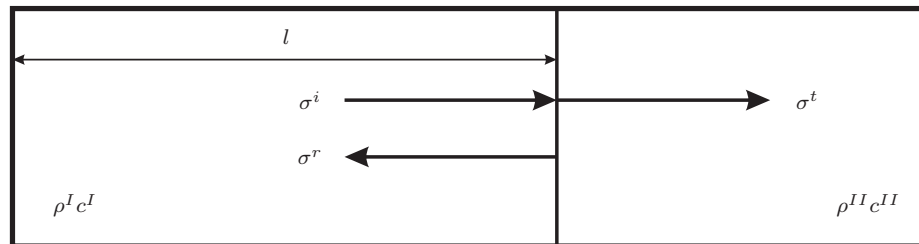


**Figure 3.2:** Reflected and transmitted 1D wave

pivotal property in this regard is the acoustic impedance  $Z = \rho c$ , i.e. the product of mass density and phase velocity of the type of wave that is considered. An impedance mismatch of two joined materials causes a reflected and transmitted portion of the incident wave. This process is illustrated in Fig. 3.2.

As it is known from the theory of wave propagation, the incident wave  $\sigma_i$  can be written in the following fashion [1]:

$$\sigma_i = f\left(t - \frac{x}{c}\right) \quad (3.22)$$

The reflected and transmitted portion of the wave can then be expressed in terms of the incident wave. This yields

$$\sigma_r = Rf\left(t - \frac{l}{c} + \frac{x-l}{c}\right) \quad (3.23)$$

$$\sigma_t = Tf\left(t - \frac{l}{c} - \frac{x-l}{c}\right). \quad (3.24)$$

$l$  denotes the propagation distance to the interface,  $R$  is the reflection coefficient while  $T$  is the transmission coefficient. With stress and displacement continuity as the boundary condition at the interface, the coefficients can be determined to be

$$R = \frac{Z_2 - Z_1}{Z_1 + Z_2}, \quad (3.25)$$

$$T = \frac{2Z_2}{Z_1 + Z_2}. \quad (3.26)$$

For the limit cases, one obtains that  $-1 < R < 1$  and  $0 < T < 2$ . One important example is the case of a free surface where the neighboring material cannot carry any mechanical waves (e.g. vacuum), i.e.  $Z_2 \rightarrow 0$ . In that case the reflected wave has the same shape as the incident wave but the sign of the stress changes after the reflection. In terms of the reflection and transmission coefficients, this means  $R = -1$  and  $T = 0$ .

### 3.1.5 Reflections of 2D P- and SV-waves

The two wave types propagate independently in an unbounded infinite medium. On interfaces of materials with different acoustic properties, reflections and couplings of

the longitudinal and transverse waves occur. Again, the important material property in that context is the acoustic impedance  $\rho c$ . An incident P-wave (SV-wave), which is reflected at a stress free boundary ( $\sigma_{22} = 0$  and  $\sigma_{21} = 0$ ) normally consists of both, a P-wave (SV-wave) and an SV-wave (P-wave). Fig. 3.3 shows the reflections of an incident P- and SV-wave.

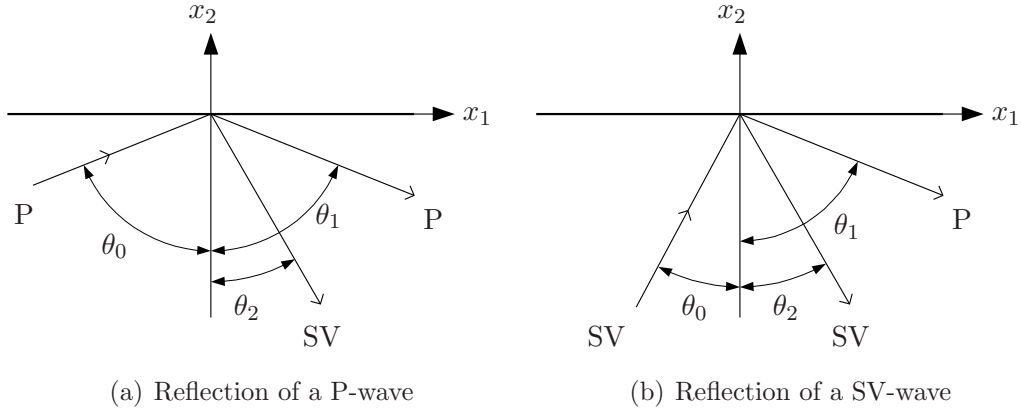


**Figure 3.3:** Wave reflections

The effect that a single incident wave-type produces two different waves after being reflected from a boundary is called mode conversion. Under plane-strain conditions, a harmonic wave in the  $(x_1, x_2)$  plane can be described by its displacement field in the following form

$$\mathbf{u}^{(n)} = A_n \mathbf{d}^{(n)} e^{ik_n(x_1 p_1^{(n)} + x_2 p_2^{(n)} - c_n t)}, \quad (3.27)$$

where  $n$  denotes the wave type (longitudinal or transverse),  $k_n$  is the respective wavenumber and  $c_n$  the respective wavespeed. Using these definitions, and assuming that the angular frequency  $\omega$  for the incident and reflected wave is equal, one can determine the relationship between the angle of the incident and the angles of the reflected waves. The relationships are given in Table 3.1.

Non-trivial amplitudes  $A_n$  can be obtained if the angles of the incident and reflected waves,  $\theta_0$ ,  $\theta_1$  and  $\theta_2$  (as defined in Fig. 3.3) satisfy Snell's law of reflection

$$k_0 \sin(\theta_0) = k_1 \sin(\theta_1) = k_2 \sin(\theta_2) \quad (3.28)$$

**Table 3.1:** Angle relations for reflection on a stressfree surface

incident $\theta_0$	reflected P $\theta_1$	reflected SV $\theta_2$
P	$\theta_1 = \theta_0$	$\sin \theta_2 = (c_T/c_L) \sin \theta_0$
SV	$\sin \theta_1 = (c_L/c_T) \sin \theta_0$	$\theta_2 = \theta_0$

There are two exceptions to mode conversion. The first is normal incidence with  $\theta_0 = 0$ . In this case, the waves are reflected as themselves. If the angle  $\theta_0$  is greater than a critical angle,

$$\theta_{\text{critical}} = \arcsin\left(\frac{c_T}{c_L}\right), \quad (3.29)$$

then only an SV-wave is reflected. The P-wave part of the reflected signal is then degenerated into the Rayleigh surface wave that travels along the surface with exponentially decreasing amplitude in the negative  $x_2$ -direction.

### 3.2 Attenuation

In the following section, an introduction to attenuation is given. Several attenuation mechanisms and their underlying physics will be explained and the mathematical representation of attenuation will be shown.

Usually, attenuation is incorporated in the wave propagation model that was discussed earlier by introducing a complex wave number  $\tilde{k}$ . The complex wavenumber is defined as an extension of Eq. (3.21)

$$\tilde{k} = \frac{\omega}{c} + i\alpha = k + i\alpha. \quad (3.30)$$

$\alpha$  denotes the wave attenuation coefficient. In addition to the complex wavenumber it is also possible to define a complex wavespeed and complex material properties.

For a plane, harmonic, one-dimensional wave, one plugs Eq. (3.30) into Eq. (3.17) to get the displacement field including attenuation. One obtains

$$u(x, t) = Ae^{i(\tilde{k}x - \omega t)} = Ae^{-\alpha x} e^{i(kx - \omega t)} \quad (3.31)$$

In the second form, the effect of the attenuation coefficient becomes quite obvious where the first part describes an exponential decay of the wave in the propagation direction while the second part describes the harmonic behavior of the wave.

Note that non-geometric attenuation is intrinsically linked to wave-velocity dispersion by the Kramers-Kronig relationship that is derived from the causality condition that the output strain cannot precede the input stress in any physical material ([27]). This is obvious, for example, if the dispersion relation  $c = \frac{\omega}{k}$  is modified in accordance to Eq. (3.30),

$$c_L = \frac{\omega}{\bar{k}} = \frac{\omega}{k' + k''i\omega} \quad (3.32)$$

where  $k'' \equiv \alpha$  denotes the attenuation coefficient and  $k'$  the real part of the wavenumber. It is clear that the (now complex) wavespeed depends on the frequency, therefore dispersion is found, i.e. waves of different frequencies travel with different wavespeeds.

In the following, several different attenuation mechanisms will be explained.

### 3.2.1 Viscoelastic material behavior - Absorption

In the general theory of elasticity, it is assumed that an elastic material stores energy without dissipation during deformation. While this is true for a number of materials (e.g. steel, aluminum) that are only dissipative for very high ultrasonic frequencies, there are many materials of technical interest (e.g. polymers, composites and cement-based materials) that dissipate part of the stored energy even for lower frequencies. Materials with this property are called viscoelastic since they combine the properties of an elastic solid and a viscous liquid. During deformation, a part of the stored energy in these materials is converted into heat due to internal friction which causes an ultrasound wave to lose some of its energy which results in a decreasing amplitude. This attenuation mechanism is also known as material absorption. The absorption in viscoelastic materials is usually assumed to be linearly dependent on the frequency in the range of ultrasound frequencies, and is called hysteresis absorption [37].

The material absorption of a specific material is usually incorporated into the theory of attenuation by applying a material absorption parameter

$$\alpha_a = \frac{C_a}{\lambda} \quad (3.33)$$

where  $C_a$  is a medium constant.

### 3.2.2 Geometric spreading

The effect of a decreasing ultrasonic wave due to spreading is called geometric attenuation. This effect is independent of frequency. It depends on the wave mode and the geometry of the investigated elastic body. As an example, Rayleigh surface waves are attenuated by  $1/\sqrt{r}$  where  $r$  is the propagation distance of the wave. This attenuation type is intrinsic in the wave equation. In the strictest sense, geometric spreading is not counted as attenuation since there is no energy loss associated with it.

### 3.2.3 Scattering

An important attenuation effect for this research is scattering attenuation in heterogeneous materials that is caused by wave scattering at material interfaces with different acoustic properties. These interfaces can be associated with the grain structure, defects (e.g. microcracks) or multiple phases of inclusions within the material (e.g. the interfacial zone between cement paste and aggregate), i.e. any inhomogeneity of the material can give rise to wave scattering. In the literature, different domains that have different approximations of the frequency dependence of the scattering attenuation coefficient are distinguished depending on the ratio of the wavelength,  $\lambda$ , to the size of the scatterer,  $a$  [30, 5]. Note that these theories are for coherent waves; that means they are primarily of interest for the EMT portion of this research and are less relevant for the diffuse part.

The scattering attenuation coefficient  $\alpha_s(\lambda, a)$  is also incorporated into the theory

of attenuation in a combination with Eq. (3.33) which yields

$$\alpha(\lambda, a) = \alpha_a(\lambda) + \alpha_s(\lambda, a) \quad (3.34)$$

In the Rayleigh domain, when the wavelength  $\lambda$  is much longer than the scatterer size  $a$ , the following functional form is found.

$$\alpha_s(\lambda, a) \propto \frac{a^3}{\lambda^4} \text{ for } \lambda \gg a \quad (3.35)$$

In the stochastic domain, with wavelength of the order of the scatterer size, the following functional form is found.

$$\alpha_s(\lambda, a) \propto \frac{a}{\lambda^2} \text{ for } \lambda \approx a \quad (3.36)$$

In the geometric domain, when the wavelength is much smaller than scatterer size, the following functional form is found.

$$\alpha_s(\lambda, a) \propto \frac{1}{a} \text{ for } \lambda \ll a \quad (3.37)$$

## CHAPTER IV

### ULTRASOUND DIFFUSION APPROXIMATION

According to [9], the multiply scattered ultrasonic wave that forms in a heterogeneous medium can be described as the superposition of a coherent ballistic part and an incoherent diffuse part.

The ballistic portion is either unscattered or forward scattered, and is both spatially and temporarily coherent with the incident source signal. For long wavelengths compared to the scatterer size or for small volume fractions of scatterers, the ballistic portion is dominant. The ballistic portion's amplitudes are significantly larger than the amplitudes of the diffuse part, so that the diffuse portion can be neglected. This regime can be modelled with effective media theories with useful results. The effective medium theories (EMT) can be effectively used for longer wavelengths which will be discussed in Chapter 5. However, these effective medium theories are unable to distinguish between different components of attenuation – attenuation caused by energy loss (dissipation) and attenuation caused by scattering losses. Also, the effective medium theories are not applicable to the strong scattering regime which is investigated in the first part of this research.

The diffuse portion of the signal is dominant in the strong scattering regime. It is spatially and temporarily incoherent with the incident signal. Because of rapid spatial fluctuations in phase and amplitude, the diffuse field will converge to zero if it is averaged over random configurations or averaged in a finite volume. This effect is called phase cancellation [31], and can be used to decrease the influence of the diffuse signal on a measured scattered signal of the diffuse and ballistic fields. Note that the phase cancellation is implicitly done by transducers with a finite surface area [9], and

makes it necessary to use transducers with a small surface area when measurement of the diffuse field is of interest. The procedure to achieve this will be described in Section 6.3.

#### ***4.1 Diffuse approximation and its governing equation***

The first major developments of the diffusion approximation were achieved through the study of the propagation of electromagnetic waves through strongly scattering materials [39]. The essential physics of the approximation are completely general to all types of classical waves, even though there are vast differences in length scales, impedance mismatches and wave velocities between applications in ultrasound acoustics or electromagnetic waves. Exploitation of the experience from using the diffusion approximation in the field of optics and electromagnetic waves is possible, but not straight forward. The main difference between the results from optics or electromagnetic waves, and ultrasonic waves in solids is the presence of longitudinal and transverse bulk waves in solid scatterers and the coupling between longitudinal and transverse waves during mode conversion.

The diffusion approximation is derived by neglecting coherence in the field – a reasonable assumption if a wave field has lost most of its original phase coherence and the field variables have become random after many scatterings – and can be used to describe the propagation of strongly scattered waves over a long distance. It is difficult to exactly determine the travel distance that is sufficiently long, since it depends on the strength of the scattering; several multiples of the scattering mean free path (the mean distance between successive scattering events) however is a reasonable requirement for the application of the diffusion approximation. In [46], a minimum of 4 to 10 scattering mean free paths is mentioned, but it is also pointed out that this is not universal and is dependent on the physical quantity under study, as well as the source-detector geometry.

The ultrasound diffusion approximation is derived with either an incoherent random walk model (analog to the derivation of the heat equation [14],[7]), or by perturbative multiple scattering formalisms [43]. A formal derivation is given in [39], less formal explanations are given in [36] and [44]. Several assumptions are made in the derivation: scatterers are distributed randomly in an elastic solid; resonance effects (as a result of high coherence of scattered waves) caused by a periodic distribution are not included in the model. All scattering is assumed to be linear elastic, i.e. no change in frequency from incident to reflected and transmitted waves takes place, and no energy is lost by scattering.

The diffusion of ultrasonic energy in a linear elastic body  $\mathcal{B}$  is described by the following second order parabolic partial differential equation (PDE). This PDE describes the time evolution of the spectral energy density  $\langle E(x, t, f) \rangle$  (energy per frequency, per volume) and is given by

$$\frac{\partial \langle E(x, t, f) \rangle}{\partial t} - D \Delta \langle E(x, t, f) \rangle + \sigma \langle E(x, t, f) \rangle = P(x, t, f) \quad \forall x \in \mathcal{B} \quad (4.1)$$

where  $P(x, t, f)$  is the spectral source energy density (forcing condition),  $D$  is the frequency-dependent diffusion coefficient and  $\sigma$  is the dissipation rate. The body is assumed to be isotropic, so the diffusion coefficient does not depend on direction.  $\langle \cdot \rangle$  is the expected value operator, i.e. Eq. (4.1) describes the evolution of the ensemble average energy density.

Eq. (4.1) is a modified version of the well-known heat conduction equation, supplemented by a dissipation term. The dissipation term does not complicate the solution procedure and will only add an  $e^{-\sigma t}$  term to the regular solution. Therefore, the applicable procedures to determine specific solutions are similar. Heat transfer theory solutions of common problems are covered in [7],[14].

To solve the partial differential equation (4.1), initial and boundary conditions are necessary. In the experimental setup considered in this research, almost no energy is transmitted from the elastic body (concrete specimen) to the surrounding air because

of a high impedance mismatch between the concrete and the air. Thus from energy considerations, this boundary condition is analogous to the insulation condition in heat transfer. The gradient on the body surface  $\partial\mathcal{B}$  has to be zero, implying no ultrasonic flux in the outward direction

$$\nabla\langle E(x, t, f) \rangle = 0 \quad \forall x \in \partial\mathcal{B}. \quad (4.2)$$

The initial condition is chosen to represent zero ultrasound energy at  $t = 0$

$$\langle E(x, t, f) \rangle = 0 \quad \text{for } t \leq 0. \quad (4.3)$$

#### 4.1.1 Definitions

A short explanation of some terms that are commonly used in the literature in the context of diffusive propagation is given:

- The transport mean free path  $l^*$  is the mean distance after which the direction of propagation of the energy is randomized [32].
- The scattering mean free path  $l_s$  is the mean distance a wave travels before it is scattered. For isotropic scattering, the scattering mean free path  $l_s$  is equal to the transport mean free path  $l^*$  [46].
- The energy velocity  $v_e$  is the average transport velocity of the ultrasonic energy and is defined as the ratio of the energy flux to the energy density [38].

#### 4.1.2 Identification of the coefficients

The phenomenological coefficients in Eq. (4.1) have different physical meanings [5]. Note that both generally depend on the frequency  $\omega = 2\pi f$  of the diffuse ultrasound.

$\sigma(f)$  is the energy dissipation in  $\frac{1}{\text{time}}$ . It must always be positive. Dissipation can be due to transformation of ultrasonic energy (kinetic and potential energy) to heat, surface losses or by nonlinear effects which lead to the excitation of

harmonics. Because elastic scattering is energy-conserving, it does not influence this dissipation. The dissipation can be represented alternatively as absorption (dissipation) time  $\tau_a = \sigma^{-1}$ , after which 100% of initial energy decreases to 63% if only dissipation takes place [32].

$D(f)$  denotes the diffusion coefficient with unit  $\frac{\text{length}^2}{\text{time}}$ .  $D$  depends on the material microstructure. Higher  $D$  means faster diffusion of the energy through the material.

### 4.1.3 Special solutions of the diffusion equation

Solutions of the diffusion equation for certain (common) geometries are presented. The frequency dependence of  $\sigma(f)$ ,  $D(f)$  and  $\langle E(f) \rangle$  is omitted in the remainder of this chapter.

#### 4.1.3.1 One-dimensional bar

Assuming the geometry of a semi-infinite bar, Eq. (4.1) is solved with an impulse excitation  $P(x, t) = P_0\delta(t)\delta(x)$ . The bar thickness is neglected, so the average energy density in the cross section is assumed to be uniform and the problem can be treated as one-dimensional with variable  $x$ . This leads to a simplified PDE and boundary condition.

$$\frac{\partial \langle E(x, t) \rangle}{\partial t} - D \frac{\partial^2 \langle E(x, t) \rangle}{\partial x^2} + \sigma \langle E(x, t) \rangle = P(x, t) \quad (4.4)$$

$$\frac{\partial \langle E(x, t) \rangle}{\partial x} = 0 \text{ for } x = 0 \quad (4.5)$$

The solution is given by

$$\langle E(x, t) \rangle = \frac{P_0}{2\sqrt{D\pi t}} e^{-x^2/(4Dt)} e^{-\sigma t}. \quad (4.6)$$

This solution is used by Turner in [2] to model the diffusion of ultrasound in a 1-D geometry (concrete rods with a length/diameter ratio of 9.2).

#### 4.1.3.2 Two-dimensional plate

Eq. (4.1) is solved in a rectangular coordinate system  $(x, y)$  with an impulse excitation at the origin  $P(x, t) = P_0\delta(t)\delta(x)\delta(y)$ . The plate thickness is assumed to be relatively small, so that the gradient in  $z$ -direction can be approximated to be equal to 0. The plate is assumed to have infinite extent ( $x \rightarrow \infty, y \rightarrow \infty$ ). From this, a closed-form solution can be given as

$$\langle E(x, t) \rangle = \frac{P_0}{4D\pi t} e^{-(x^2+y^2)/(4Dt)} e^{-\sigma t} = \frac{P_0}{4D\pi t} e^{-r^2/(4Dt)} e^{-\sigma t}. \quad (4.7)$$

Eq. (4.7) is obviously radially symmetric.

This solution will later be used in Section 7.1.5 as one model to approximate the ultrasound diffusion in the concrete cuboids that are used as specimens in this research. One big advantage of these semi-infinite solutions in equations (4.6) and (4.7) is that an easy linear regression to measured data is possible after a natural logarithm is taken on both sides. This will be explained in detail later.

#### 4.1.3.3 3D cuboid

The PDE (4.1) is now solved for a cuboid with the dimensions  $a \times b \times c$  with the boundary condition

$$\nabla \langle E(x, t, f) \rangle = 0 \quad \forall x \in \partial\mathcal{B} \quad (4.8)$$

which is equivalent to

$$\begin{aligned} \frac{\partial E}{\partial x}(0, y, z, t) &= \frac{\partial E}{\partial x}(a, y, z, t) = \frac{\partial E}{\partial y}(x, 0, z, t) \\ &= \frac{\partial E}{\partial y}(x, b, z, t) = \frac{\partial E}{\partial z}(x, y, 0, t) = \frac{\partial E}{\partial z}(x, y, c, t) = 0. \end{aligned} \quad (4.9)$$

The source is an impulse excitation at the point  $(x, y, z) = (x_0, y_0, z_0)$  which yields  $P(x, y, z, 0) = P_0\delta(t)\delta(x-x_0)\delta(y-y_0)\delta(z-z_0)$ . Following [14] and [35], a 3D solution

can be derived using Fourier series. The solution is given by

$$\begin{aligned}
\langle E(x, y, z, t) \rangle = & \left\{ 1 + \sum_{n=1}^{\infty} \sum_{m=1}^{\infty} \sum_{l=1}^{\infty} 8 \cos\left(\frac{n\pi x_0}{a}\right) \cos\left(\frac{m\pi y_0}{b}\right) \cos\left(\frac{l\pi z_0}{c}\right) \right. \\
& \times \cos\left(\frac{n\pi x}{a}\right) \cos\left(\frac{m\pi y}{b}\right) \cos\left(\frac{l\pi z}{c}\right) e^{-D[(n\pi/a)^2 + (m\pi/b)^2 + (l\pi/c)^2]t} \\
& + \sum_{n=1}^{\infty} \sum_{m=1}^{\infty} 4 \cos\left(\frac{n\pi x_0}{a}\right) \cos\left(\frac{n\pi x}{a}\right) \cos\left(\frac{m\pi y_0}{b}\right) \cos\left(\frac{m\pi y}{b}\right) \\
& \times e^{-D[(n\pi/a)^2 + (m\pi/b)^2]t} \\
& + \sum_{n=1}^{\infty} \sum_{l=1}^{\infty} 4 \cos\left(\frac{n\pi x_0}{a}\right) \cos\left(\frac{n\pi x}{a}\right) \cos\left(\frac{l\pi z_0}{c}\right) \cos\left(\frac{l\pi z}{c}\right) \\
& \times e^{-D[(n\pi/a)^2 + (l\pi/c)^2]t} \\
& + \sum_{m=1}^{\infty} \sum_{l=1}^{\infty} 4 \cos\left(\frac{m\pi y_0}{b}\right) \cos\left(\frac{m\pi y}{b}\right) \cos\left(\frac{l\pi z_0}{c}\right) \cos\left(\frac{l\pi z}{c}\right) \\
& \times e^{-D[(m\pi/b)^2 + (l\pi/c)^2]t} \\
& + \sum_{n=1}^{\infty} 2 \cos\left(\frac{n\pi x_0}{a}\right) \cos\left(\frac{n\pi x}{a}\right) e^{-D[(n\pi/a)^2]t} \\
& + \sum_{m=1}^{\infty} 2 \cos\left(\frac{m\pi y_0}{b}\right) \cos\left(\frac{m\pi y}{b}\right) e^{-D[(m\pi/b)^2]t} \\
& + \left. \sum_{l=1}^{\infty} 2 \cos\left(\frac{l\pi z_0}{c}\right) \cos\left(\frac{l\pi z}{c}\right) e^{-D[(l\pi/c)^2]t} \right\} \\
& \times P_0 e^{-\sigma t}. \tag{4.10}
\end{aligned}$$

This solution will later be used in Section 7.1.7 to model the diffusion process in the concrete specimens of this research. The models of equations (4.7) and (4.10) will be compared.

## CHAPTER V

### EFFECTIVE MEDIUM THEORY (EMT) FOR MULTI-PHASE MATERIALS

An effective medium with equivalent properties of the original material is a medium with space and time dispersion, i.e. its parameters depend on the frequency of the incident field. An interesting point is that even though the effective medium is homogeneous and isotropic, its effective properties depend on the type of the propagating wave; they are consequently not unique but different for longitudinal and transverse incident waves. As a self-consistent method, it is based on two hypotheses that reduce the problem with many particles to a problem with only a single particle. The two hypotheses are

1. Every inclusion behaves as an isolated one embedded in the medium with the effective properties of the composite. The wave that acts on this inclusion is a plane wave propagating in the effective medium.
2. The mean wave field in the composite coincides with the wave field propagating in the effective medium.

Kanaun derives a model for a two-phase effective medium in [16]. He assumes a medium that is made up of a matrix material and a random set of spherical inclusions. The derivation in this section will follow that of Kanaun. In this research, the model of Kanaun will be adapted to multi-phase materials. There is however, a slight conceptual difference between Kanaun's approach and the approach of this research. Kanaun only regards the actual inclusions as scatterers. He solves the single-scatterer problem of the inclusion in the effective medium and then uses that solution in the

surroundings of the original matrix material. This research takes a different route as an extension of the work of Kim et al. [19]. It regards both the inclusion and the matrix material as scatterers (which is intuitively plausible), solves the single-scatterer problem for all inclusion types (the material is multi-phase and multi-scale in this research), and then uses all solutions in the surroundings of the effective medium. An illustration of both approaches is given in Figs. 5.1 and 5.2.

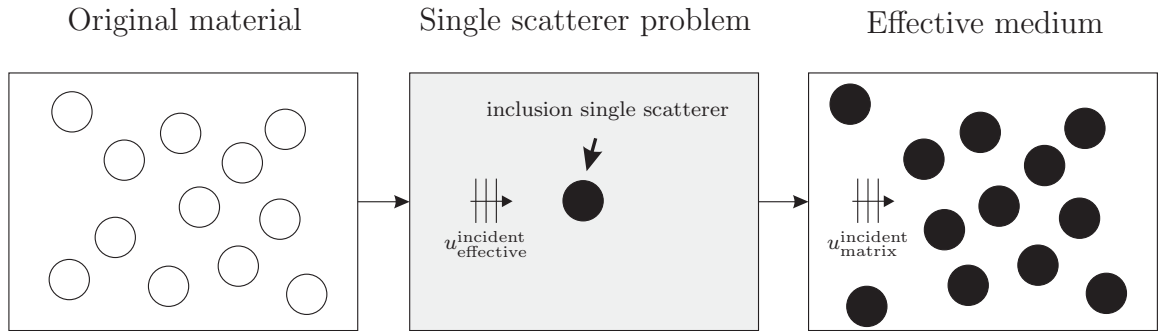


**Figure 5.1:** Illustration of Kanaun's self-consistency approach

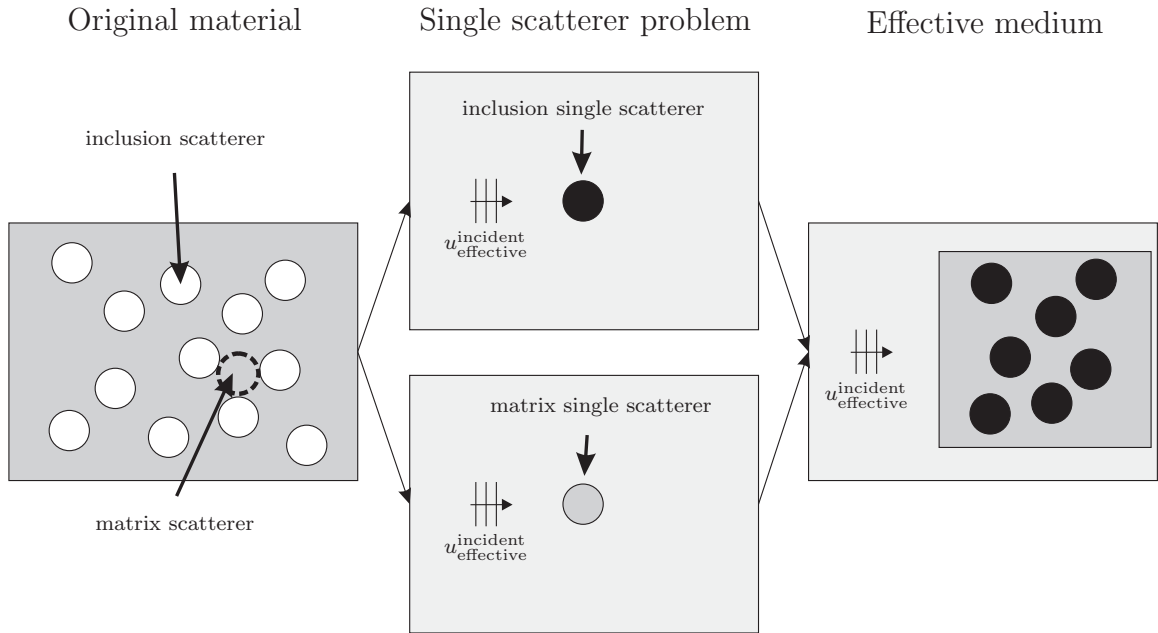


**Figure 5.2:** Illustration of this research's self-consistency approach

## 5.1 General scheme

From the first EMT hypothesis, the integral equation for the one particle problem, that will be needed later, can be set up.

$$u_i(x) = u_i^*(x) + \sum_{p=1}^N \int_{v_p} \partial_j G_{ik}^*(x-x') C_{kijm}^{*p} \epsilon_{mn}(x') + \omega^2 G_{ik}^*(x-x') \rho^{*p} u_k(x') dy' \quad (5.1)$$

where  $v_p$  is the inclusion volume of the  $p$ th material out of a total of  $N$  materials.  $C^{*p} = C^p - C^*$  where  $C^p$  is the stiffness tensor of the  $p$ th material and  $C^*$  is the stiffness tensor of the effective medium. The same applies for the density  $\rho^{*p} = \rho^p - \rho^*$ . The Green's function  $G^*$  is given by

$$G_{ik}^*(x) = \frac{1}{4\pi\rho^*\omega^2} \left[ \delta_{ik} k_{\text{T}}^{*2} \frac{e^{ik_{\text{T}}^* r}}{r} - \frac{\partial}{\partial x_i} \frac{\partial}{\partial x_k} \left( \frac{e^{ik_{\text{T}}^* r}}{r} - \frac{e^{ik_{\text{L}}^* r}}{r} \right) \right] \quad (5.2)$$

where  $k_{\text{L}}^{*2} = \frac{\rho^*\omega^2}{\lambda^*+2\mu^*}$  and  $k_{\text{T}}^{*2} = \frac{\rho^*\omega^2}{\mu^*}$ . The field  $u(x)$  inside the inclusion with center  $x_0 = 0$  can be described as

$$u_i(x) = \Lambda_{ik} u_i^*(x) = \left( \sum_{p=1}^N \Lambda_p \right) u_i^*(x) \quad \epsilon_{ij}(x) = \partial_i (\Lambda_{jk} u_k^*(x)) \quad (5.3)$$

$\Lambda$  is a linear operator that depends on the dynamic properties of the effective medium, the matrix and the inclusion materials. For the field inside the inclusion with center  $x_0 \neq 0$  one obtains

$$u(y) = \Lambda_{ik}^u(x-x_0) u_k^*(x) \quad \epsilon_{ij}(y) = \Lambda_{ijkl}^\epsilon(x-x_0) \epsilon_{kl}^* \quad (5.4)$$

where

$$\Lambda_{ik}^{up}(z) = \Lambda_{ik}^p e^{-ik^*\cdot z} e^{ik^*\cdot z} \quad \Lambda_{ijkl}^{\epsilon p}(z) = (\partial_j \Lambda_{ik}^p(z)) \frac{ik_l^*}{(k^*)^2} + \Lambda_{ik}(z) \delta_{lj} \quad (5.5)$$

$\Lambda_{ik}^{up}(z)$  and  $\Lambda_{ijkl}^{\epsilon p}(z)$  are introduced that coincide with  $\Lambda_{ik}^{up}(x-x_0^i)$  and  $\Lambda_{ijkl}^{\epsilon p}(x-x_0^i)$  if  $x$  is inside the inclusion centered at  $x_0^i$  and zero otherwise.

Now, consider a medium whose properties are estimates of the true effective

medium's properties. The scattering problem is solved in that medium.

$$\begin{aligned}
u_i(x) &= u'_i(x) \\
&+ \sum_{p=1}^N \int [\partial_j G'_{ik}(x-x') C'^p_{kjm n} \Lambda^{ep}_{m n r s} \epsilon_{rs}^*(x') + \omega^2 G'_{ik}(x-x') \rho'^p \Lambda^{up}_{kr} u_r^*(x')] S_p(x') dx'
\end{aligned} \tag{5.6}$$

where ' represents the estimate effective medium, i.e.  $C'^p_{ijkl} = C^p_{ijkl} - C'_{ijkl}$  and  $\rho'^p = \rho^p - \rho'$  where  $C^p, \rho^p$  belongs to the  $p$ th material ( $p = 1, \dots, N$ ) and  $C', \rho'$  belong to the estimate effective medium.  $G'$  is the Green function with elastic properties  $C', \rho'$ . Note that a differential operator is given by  $L'_{ik}(k) = C'_{ijkl} k_j k_l - \rho' \omega^2 \delta_{ik}$ . Also note  $L'_{ik}(k) G'_{kj}(k) = \delta_{ij}$  and  $L'_{ik}(k) u'_k(k) = L'(k) (2\pi)^2 \delta(k-k') = 0$ . After averaging and using self-consistency ( $u^*(x) = \langle u(x) \rangle$ ), one obtains

$$\begin{aligned}
\langle u_i(x) \rangle &= u_i^*(y) \\
&+ \sum_{p=1}^N p_p \int \partial_j G'_{ik}(x-x') C'^p_{kjm n} \Lambda^{Cp}_{m n r s} \langle \epsilon_{rs}(x') \rangle + \omega^2 G'_{ik}(x-x') \rho'^p \Lambda^{pp}_{kr} \langle u_r(x') \rangle dx'
\end{aligned} \tag{5.7}$$

where

$$\Lambda^C_{ijkl} = \frac{1}{p_p \Omega} \lim_{\Omega \rightarrow \infty} \int_{\Omega} \Lambda^{\epsilon}_{ijkl}(x) dx = \frac{1}{v_p} \int_{v_p} \Lambda^{ep}_{ijkl}(x) dx \tag{5.8}$$

$$\Lambda^{\rho p}_{ik} = \frac{1}{p_p \Omega} \lim_{\Omega \rightarrow \infty} \int_{\Omega} \lambda^{up}_{ik}(x) dx = \frac{1}{v_p} \int_{v_p} \Lambda^{up}_{ik}(x) dx \tag{5.9}$$

Taking the Fourier transform gives

$$\langle u_i(k) \rangle = u'_i(k) + \sum_{p=1}^N p_p [i k_j G'_{ik}(k) C'^p_{kjm n} \Lambda^{Cp}_{m n r s} \langle \epsilon_{rs}(k) \rangle + \omega^2 G'_{ik}(k) \rho'^p \Lambda^p_{kr} \langle u_r(k) \rangle] \tag{5.10}$$

Multiplication with  $L'(k)$  leads to

$$\left[ L'_{ik}(k) - \sum_{p=1}^N p_p [k_j C'^p_{ijm n} \Lambda^C_{m n k l} k_l + \omega^2 \rho'^p \Lambda^{\rho p}_{kr}] \right] \langle u_k(k) \rangle = 0 \tag{5.11}$$

Assuming  $\langle u(k) \rangle = (2\pi)^3 \delta(k-k^*)$ , one obtains

$$k_j^* C^*_{ijkl}(k^*) k_l^* - \rho^*_{ik}(k^*) \omega^2 = 0 \tag{5.12}$$

where

$$C_{ijkl}^* = C'_{ijkl} - \sum_{p=1}^2 p_p C'_{ijmn}{}^p \Lambda_{mnkl}^{C_p} \quad (5.13)$$

$$\rho_{ik}^* = \rho' \delta_{ik} + \sum_{p=1}^2 p_p \rho'{}^p \Lambda_{ik}^{\rho p} \quad (5.14)$$

Under the assumption that the estimate values  $C', \rho'$  are equal to the true values  $C^*, \rho^*$ , both cancel and the following equations give the final equations for the effective parameters.

$$0 = \sum_{p=1}^2 p_p C^{*p}{}_{ijmn} \Lambda_{mnkl}^{C_p} \quad (5.15)$$

$$0 = \sum_{p=1}^2 p_p \rho^{*p} \Lambda_{ik}^{\rho p} \quad (5.16)$$

### 5.1.1 Solution of the one-particle problem

As was discussed at the very beginning of this chapter, the self-consistency approach of the effective medium theory reduces the multiple scatterer problem to a one-particle problem. The solution of this problem is required for the numerical calculations of the next section. To do that, wave fields are represented in the form of a series of spherical vector functions [12].

First, consider an incident longitudinal wave. The incident wave propagating in  $z$ -direction represented in the form of a series of spherical vector functions is given by

$$\mathbf{u}^i = \mathbf{e}_3 e^{ik_L^* z} = -\frac{1}{k_L^*} \sum_{n=0}^{\infty} i^{n+1} (2n+1) \mathbf{L}_{0n}^1(\mathbf{r}) \quad (5.17)$$

$$\mathbf{L}_{0n}^1 = \mathbf{e}^r \frac{dj_n(k_L^* r)}{dr} P_n(\cos \theta) + \mathbf{e}^\theta \frac{j_n(k_L^* r)}{r} \frac{dP_n(\cos \theta)}{d\theta} \quad (5.18)$$

where  $P_n(\cos \theta)$  is the Legendre polynomial of order  $n$  and  $j_n(z)$  is the spherical Bessel function of order  $n$ .  $\mathbf{e}^r$  and  $\mathbf{e}^\theta$  are the basic vectors of the spherical coordinate system  $(r, \phi, \theta)$ , while  $\mathbf{e}^3$  is the unit vector of the  $z$ -axis.

Using spherical vector function representation, the scattered displacement field is

$$\mathbf{u}^s = \sum_{n=0}^{\infty} (a_n \mathbf{L}_{0n}^3 + b_n \mathbf{N}_{0n}^3) \quad (5.19)$$

and the transmitted field inside the inclusion is

$$\mathbf{u}^t = \sum_{n=0}^{\infty} (a'_n \mathbf{L}'_{0n} + b'_n \mathbf{N}'_{0n}) \quad (5.20)$$

where

$$\begin{aligned} \mathbf{L}_{0n}^3 &= \mathbf{e}^r \frac{dh_n(k_L^* r)}{dr} P_n(\cos \theta) + \mathbf{e}^\theta \frac{h_n(k_L^* r)}{r} \frac{dP_n(\cos \theta)}{d\theta} \\ \mathbf{N}_{0n}^3 &= \mathbf{e}^r \frac{n(n+1)}{r} h_n(k_T^* r) P_n(\cos \theta) + \mathbf{e}^\theta \frac{1}{r} \frac{d}{dr} [r h_n(k_T^* r)] \frac{dP_n(\cos \theta)}{d\theta}. \end{aligned} \quad (5.21)$$

$h_n(z)$  is called the spherical Hankel functions of the first kind.  $\mathbf{L}'_{0n}$  and  $\mathbf{N}'_{0n}$  can be determined from  $\mathbf{L}_{0n}^3$  and  $\mathbf{N}_{0n}^3$  by replacing  $h_n(z)$  with the spherical Bessel function  $j_n(z)$ . The prime denotes that the wavenumbers of the effective medium  $k_L^*$  and  $k_T^*$  are replaced by the wavenumbers of the material of the scatterer  $k_L^p$  and  $k_T^p$ . To determine the constants  $a_n, b_n, a'_n$  and  $b'_n$ , boundary conditions on the border of the inclusion  $r = a$  are imposed which are

$$u_r^i(a) + u_r^s(a) = u_r^t(a), \quad u_\theta^i(a) + u_\theta^s(a) = u_\theta^t(a), \quad (5.22)$$

$$\sigma_{rr}^i(a) + \sigma_{rr}^s(a) = \sigma_{rr}^t(a), \quad \sigma_{r\theta}(a)^i + \sigma_{r\theta}^s(a) = \sigma_{r\theta}^t(a). \quad (5.23)$$

Substitution of the components of the displacement vectors and stress tensors into the boundary conditions in Eq. (5.23) yields four linear algebraic equations for said constants. The system of equation is given as ([10])

$$\begin{aligned} \mathbf{L}_n \begin{bmatrix} a_n \\ b_n \end{bmatrix} - \mathbf{L}'_n \begin{bmatrix} a'_n \\ b'_n \end{bmatrix} &= i^{n+1} \frac{2n+1}{k_L^*} \begin{bmatrix} f_1^1(k_L^* a) \\ f_3^1(k_L^* a) \end{bmatrix} \\ \mathbf{M}_n \begin{bmatrix} a_n \\ b_n \end{bmatrix} - \frac{\mu_I}{\mu_{eff}} \mathbf{M}'_n \begin{bmatrix} a'_n \\ b'_n \end{bmatrix} &= i^{n+1} \frac{2n+1}{k_L^*} \begin{bmatrix} f_5^1(k_L^* a) \\ f_7^1(k_L^* a) \end{bmatrix} \end{aligned} \quad (5.24)$$

where the matrices  $\mathbf{L}_n$  and  $\mathbf{M}_n$  are defined as

$$\mathbf{L}_n = \begin{bmatrix} f_1^2(k_L^*a) & f_2^2(k_L^*a) \\ f_3^2(k_L^*a) & f_4^2(k_L^*a) \end{bmatrix}, \quad \mathbf{M}_n = \begin{bmatrix} f_5^2(k_L^*a) & f_6^2(k_L^*a) \\ f_7^2(k_L^*a) & f_8^2(k_L^*a) \end{bmatrix} \quad (5.25)$$

The radial functions  $f_m^i(qr)$ , ( $m = 1, 2, \dots, 8$ ;  $i = 1, 2$ ) are

$$\begin{aligned} f_1^i(k_L^p r) &= n y_n^i(k_L^p r) - k_L^p r y_{n+1}^i(k_L^p r), \\ f_2^i(k_T^p r) &= n(n+1) y_n^i(k_T^p r), \\ f_3^i(k_L^p r) &= y_n^i(k_L^p r), \\ f_4^i(k_T^p r) &= (n+1) y_n^i(k_T^p r) - k_T^p r y_{n+1}^i(k_T^p r), \\ f_5^1(k_L^p r) &= \left( n^2 - n - \frac{(k_T^p r)^2}{2} \right) y_n^i(k_L^p r) + 2k_L^p r y_{n+1}^i(k_L^p r), \\ f_6^i(k_T^p r) &= n(n+1) \left[ (n-1) y_n^i(k_T^p r) - k_T^p r y_{n+1}^i(k_T^p r) \right], \\ f_7^i(k_L^p r) &= (n-1) y_n^i(k_L^p r) - k_L^p r y_{n+1}^i(k_L^p r), \\ f_8^i(k_T^p r) &= \left( n^2 - 1 - \frac{(k_T^p r)^2}{2} \right) y_n^i(k_T^p r) + k_T^p r y_{n+1}^i(k_T^p r) \end{aligned} \quad (5.26)$$

where the following rules apply:

- The wavenumbers  $k_L$  and  $k_T$  have the superscript \* if they describe the wave in the effective medium and the superscript  $p$  if they describe the wave inside the scatterer i.e. inside an inclusion or inside the matrix since both are treated the same way in this model.
- If  $i = 1$ , the functions  $y_n^1(z)$  are the spherical Bessel functions  $j_n(z)$ , whereas for  $i = 2$ , the functions  $y_n^2(z)$  are the spherical Hankel functions  $h_n(z)$
- The matrices  $\mathbf{L}'_n$  and  $\mathbf{M}'_n$  are defined by the same Eqs. (5.25) and (5.26), if the functions  $f_m^2(k_L^*a)$  and  $f_l^2(k_T^*a)$  are replaced by  $f_m^1(k_L^p a)$  and  $f_l^1(k_T^p a)$ .

Next, consider the case of an incident transverse wave propagating in the  $z$  direction. Again, this can be expressed in terms of spherical vector functions as

$$\mathbf{u}_i = \mathbf{e}_1 e^{ik_T^p z} = \sum_{n=1}^{\infty} \frac{i^n (2n+1)}{n(n+1)} \left[ \mathbf{M}_{01n}^1(\mathbf{r}) - \frac{i}{k_T^p} \mathbf{N}_{01n}^1(\mathbf{r}) \right] \quad (5.27)$$

where  $\mathbf{e}_1$  is its polarization vector in the  $x$  direction and

$$\begin{aligned}\mathbf{M}_{01n}^1 &= \mathbf{e}^\theta j_n(k_{\text{T}}^p r) \frac{P_n^1(\cos \theta)}{\sin \theta} \cos \phi - \mathbf{e}^\phi j_n(k_{\text{T}}^p r) \frac{dP_n^1(\cos \theta)}{d\theta} \sin \phi, \\ \mathbf{N}_{e1n}^1 &= \mathbf{e}^r \frac{n(n+1)}{r} j_n(k_{\text{T}}^p r) P_n^1(\cos \theta) \cos \phi + \\ &\quad \left[ \mathbf{e}^\theta \frac{dP_n^1(\cos \theta)}{d\theta} \cos \phi - \mathbf{e}^\phi \frac{P_n^1(\cos \theta)}{\sin \theta} \sin \phi \right] \frac{1}{r} \frac{d}{dr} [r j_n(k_{\text{T}}^p r)]\end{aligned}\quad (5.28)$$

with the associated Legendre polynomials of order  $n$ ,  $P_n^1$ . The scattered and the transmitted field are now given as

$$\begin{aligned}\mathbf{u}^s &= \sum_{n=1}^{\infty} (c_n \mathbf{L}_{e1n}^3 + d_n \mathbf{M}_{o1n}^3 + e_n \mathbf{N}_{e1n}^3), \\ \mathbf{u}^t &= \sum_{n=1}^{\infty} (c'_n \mathbf{L}_{e1n}^{1'} + d'_n \mathbf{M}_{o1n}^{1'} + e'_n \mathbf{N}_{e1n}^{1'})\end{aligned}\quad (5.29)$$

where  $\mathbf{M}_{01n}^3$  and  $\mathbf{N}_{e1n}^3$  are obtained from  $\mathbf{M}_{01n}^1$  and  $\mathbf{N}_{e1n}^1$  by replacing the functions  $j_n(z)$  by  $h_n(z)$ ; and  $\mathbf{L}_{e1n}^3$  is given by

$$\begin{aligned}\mathbf{L}_{e1n}^3 &= \mathbf{e}^r \frac{d}{dr} [h_n(k_{\text{L}}^* r)] P_n^1(\cos \theta) \cos \phi + \\ &\quad \left[ \mathbf{e}^\theta \frac{dP_n^1(\cos \theta)}{d\theta} \cos \phi - \mathbf{e}^\phi \frac{P_n^1(\cos \theta)}{\sin \theta} \sin \phi \right] \frac{h_n(k_{\text{L}}^* r)}{r}\end{aligned}\quad (5.30)$$

The functions  $\mathbf{L}_{e1n}^{1'}$ ,  $\mathbf{M}_{o1n}^{1'}$  and  $\mathbf{N}_{e1n}^{1'}$  are obtained from  $\mathbf{L}_{e1n}^1$ ,  $\mathbf{M}_{o1n}^1$  and  $\mathbf{N}_{e1n}^1$  by changing the arguments  $k_{\text{L}}^* r$  and  $k_{\text{T}}^* r$  for  $k_{\text{L}}^p r$  and  $k_{\text{T}}^p r$ .

For the scattering coefficients  $c_n$ ,  $d_n$ ,  $e_n$  and the coefficients for the transmitted field  $c'_n$ ,  $d'_n$  and  $e'_n$  in Eq. (5.29) two more boundary conditions have to be set up at  $r = a$ . In addition to the continuity equations for the incident longitudinal wave given in Eq. (5.23), the incident transverse wave leads to two more continuity equations.

$$u_\phi^s(a) + u_\phi^i(a) = u_\phi^t(a) \quad \sigma_{\phi r}^s(a) + \sigma_{\phi r}^i(a) = \sigma_{\phi r}^t(a) \quad (5.31)$$

A system of equations analog to Eq. (5.24) can then be derived [23]. One obtains

$$\begin{aligned}
\mathbf{L}_n \begin{bmatrix} c_n \\ e_n \end{bmatrix} - \mathbf{L}'_n \begin{bmatrix} c'_n \\ e'_n \end{bmatrix} &= i^{n+1} \frac{2n+1}{k_{\text{T}}^* n(n+1)} \begin{bmatrix} f_2^1(k_{\text{T}}^* a) \\ f_3^1(k_{\text{T}}^* a) \end{bmatrix} \\
\mathbf{M}_n \begin{bmatrix} c_n \\ e_n \end{bmatrix} - \frac{\mu_I}{\mu_{eff}} \mathbf{M}'_n \begin{bmatrix} c'_n \\ e'_n \end{bmatrix} &= i^{n+1} \frac{2n+1}{k_{\text{T}}^* n(n+1)} \begin{bmatrix} f_6^1(k_{\text{L}}^* a) \\ f_8^1(k_{\text{L}}^* a) \end{bmatrix} \\
\mathbf{N}_n \begin{bmatrix} d_n \\ d'_n \end{bmatrix} &= -i^n \frac{2n+1}{n(n+1)} \begin{bmatrix} f_9^1(k_{\text{T}}^* a) \\ f_{11}^1(k_{\text{T}}^* a) \end{bmatrix}
\end{aligned} \tag{5.32}$$

The matrices  $\mathbf{L}_n$ ,  $\mathbf{M}_n$ ,  $\mathbf{L}'_n$  and  $\mathbf{M}'_n$  are defined in Eq. (5.25). The radial functions  $f_m^i(qr)$ , ( $m = 1, 2, \dots, 8$ ;  $i = 1, 2$ ) are given in Eq. (5.26) and the same rules as defined above still hold. The matrix  $\mathbf{N}_n$  is defined as

$$\mathbf{N}_n = \begin{pmatrix} f_9^2(k_{\text{T}}^* a) & f_{10}^1(k_{\text{T}}^* a) \\ f_{11}^2(k_{\text{T}}^* a) & f_{12}^1(k_{\text{T}}^* a) \end{pmatrix} \tag{5.33}$$

and the radial functions  $f_m^i(qr)$ , ( $m = 9, \dots, 12$ ;  $i = 1, 2$ ) are given by

$$f_9^i(k_{\text{T}}^p r) = y_n^i(k_{\text{T}}^p r) \tag{5.34}$$

$$f_{10}^i(k_{\text{T}}^p r) = -y_n^i(k_{\text{T}}^p r) \tag{5.35}$$

$$f_{11}^i(k_{\text{T}}^p r) = (n-1)y_n^i(k_{\text{T}}^p r) - k_{\text{T}}^p r y_{n+1}^i(k_{\text{T}}^p r) \tag{5.36}$$

$$f_{12}^i(k_{\text{T}}^p r) = -\frac{\mu_I}{\mu_{eff}} ((n-1)y_n^i(k_{\text{T}}^p r) - k_{\text{T}}^p r y_{n+1}^i(k_{\text{T}}^p r)) \tag{5.37}$$

The solution of the one-particle problem allows to find explicit forms of the tensors  $\Lambda_{ij}^\rho$  and  $\Lambda_{ijkl}^C$ . Because the mean wave field  $\langle u_k(x) \rangle$  is a plane wave we have [16]

$$\Lambda_{ik}^\rho \langle (u_k(x)) \rangle = h_i = \frac{1}{v} \int_v u_i(x) e^{-i\mathbf{q}^* \cdot \mathbf{x}} dx, \tag{5.38}$$

$$\Lambda_{ikkl}^C \langle (\epsilon_{kl}(x)) \rangle = H_{ij} = \frac{1}{v} \int_v \epsilon_{ij}(x) e^{-i\mathbf{q}^* \cdot \mathbf{x}} dx, \tag{5.39}$$

where  $\mathbf{q}^* = \mathbf{k}_{\text{L}}^*$  for longitudinal incident waves and  $\mathbf{q}^* = \mathbf{k}_{\text{T}}^*$  for transverse incident waves.

Only incident longitudinal waves are considered in this research. One obtains the following expressions for  $h^L$  and  $H^L$  [15]. The expressions for incident transverse waves can be found in [16].

$$h^{Lp} = -3k_L^* \sum_{n=0}^{\infty} (-i)^{n+1} \left[ a'_n \left( \frac{f_3^1(k_L^p a) f_1^1(k_L^* a)}{(k_L^* a)^2} + g_n(k_L^p, k_L^*) \right) + b'_n \frac{f_2^1(k_T^p a) f_3^1(k_L^* a)}{(k_L^* a)^2} \right] \quad (5.40)$$

where

$$g_n(k_L^p, k_L^*) = \frac{1}{(k_L^p a)^2 - (k_L^* a)^2} [k_L^p a j_{n+1}(k_L^p a) j_n(k_L^* a) - k_L^* a j_{n+1}(k_L^* a) j_n(k_L^p a)] \quad (5.41)$$

$$H_{ij}^{Lp} = ik_L^* [H_1^L \delta_{ij} + H_2^L (e_i^3 e_j^3 - \frac{1}{3} \delta_{ij})], \quad H_1^L = -\frac{(k_L^p a)^2}{k_L^* a^2} \sum_{n=0}^{\infty} (-i)^{n+1} a'_n g_n(k_L^p, k_L^*) \quad (5.42)$$

$$H_2^{Lp} = -\frac{3}{2} \left[ \frac{3}{a(k_L^* a)^3} \sum_{n=0}^{\infty} (-i)^{n+1} [a'_n F_n^a(k_L^p, k_L^*) + b'_n F_n^b(k_L^p, k_L^*)] + H_1^L \right] \quad (5.43)$$

where

$$\begin{aligned} F_n^a(k_L^p, k_L^*) &= f_1^1(k_L^p a) [f_2^1(k_L^* a) - 2f_1^1(k_L^* a) - (k_L^* a)^2 f_3^1(k_L^* a)] + f_3^1(k_L^p a) f_6^1(k_L^* a) \\ &\quad + (k_L^* a)^2 [f_3^1(k_L^p a) f_1^1(k_L^* a) + (k_L^* a)^2 g_n(k_L^p, k_L^*)], \\ F_n^b(k_L^p, k_L^*) &= f_2^1(k_T^p a) [f_2^1(k_L^* a) - 2f_1^1(k_L^* a) - (k_L^* a)^2 f_3^1(k_L^* a)] \\ &\quad + f_4^1(k_T^p a) f_6^1(k_L^* a) + (k_L^* a)^2 f_2^1(k_T^p a) f_3^1(k_L^* a) \end{aligned} \quad (5.44)$$

### 5.1.2 Numerical solution

In analogy to [16] and using the solutions of the one-scatterer problem from Eqs. (5.40) and (5.43), it is possible to find implicit solutions to Eq. (5.16). With  $H_1^L$ ,  $H_2^L$

and  $h^L$ , one obtains the following equations

$$\sum_{i=1}^N p_p(\rho_p - \rho^*) h^{Lp}(k_L^p, k_T^p, k_L^*, k_T^*) = 0 \quad (5.45)$$

$$\sum_{i=1}^N p_p(\mu_p - \mu^*) H_2^{Lp}(k_L^p, k_T^p, k_L^*, k_T^*) = 0 \quad (5.46)$$

$$\sum_{i=1}^N p_p(K_p - K^*) H_1^{Lp}(k_L^p, k_T^p, k_L^*, k_T^*) = 0 \quad (5.47)$$

where

$$k_L^* = \omega \sqrt{\frac{\rho^*}{K^* + \frac{4}{3}\mu^*}}, \quad k_T^* = \omega \sqrt{\frac{\rho^*}{\mu^*}} \quad (5.48)$$

where  $\rho^*$  is the density,  $\mu^*$  the shear modulus and  $K^*$  is the bulk modulus of the effective medium. The static solutions for  $H_1^L$ ,  $H_2^L$  and  $h^L$  which are necessary for the initial conditions are given by

$$3H_1^L = \frac{3K_s + 4\mu_s}{3K + 4\mu_s}, \quad H_2^L = \frac{5\mu_s(3K_s + 4\mu_s)}{\mu_s(9K_s + 8\mu_s) + 6\mu(K_s + 2\mu_s)}, \quad h^L = 1 \quad (5.49)$$

The corresponding static solutions of the effective parameters using Eq. (5.49) is then given by

$$\rho_s = \sum_{p=1}^N p_p \rho^p \quad (5.50)$$

$$\mu_s = \frac{\sum_{p=1}^N p_p \mu^p \frac{5\mu_s(3K_s + 4\mu_s)}{\mu_s(9K_s + 8\mu_s) + 6\mu(K_s + 2\mu_s)}}{\sum_{p=1}^N p_p \frac{5\mu_s(3K_s + 4\mu_s)}{\mu_s(9K_s + 8\mu_s) + 6\mu(K_s + 2\mu_s)}} \quad (5.51)$$

$$K_s = \frac{\sum_{p=1}^N p_p K^p \frac{3K_s + 4\mu_s}{3K + 4\mu_s}}{\sum_{p=1}^N p_p \frac{3K_s + 4\mu_s}{3K + 4\mu_s}} \quad (5.52)$$

The static equations can be solved numerically with Maple. The dynamic solutions for Eqs. (5.45) - (5.47) are determined with a multidimensional Newton-Raphson method using Matlab.

## CHAPTER VI

### EXPERIMENTAL PROCEDURE FOR DIFFUSE MEASUREMENTS

This section describes the instrumentation used for the diffuse measurements in this research.

#### *6.1 Signal generation*

A high voltage pulse generator (Panametrics 5058 PR) provides the source signal for the diffuse measurements. The voltage of the pulse generator can be continuously varied in the range of 100 - 900 V. It also provides a switch that allows the user to select fixed voltage values of 100, 200, 400 and 900 V. The manufacturer provides information about the bandwidth as +10MHz. The pulse repetition frequency can be set to 20, 50, 100, 200, 500, 1000 or 2000 Hz. The damping factor – which determines the duration of the decay from peak to zero voltage – can be set to the values 50, 100, 200, or 500  $\Omega$  or can be continuously varied. The smaller the damping factor is, the sharper the pulse is in time which leads to a broader frequency spectrum. More details on the effect of the damping factor of impulse generators can be found in [5]. In this research, the voltage is set to 400 V, the damping factor to 50  $\Omega$  and the pulse repetition frequency to 20 Hz.

The impulse generator also generates a 5V rectangular synchronization signal, whose positive edge is used to trigger the signal acquisition of the oscilloscope. The impulse generator can also be used in pulse-echo mode, in which the same transducer is used as both source and receiver. This mode, however, is not used in this research since it is difficult to apply to concrete samples.

For the velocity measurements, a Panametrics 5072 PR pulse generator is used to generate a pulse, with a source voltage of 210 V. The pulse generator also has a damping factor with settings from 1 to 8, but with a reverse meaning, i.e. a higher damping factor gives a sharper pulse in time. In this research, the damping factor is set to 6.

## ***6.2 Received signal amplification***

Due to high attenuation of cement-based materials, both a high input signal and an amplified received signal are essentially needed to get a high signal-to-noise ratio from the concrete specimens used in this research.

In a first step of amplifying and signal conditioning, a pre-amplifier (DigitalWave DW2040G/A) that amplifies the received signal by 40 dB is used in series with a signal conditioning amplifier DigitalWave DW FTM4000. This amplifier allows a further amplification of 20 dB. Both maximum amplification values are used for the diffuse measurements. The amplifier also allows the setting of a lowpass and highpass filter. In this research however, they are set to their respective minimum (20 KHz) and maximum (4 MHz) values. The manufacturer intends the combination of pre-amplifier and amplifier and they are optimized to this application. The frequency ranges of both are broad enough for this research ( $\sim 0.6 \text{ MHz} < f < \sim 1.3 \text{ MHz}$ ).

For the velocity measurements, the integrated amplifier in the pulse generator is used. A low-power amplifier is integrated into the impulse generator. The disadvantage of this amplifier, cross-talk during the pulse generation, can be neglected, since the (real) important signal is slightly later and not affected by the cross-talk. Cross-talk is an artificial signal, because it is only due to the imperfect electrical isolation in the amplifier and it is caused by a distortion of the amplified received signal by the pulse and the synchronization signal.

### ***6.3 Source/receiver transducer***

Both source and receiver in this research are Panametrics V103 1 MHz broadband transducers with a diameter of 12.5 mm. The manufacturer provides a calibration sheet which states that the optimal frequency band is 0.7 - 1.3 MHz. As was mentioned in Section 4, it is necessary for the diffuse measurements to have a small receiver surface. For this purpose, a small cone is designed and manufactured. The bottom diameter of the cone is 5 mm, the top diameter is 2 mm, its thickness 2.2 mm. The cone is manufactured out of aluminum. Another cone made of steel led to identical results. Fig. 6.1 shows a picture of the transducer where the attached cone is clearly seen. The cone is attached with glue (LOCTITE Super Glue). Unfortunately, the added cone makes the transducer unstable which makes consistent coupling conditions difficult. To prevent these inconsistencies, a fixture is designed and manufactured (Fig. 6.2) that is clamped to the specimen to keep the transducer perfectly perpendicular to the surface. A typical configuration is shown in Fig. 6.3.

An alternative to this transducer would be a pin-transducer manufactured by Valpey-Fisher with a diameter of 1 mm. However, several problems with these pin-transducers were encountered. First, it is very difficult to keep the coupling conditions consistent with this type of transducer. Not only is it difficult to keep them perfectly perpendicular to the surface, it is also difficult to fix them to the sample with a constant pressure. Also, it was shown that pin-transducers have only narrow-band efficiency [5] and they are sensitive to electromagnetic fields of other measurement equipment like the pulse generator. For these reasons, a pin-transducer is not used in this research.

### ***6.4 Waveform acquisition***

A four channel digital Tektronix TDS5034 oscilloscope is used for this research. It provides a sampling rate up to 5 GSamples per second, but the maximum sampling



**Figure 6.1:** Receiving transducer with cone

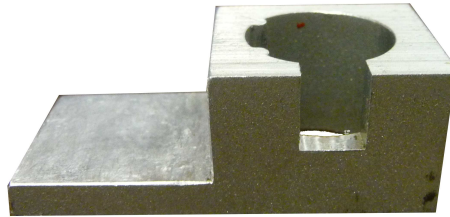


**Figure 6.2:** Fixture for receiving transducer

rate in this research is 125 MHz for the velocity measurements. The impedance is always set to 1 M $\Omega$ . The oscilloscope runs Windows 2000 as an operating system and allows saving the acquired waveforms in the \*.dat format which is readable by Matlab. The files can be easily transferred to a PC using a flash drive for further signal processing.



**Figure 6.3:** Fixture clamped to sample with receiving transducer

### 6.4.1 Signal-to-noise ratio (SNR) and averaging

All measurements are obtained by avering 500 individual measurements during the acquisition with the oscilloscope. This averaging decreases the noise levels by 27 dB, which is very critical for diffuse ultrasound signals to get an acceptable signal-to-noise ratio. Following [5], the following section shows why the averaging of the signals reduces the standard deviation  $\sigma$  by  $\sqrt{N}$  if the signal noise is uncorrelated.

Consider an individual measurement  $X_i$  with  $X_i = s_i + N_i$ , where  $s_i$  is the deterministic portion of the signal and  $N_i$  is a random variable representing the noise. Assuming  $E[N_i] = 0$  and  $E[N_i^2] = \sigma_N$ , the mean and variance of  $X_i$  is given by:

$$m_{X_i} = E[X_i] = s_i + E[N_i] = s_i \quad (6.1)$$

$$\sigma_{X_i}^2 = E[(X_i - m_{X_i})^2] \quad (6.2)$$

assuming unbiased measurements ( $E[s_i] = s_i$ ). The averaged value over  $N$  measurements is then given by  $X = \frac{1}{N} \sum_{i=1}^N X_i$ . If the noise of the  $N$  different  $X_i$  is uncorrelated (a strict assumption), one can simply add the variances and calculate the variance of the averaged signal. One obtains

$$\sigma_X^2 = E[(X - m_X)^2] = E\left[\left(\frac{1}{N} \sum_{i=1}^N X_i - m_{X_i}\right)^2\right] = E\left[\frac{1}{N^2} \sum_{i=1}^N (X_i - m_{X_i})^2\right] \quad (6.3)$$

It follows:

$$\sigma_X^2 = \frac{1}{N^2} E\left[\sum_{i=1}^N (X_i - m_{X_i})^2\right] = \frac{\sigma_N^2}{N} \quad (6.4)$$

One can conclude that under the assumption of uncorrelated noise, averaging over  $N$  signals decreases the variance by the factor  $N$  and therefore the standard deviation by  $\sqrt{N}$ . Obviously, averaging does not decrease systematic errors, because they are not independently distributed or do not have zero mean.

### 6.4.2 Sampling rate and record length

All measurements are sampled with a sampling frequency  $f_s$  of at least 50 MHz and are filtered with a 4 MHz low pass filter. Therefore, the requirement of the Nyquist-Shannon sampling theorem that the sampling rate must exceed at least twice the highest frequency in the sampled analog signal is met. If it is not met, frequency aliasing occurs, i.e. higher frequencies are detected as lower frequency content [29].

## 6.5 *Specimens*

### 6.5.1 Description

All specimens are cast according to the standard ASTM C 1293 [3]. It is a standard test to quantify aggregate reactivity with regard to ASR damage in concrete by measuring expansion of concrete bars. The expansion data of the three ASR damage levels used in this research is shown in Fig. 6.4. One can see that ASR 1 has the most damage, ASR 6 has medium damage and ASR 7 has the least damage among the three samples. All bars are two years old when the tests began, so they are certain to have reached their final strength. The original bars have the dimensions 75 mm  $\times$  75 mm  $\times$  285 mm. From these bars, the actual samples of this research are cut. The samples then have the dimensions 75 mm  $\times$  75 mm  $\times$  46 mm for the diffuse measurement and in addition 75 mm  $\times$  75 mm  $\times$  13 mm for the velocity measurement.

For concrete, the volume fractions of aggregates are given as gradation [25]. Gradation is evaluated by passing the aggregates through a series of sieves. The sieve retains particles larger than the opening, while smaller ones pass through. In the U.S., sieves with openings greater than 1/4 in. are designated by the size of the opening. Sieves smaller than 1/4 in. are specified by the number of uniform openings per linear inch (e.g. a #16 sieve has 16 openings per inch). The mix designs of the original bars of the three ASR damage levels are given in Table 6.1; the gradation for the fine aggregate is given in Table 6.2; the gradation for the coarse aggregate is given

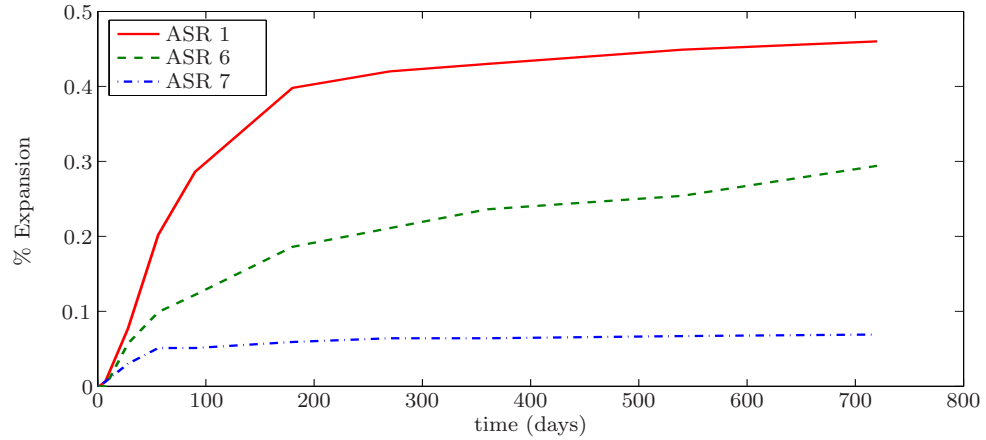


**Figure 6.4:** Expansion data of ASR damaged concrete samples

in Table 6.3 in accordance with ASTM C 1293 standard. Note that the water/cement ratio is 0.45. However, for some samples, a cement substitute is used to replace some portion of the cement. The substitutes used are metakaolin (MK) and fly ash (FA). Both are used in concrete to reduce the ASR reactivity. The cement used has a total alkali content of  $0.9 \pm 0.1$  %  $\text{Na}_2\text{O}$  equivalent.  $\text{NaOH}$  is added to the concrete mixing water so as to increase the alkali content of the mixture to 1.25 % by mass of cement.

Acoustical properties of the concrete constituents are given in Table 6.4 [17]. Even though the cited limestone aggregate is not exactly the same as the one used in this research, its acoustic properties are assumed to be a valid approximation, especially since only a rough estimate is needed in the following Section 6.5.2.

All samples that are cut from the original bars are assumed to have the same amount of cement paste. All surfaces of the samples used are polished to improve the coupling conditions for the ultrasonic transducers.

All the original bars were cast and all information about them was provided by Robert Moser (Graduate Research Assistant at Georgia Tech).

**Table 6.1:** Mix design for concrete samples

Mix	w/cm	MK Type	% MK	% FA	Fine Agg. (lb)	Coarse Agg. (lb)	Cement (lb)	MK (lb)	FA (lb)	Water (lb)	NaOH (lb)
ASR 1	0.45	-	0	0	2.7	4.5	1.73	0	0	0.77	0.0077
ASR 6	0.45	-	0	25	2.63	4.5	1.3	0	0.43	0.77	0.006
ASR 7	0.45	235	8	25	2.6	4.5	1.17	0.13	0.43	0.77	0.0053

**Table 6.2:** Gradation of fine aggregate

Sieve #	Amount retained/total weight (%)
# 4	6.2
# 8	7.1
# 16	14.8
# 30	18.7
# 50	33.0
# 100	15.8
pan	4.4
Total	100

**Table 6.3:** Gradation of coarse aggregate

Sieve size		Amount retained/total weight (%)
Passing	Retained	
19 mm	12.5 mm	33.3
12.5 mm	9.5 mm	33.3
9.5 mm	4.5 mm	33.3

**Table 6.4:** Acoustic properties of concrete constituents

Material	$C_L$ (m/s)	$C_T$ (m/s)	$E$ (GPa)	$\nu$	$\rho$ (kg/m <sup>3</sup> )	$Z$ (kg/sm <sup>2</sup> )
Limestone	5200	2830	55.8	0.29	2700	14040000
Sand	5570	3540	75.4	0.16	2600	14482000
Cement paste	3550	2000	20.0	0.26	1950	6922500

### 6.5.2 Impedance mismatch

With the acoustic properties in Table 6.4 and the definitions of reflection and transmission coefficient from Section 3.1.4, the values of the coefficients for the paste/sand and paste/aggregate interfaces can be determined. It is assumed there is generally no contact between aggregates, so sand/aggregate coefficients are not necessary. One obtains

$$R_{\text{paste/sand}} = 0.3532 \quad (6.5)$$

$$T_{\text{paste/sand}} = 1.3532 \quad (6.6)$$

$$R_{\text{paste/stone}} = 0.3395 \quad (6.7)$$

$$T_{\text{paste/stone}} = 1.3395 \quad (6.8)$$

According to these values the ultrasound waves travel through all materials, i.e. also a considerable distance in the paste which is the major cause for absorption.

## CHAPTER VII

### RESULTS

Two sets of experiments are considered and their results will be presented in the following. The first are diffuse field measurements with a pair of piezoelectric transducers, located off center from each other. The second set is a coherent velocity measurement with aligned piezoelectric transducers as source and receiver.

The first section is based on the diffusion theory in chapter 4 and the off-center measurements. It describes a procedure to determine the material-related parameters,  $D$  and  $\sigma$ . Two different diffusion models are used in this procedure, a 2D semi-infinite model and a 3D finite model. The diffusion method is applied to two types of microcracking damage: ASR and thermal damage. Results for all specimens are presented, and the accuracy and limitations of the proposed methodologies are discussed. A source/receiver combination with high efficiency in the investigated band width (0.65 MHz to 1.1 MHz) is chosen to enable diffuse field measurements with sufficient signal-to-noise ratio in the strongly attenuating specimens.

In the second section, the velocity in the same damaged specimens is determined with a coherent measurement technique.

A comparison of the sensitivity of both methods investigated is presented.

Afterwards, the results of the effective medium theory calculations are shown. A comparison of the numerically determined values to experimental data from literature is given and discussed.

#### ***7.1 Diffusion approximation***

The impulse responses of different specimens are measured 38 mm off of the epicenter on the opposite side (with respect to the source) as shown in Fig. 7.1. The choice

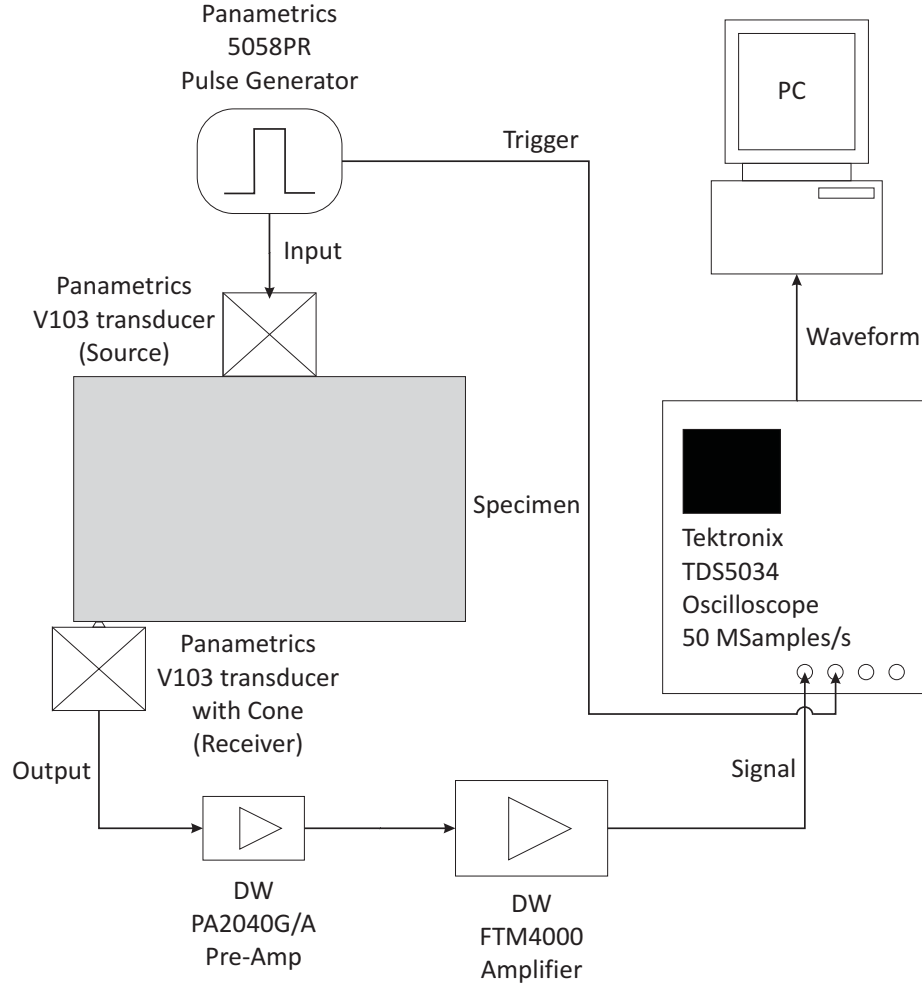


**Figure 7.1:** Setup for diffuse ultrasound measurement

of this location is important, because no ballistic signal component is included in the measured signals there.

The source transducer is set in the center, and the receiver close to the corner. That way, when the receiver is placed near a corner, the most receiving points with the same source/receiver distance are available on a sample. It can be seen in Eq. (4.7) that points with equal source/receiver separation  $r$  should theoretically have the same expected value for the spectral energy density  $\langle E \rangle$  which allows spatial ensemble averaging of measurements from different points. The same is valid for Eq. (4.10). In that case putting the receiver in a different corner corresponds to a rotation of the

coordinate system so that the coordinates  $(x, y, z)$  and  $(x_0, y_0, z_0)$  stay the same for every receiver configuration with the same source/receiver distance.

If a ballistic portion is present in the signal, it is necessary to separate the coherent (ballistic) portion from the incoherent (diffuse) signal component. This separation can be accomplished by averaging signals taken at multiple locations to obtain the coherent signal contribution (the incoherent portion will average to zero) and then subtracting this coherent signal from the individual signals. This procedure will only work if there are a large number of detection points and all averaged signals are measured in a consistent fashion. Since the chosen position ensures enough scattering to justify using the diffusion approximation, this is not necessary in the present setup. A use of this technique in a setup with immersion transducers is shown in [46].

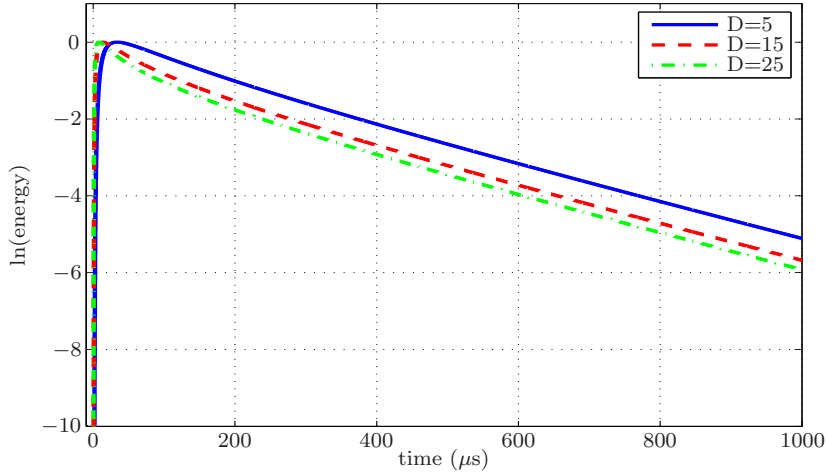
### 7.1.1 Measurement setup description

The diffuse field response of a pulse excitation is detected with the point-like cone transducer (see Section 6.3), amplified and recorded with 200000 record points at 50 MHz sampling frequency (see Section 6.4.2), which roughly corresponds to a 4 ms effective useful signal length. Only about 1 ms of the signal is actually used for the calculations, although the signal tail is useful to determine the noise level.

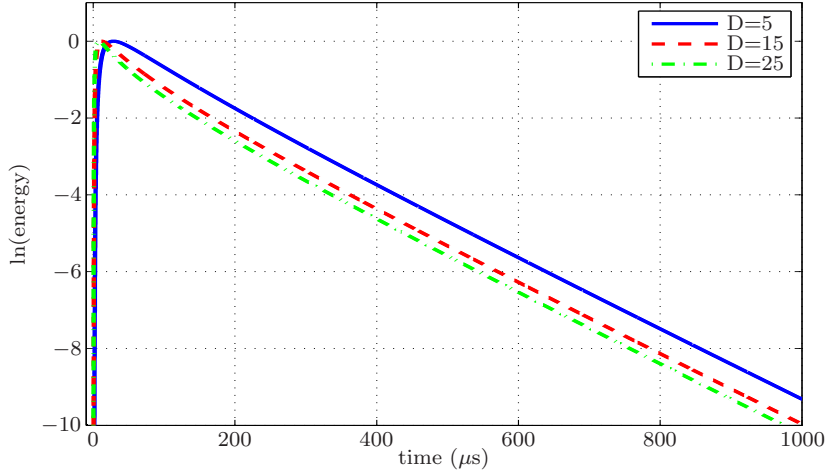
The source/receiver combination and the excitation pulse are kept the same for all measurements to assure the best possible consistency between measurements on different specimens. A viscous couplant is used to couple both source and receiver to the specimen. For the receiver, an oily (less viscous) couplant is used to increase repeatability. With gel couplants, thickness variations and settling times of the couplant layer may introduce inconsistencies for the small surface receiver [11].

### 7.1.2 Simulation of the energy density evolution $\langle E(x, t, f) \rangle$

Values for the  $D$  and  $\sigma$ -coefficients that were experimentally obtained by Anugonda et al. [2] with real concrete samples in a one-dimensional setup, are used to simulate

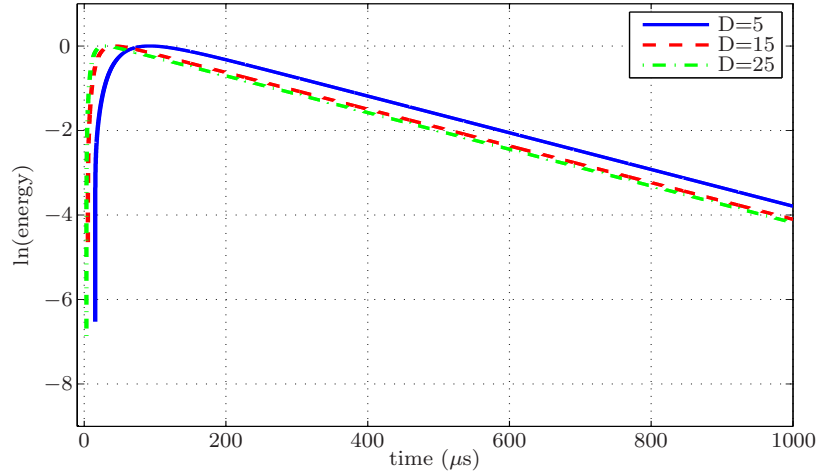


(a) Solutions with dissipation  $\sigma = 10000 \frac{1}{s}$  for infinite 2D model

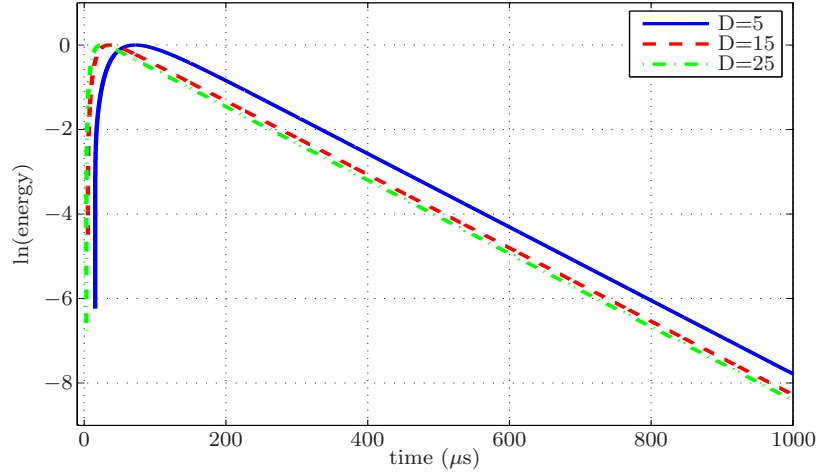


(b) Solutions with dissipation  $\sigma = 20000 \frac{1}{s}$  for infinite 2D model

**Figure 7.2:** Simulation of the energy density evolution with the infinite plate solution the approximate solution for a two-dimensional plate (Eq. (4.7)), which is later used as an initial guess for the determination of the coefficients  $D$  and  $\sigma$  for different frequencies. The same is done for the solution for a three-dimensional cuboid (Eq. (4.10)). The goal is to estimate changes in  $\langle E(x, t, f) \rangle$  depending on variations of  $D$  and  $\sigma$ . All calculated functions  $\langle E(x, t, f) \rangle$  are normalized to  $\max \langle E(x, t, f) \rangle = 1$  to obtain visually better plots. The normalization only influences the coefficient  $P_0$ , which is neglected later, because of its high dependence on measurement and



(a) Solutions with dissipation  $\sigma = 10000 \frac{1}{s}$  for finite 3D model



(b) Solutions with dissipation  $\sigma = 20000 \frac{1}{s}$  for finite 3D model

**Figure 7.3:** Simulation of the energy density evolution with the finite cuboid solution transducer coupling conditions. As can be seen in Figs. 7.2 and 7.3 that are obtained with the same set of  $D$  values (in  $\frac{m^2}{s}$ ) but with different  $\sigma$  values, variations in  $\sigma$  lead to very different curve fall-off slopes (here after  $50 \mu s$ ). In contrast, variations in the diffusivity  $D$  lead to more changes at early times, after some time (here  $100 - 200 \mu s$ ) the curves of different  $D$  values have the same slope. The peak gets sharper and approaches  $t = 0$  with increasing  $D$ , but never reaches  $t = 0$ . Note that both energy evolution curves (Eq. (4.7), (4.10)) have a singularity at  $t = 0$ .

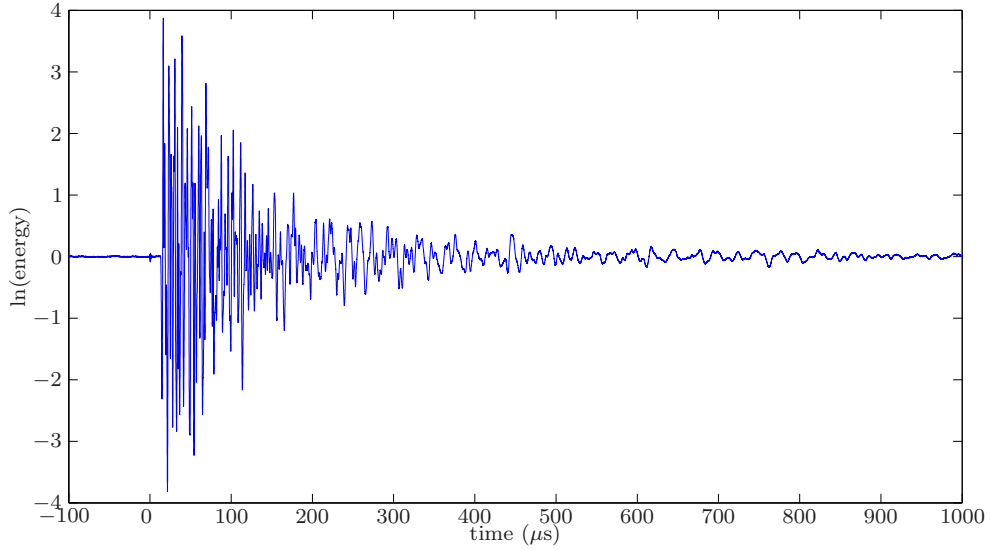


**Figure 7.4:** Typical timesignal of diffuse measurement

In summary, it is noted that variations in the dissipation coefficient  $\sigma$  mainly change the slope of the fall-off – at later times this slope is almost only determined by  $\sigma$ . The diffusivity  $D$  influences the early time behavior, including the peak arrival time and the fall-off slope in the beginning (until 50-100  $\mu\text{s}$ ).

### 7.1.3 Calculation of the energy density evolution $\hat{E}(x, t, f)$ from measurement data

A time-frequency analysis with the following main steps is performed to calculate the measured spectral energy density  $\hat{E}(x, t, f)$  at a certain frequency  $f$  (and at the measurement point  $x$ ). A typical time signal is shown in Fig. 7.4 that is used as an example in the following sections.

1. Divide the time signal into overlapping time windows of length  $\Delta t$ . For the shown results, the window length is set to  $\Delta t = 6 \mu\text{s}$  (i.e. 300 data points) and window overlap of 90 % between consecutive windows is applied.

The Hanning window (used in the next step) gives signal outside of the window center less weight, so the overlap makes sure that the whole time-domain signal

is taken into account for the further calculations. More time points are available if the windows overlap more.

2. Multiply the signal of each time window with the Hanning window (see Fig. 7.5) to smooth the signal edges. As shown in Fig. 7.5, the Hanning window has small side lobes in its spectrum which leads to good properties for time-frequency analysis purposes.
3. Calculate the discrete-time Fourier transform (DTFT) of each individual time window and square it. All the steps until here are done automatically by the Matlab function `spectrogram` which gives the resulting quantity from these three steps – the power spectral density – as one of its outputs. The power spectral density is basically a table of Fourier transforms for every time window centered at the center time of each time window.
4. Determine the spectral energy density of each time window in a certain frequency band by integrating the power spectrum in that bandwidth with width  $\Delta f$  centered around frequency  $f_c$ . The value used for this research is  $\Delta f = 350$  kHz.
5. Construct a table of spectral energy density values that are assigned to discrete time points. The time points are centered in their respective time windows (centering assumes that the statistical signal properties like power spectrum are stationary over the length of the time window).

The resulting quantity is denoted with  $\hat{E}(x, t, f)$ .  $\hat{E}(x, t, f)$  is not the ultrasonic spectral energy density itself, but differs from that by a factor related to transducer sensitivity and a factor relating the measured local mean-square motions detected by the transducer to the local strain and kinetic energy densities. That factor is unknown, but presumed constant [44].

### 7.1.4 Estimation of the expected fluctuations

Eq. (4.1) models the expected value  $\langle E(x, t, f) \rangle$  of the spectral energy. From probability theory, it is known that the best estimate for  $\langle E(x, t, f) \rangle$  is the average of  $N$  measurements of multiple, independent configurations  $C_i$ . The average converges to  $\langle E(x, t, f) \rangle$  if the configurations  $C_i$  are statistically independent.

$$\frac{1}{N} \sum_{C_i}^N \hat{E}_i(x, t, f) \rightarrow \langle E(x, t, f) \rangle \text{ for } N \rightarrow \infty \quad (7.1)$$

Multiple configuration measurements can be obtained by changing the locations of the scatterers in the media [31] or by measuring at different points,  $x_i$ , that have the same solution  $\langle E(x_i, t, f) \rangle$ . With regard to Eq. (4.7) and a specimen with a centered source at  $r = 0$ , this could mean taking measurements on a circle  $r = r_0$ , because by diffusion theory, the predicted spectral energy density  $\langle E(x, t, f) \rangle$  is identical on all points on the circle. Statistical independence would be assured, if the points are separated by at least a specimen thickness.

Even though multiple measurements are possible with the presented measurement setup (this was not the case in [5] because of inconsistent coupling effects), the variance of only one measured curve  $\hat{E}_i(x, t, f)$  with respect to  $\langle E(t) \rangle$  is still of interest to validate curve fit quality.

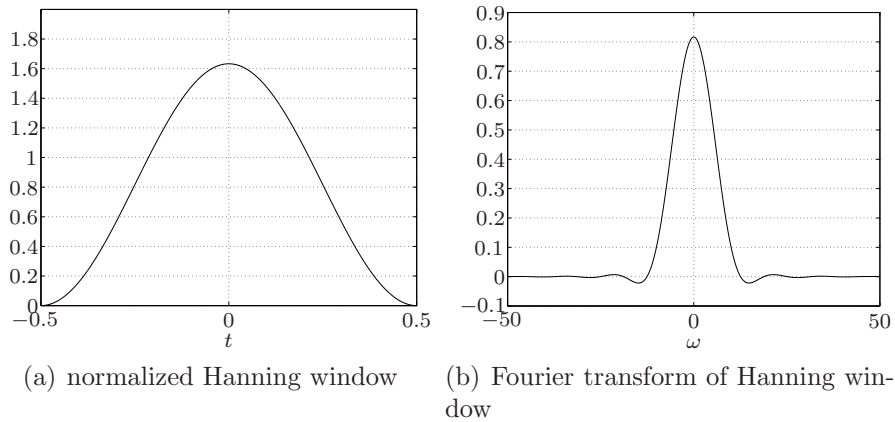


**Figure 7.5:** Hanning window

If stationarity in each time window and independent power spectra in each frequency bandwidth are assumed, the variance can be estimated for small  $\Delta t$  and  $\Delta f$  [44]:

$$\sigma^2 = E[(\hat{E}(x, t, f) - \langle E(x, t, f) \rangle)^2] = \frac{1}{\Delta t \Delta f} \quad (7.2)$$

If Gaussian statistics hold, roughly 70 % of the measured values  $\hat{E}(x, t, f)$  are expected to lie in the interval  $I$ .

$$I(\sigma) = [\langle E(x, t, f) \rangle + \sigma, \langle E(x, t, f) \rangle - \sigma] \quad (7.3)$$

Note that Eq. (7.2) is derived for a rectangular window in [44]. In this research however, a Hanning window is applied to the signal window which accounts less for values outside of the time window center. Hence, a normalization factor is introduced that accounts for the difference between Hanning and rectangular window.

$$\alpha = \frac{\sum_0^{N-1} w(n)}{\sum_0^{N-1} r(n)} = \frac{1}{N} \sum_0^{N-1} w(n)$$

Here,  $N$  is the window length in points,  $w(n)$  the applied window and  $r(n)$  the rectangular window. Eq. (7.2) is then slightly modified (for the Hanning window used in all calculations,  $\alpha = 0.5017$ ).

$$\sigma^2 = E[(\hat{E}(x, t, f) - \langle E(x, t, f) \rangle)^2] = \frac{1}{\alpha \Delta t \Delta f} \quad (7.4)$$

The smaller the  $\Delta f$ , the more exact are the frequency-dependent parameters  $D$  and  $\sigma$  determined from  $\hat{E}(x, t, f)$ , because less averaging over frequency is involved. But a small  $\Delta f$  increases the fluctuations in  $\hat{E}(x, t, f)$  and hence decreases the quality of fit. Low  $\Delta t$  leads to better time resolution, which in turn increases the fitting of the sharp arrival peak, but it also increases the fluctuations because of less averaged discrete energy values and therefore decreases the quality of fit.

The minimum possible  $\Delta f$  which corresponds to only one squared discrete DTFT amplitude value at a certain time, is derived as follows ( $f_s$  is the sampling frequency

and  $N$  the window length).

$$\Delta f_{\min} = \frac{f_s}{N} = \frac{f_s}{\Delta t / f_s} = \frac{1}{\Delta t} \quad (7.5)$$

It is important to note, that  $\Delta f_{\min}$  is independent of the sampling frequency.

### 7.1.5 2D Semi-infinite plate

#### 7.1.5.1 Fit of an approximate solution

In a first attempt to recover the model parameters ( $P_0$ ,  $D$  and  $\sigma$ ) from the experimentally determined spectral energy density  $\hat{E}(x, t, f_c)$  (calculated for a frequency band with center frequency  $f_c$ ), the curve is fit to the approximate two-dimensional model from Eq. (4.7). Only data on a limited time range in which the energy density is clearly above noise level can be considered for the curve fit. This time range depends very strongly on the frequency. Due to higher energy dissipation at higher frequencies, the useful signal length decreases with increasing frequency. This obviously causes fewer time points to be included in the curve fitting procedure which decreases the quality of fit at high frequencies, which in turn leads to a stronger influence on the fluctuations. The time intervals used for the curve fitting method in this section is given in Table 7.1.

Assume Eq. (4.7) to be an approximate model for  $\langle E(x_0, y_0, t) \rangle$ . The distance between the source and transducer is measured to be  $r = 38$  mm.

To make the curve fitting procedure very simple, the natural logarithm is taken on both sides of Eq. (4.7) which gives

$$\ln(\langle E(r, t) \rangle) = \ln(P_0) - \ln(4D\pi) - \ln(t) - \frac{r^2}{4Dt} - \sigma t \quad \forall t \neq 0. \quad (7.6)$$

In that form, a linear regression can be used which will be illustrated in the following. For each data point with  $t > 0$ , the term  $N(r, t) = \ln(\langle E(r, t) \rangle) + \ln(t)$  can be represented as a linear function  $f$  in the variables  $F$ ,  $G$ ,  $H$  and  $t$  which yields

$$N(r, t) = \ln(\langle E(r, t) \rangle) + \ln(t) = f(F, G, H, t) = F + Gt + H/t \quad (7.7)$$

with

$$F = \ln \left( \frac{P_0}{4\pi D} \right) \quad (7.8)$$

$$G = -\sigma \quad (7.9)$$

$$H = -\frac{r^2}{4D} \quad (7.10)$$

As mentioned before, the measured spectral density is denoted by  $\hat{E}$ , so the experimentally determined variable  $\hat{N}(r, t) = \ln(\hat{E}(r, t)) + \ln(t)$  is introduced which should fulfill the following equation in an optimal sense

$$\hat{N}(r, t) = \langle N(r, t) \rangle \quad \forall t \in [t_{\text{start}}, t_{\text{end}}] \quad (7.11)$$

This corresponds to one equation for every discrete time step  $t_i$  and it can be put in the form of a linear matrix equation

$$\underbrace{\begin{pmatrix} 1 & t_1 & 1/t_1 \\ 1 & t_2 & 1/t_2 \\ \dots & \dots & \dots \\ 1 & t_n & 1/t_n \end{pmatrix}}_{\mathbf{A}} \underbrace{\begin{pmatrix} F \\ G \\ H \end{pmatrix}}_{\mathbf{x}} = \underbrace{\begin{pmatrix} \hat{N}_1 \\ \hat{N}_2 \\ \dots \\ \hat{N}_n \end{pmatrix}}_{\hat{\mathbf{n}}} \quad (7.12)$$

Using a least squares estimation of the regression parameters (minimization of the  $L_2$  norm), the solution with the pseudo-inverse matrix is [22]

$$\mathbf{x} = (\mathbf{A}^T \mathbf{A})^{-1} \mathbf{A}^T \hat{\mathbf{n}} \quad (7.13)$$

This solution minimizes the square error

$$\epsilon = \sum_{t_i} (\ln(\langle E(r, t) \rangle) - \ln(\hat{E}(r, t)))^2. \quad (7.14)$$

The solution of the problem will yield the variables  $F$ ,  $G$  and  $H$ . From these, the parameters  $P_0$ ,  $D$  and  $\sigma$  can be obtained using Eq. (7.8) - (7.10).  $P_0$  is a factor

**Table 7.1:** Time windows for 2D curve fit

$f_{\text{center}}$ (MHz)	$t_{\text{start}}$ ( $\mu\text{s}$ )	$t_{\text{end}}$ ( $\mu\text{s}$ )
0.634	12	250
0.732	12	200
0.830	12	150
0.927	12	130
1.025	12	110
1.123	12	90

related to the input energy but also to transducer coupling and other measurement-related factors. Due to this ambiguity it will not be used in the characterization of the material.

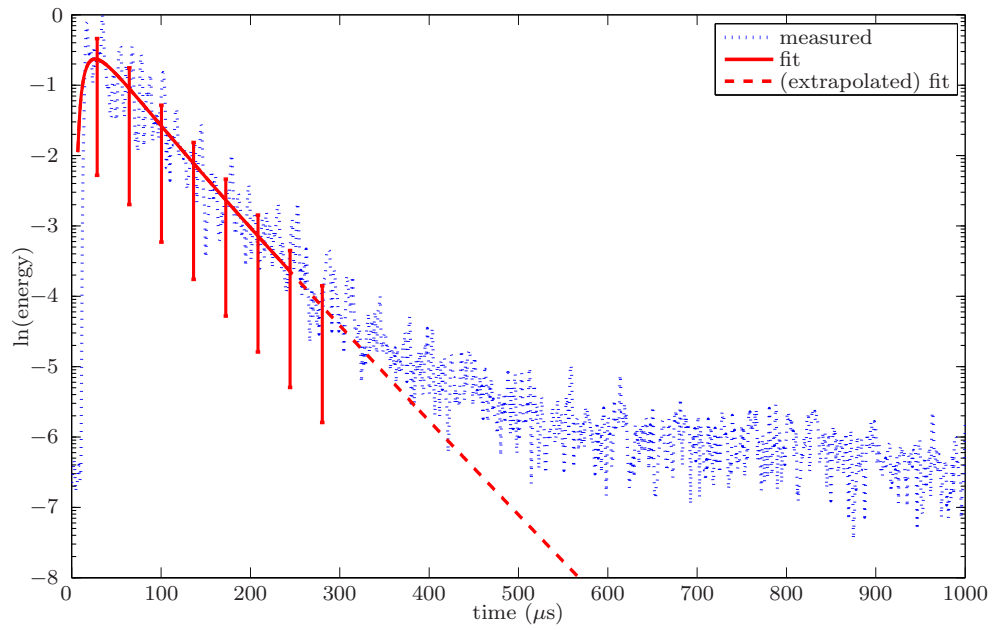
Figs. 7.6, 7.7 and 7.8 show example curve fits in a logarithmic scale corresponding to the time signal shown in Fig. 7.4. The spectral energy density is calculated with the time and frequency windows  $\Delta t = 6\mu\text{s}$  and  $\Delta f = 0.35$  MHz. The error bars correspond to the predicted deviations from Section 7.1.4 caused by the randomness of the media. They are the same for all points and only plotted as examples at some points.

Note that the fluctuations lie randomly above and below the modelled curve which suggests good quality of fit.

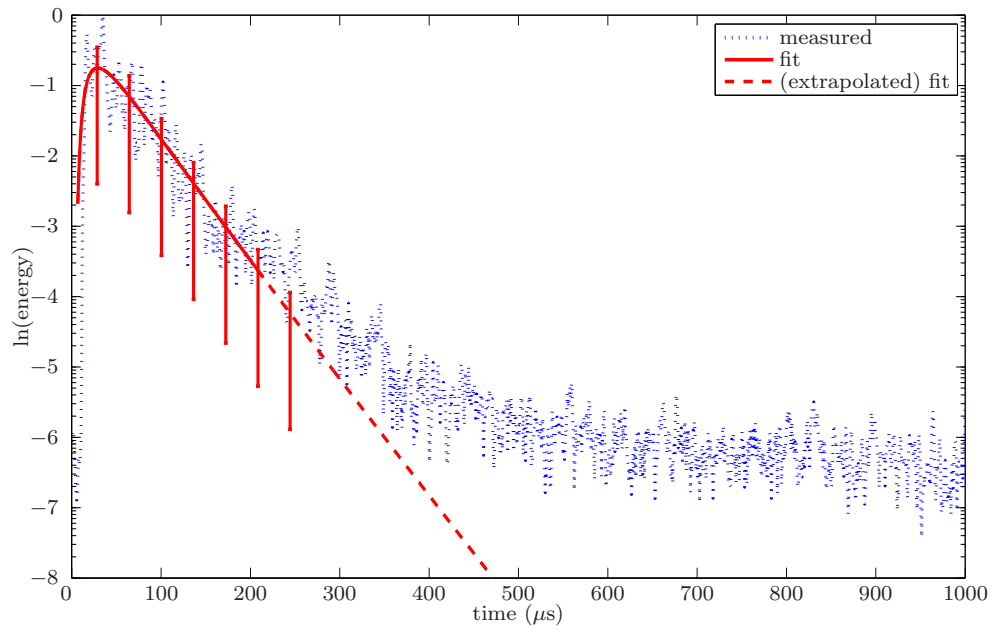
### 7.1.6 Model accuracy

In the following, several points about the accuracy of the application of a 2D semi-infinite plate model to the specimens used and about the assumptions of the ultrasound energy density source to be a temporal and spatial impulse have to be made.

1. The assumption that the sample is two-dimensional is not accurate. The thickness/side length ratio of the sample is 0.61 which does not completely justify neglecting the thickness. Also, comparing measurements of source and receiver on the same side with measurements of source and receiver on different sides lead to different results which can be explained by the underestimation of the

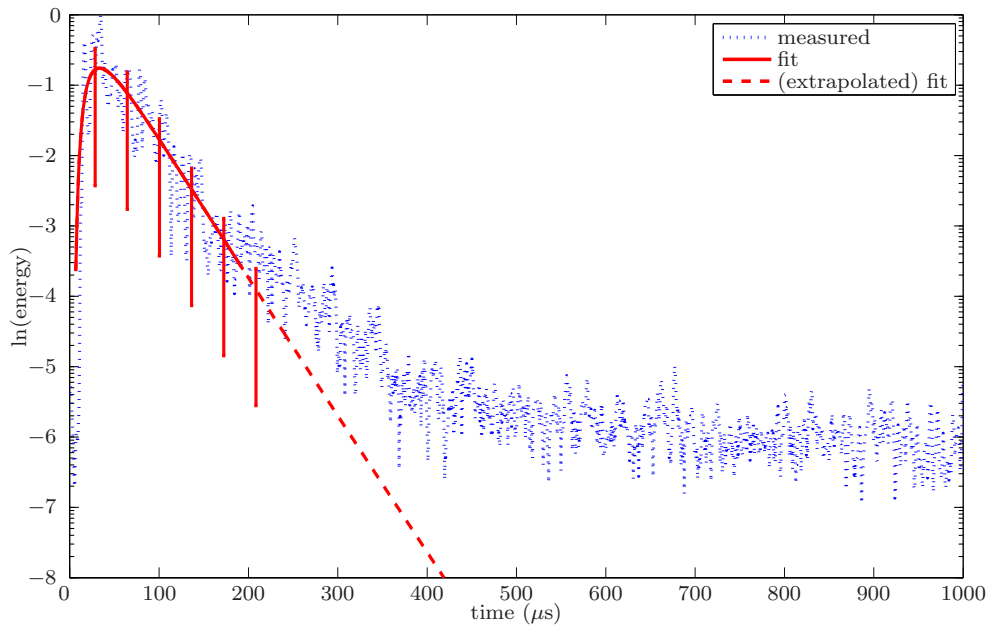


(a)  $f_c = 0.635$  MHz

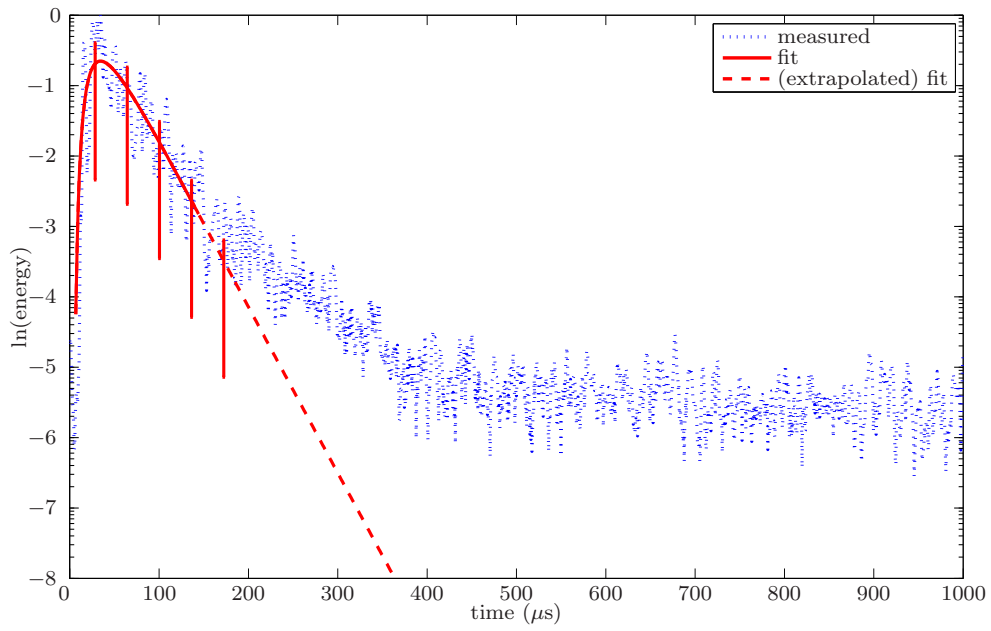


(b)  $f_c = 0.732$  MHz

**Figure 7.6:** Curve fit with the semi-infinite model with the expected deviation as bars

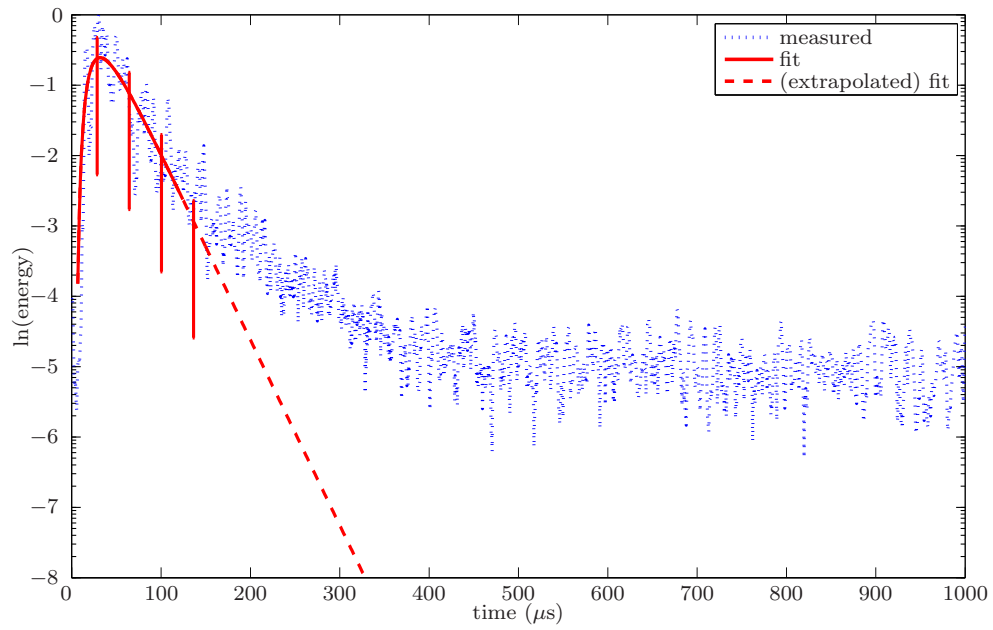


(a)  $f_c = 0.830$  Mhz

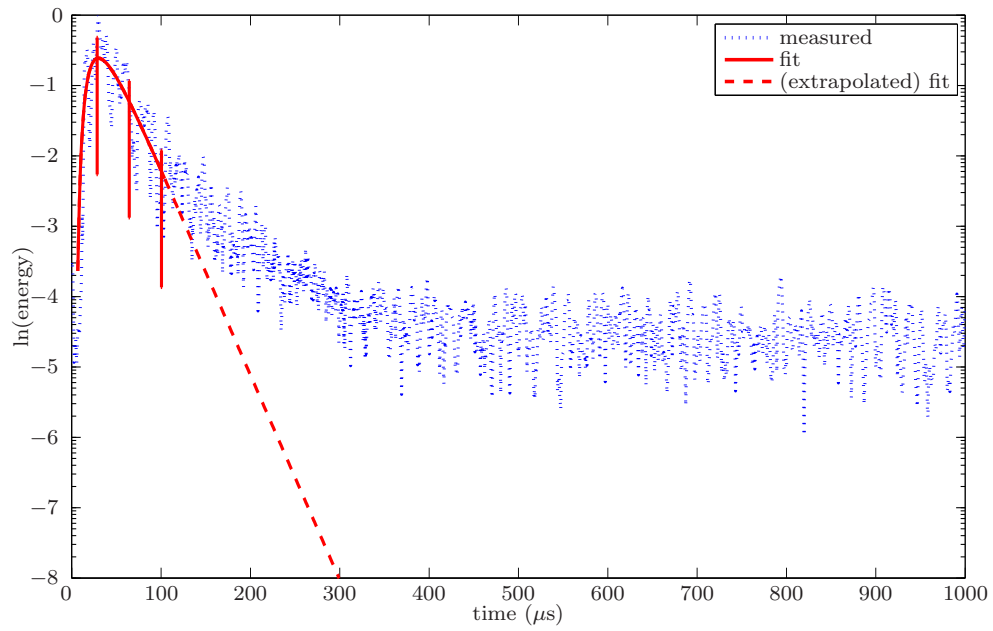


(b)  $f_c = 0.928$  Mhz

**Figure 7.7:** Curve fit with the semi-infinite model with the expected deviation as bars



(a)  $f_c = 1.025$  MHz



(b)  $f_c = 1.123$  MHz

**Figure 7.8:** Curve fit with the semi-infinite model with the expected deviation as bars

source/receiver distance in the case of opposing sides. Using this model can still be justified by its simplicity (it allows linear regression) and that it helps present a first idea of the trends in diffusivity and dissipation. Also the determined values serve as an initial guess for the nonlinear curve fitting procedure.

2. The wave field is not completely scattered immediately after the time of the excitation pulse. It takes the coherent pulse a certain time, that depends on the specific material and geometry of the specimen, to be scattered enough to be considered a diffuse ultrasound energy source. This transition period, that is not taken into account in the model, is expected to lower the diffusivity  $D$ .
3. The source pulse duration is finite and not an ideal pulse, which leads to slight differences from the model, especially at early times. However, a very short pulse, compared to the arrival time of about  $10 - 30 \mu\text{s}$ , is chosen to minimize the error.
4. The source transducer is not actually a spatial pulse but has a relatively large finite size. This leads to a faster arrival of the energy peak than predicted by the model (more energy can be transmitted faster into the specimen). This result will probably increase the recovered  $D$ , because the model makes up for the faster arrival with higher  $D$ .
5. The ultrasound beam spreading (frequency-dependent near-field and far-field effects) of the source transducer is neglected. The influence of this effect is difficult to quantify since it depends on the wavelength and specimen thickness.
6. At very early times (shortly before and after the peak arrival), the fit quality is usually poorer than at later times as can be seen in Figs. 7.6 – 7.8. This can not be attributed to the coherent field since it will arrive faster than the wave field in that time period. Similar results were observed in [45]. Weaver suggested

that the reason is that fewer ray paths take part in the transport of the diffuse energy at very early times, i.e. less implicit averaging takes place and that only later the diffuse energy has explored a larger volume and more paths contribute to the measured field. Also, some of the waves at early times probably have not scattered multiple times, so the energy transport is not yet fully diffuse. Additionally, the effective time window at early times is shorter than the actual window because the majority of the energy arrives during a small part of that window, i.e. the energy is not equally distributed over the time of the window as it is assumed by centering the discrete time in their respective time window. This will mostly influence the  $D$  parameter, because it diminishes at later times.

The source related inaccuracies could be reduced by modelling the source term  $P(r, t, f) = P_0 e^{-at} e^{-br}$  which is a better approximation to reality and could improve the quality of the curve fit. However, it will complicate the solution of the diffusion equation (4.1) which will also require more complicated non-linear curve fitting algorithms. The geometry effects will be investigated further with the 3D finite cuboid model in the following Section 7.1.7.

#### 7.1.6.1 Evaluation of the recovered parameters

The recovered parameters  $D$  and  $\sigma$  are plotted over frequency in the following section. In Figs. 7.9 and 7.10, two samples of the same damage level (medium damage) are compared and a good agreement is attested which illustrates that the measurement method in this research gives consistent results. To compare the results better, parameters from ten measurements per sample are averaged. The diffusivity  $D$  shows the expected decreasing behavior with increasing frequency known from the literature for concrete samples. The dissipation  $\sigma$  also increases with frequency. A linear regression for the ASR 6-1 sample of the following form is also included in Fig. 7.10

$$\sigma(f) = mf + c \tag{7.15}$$

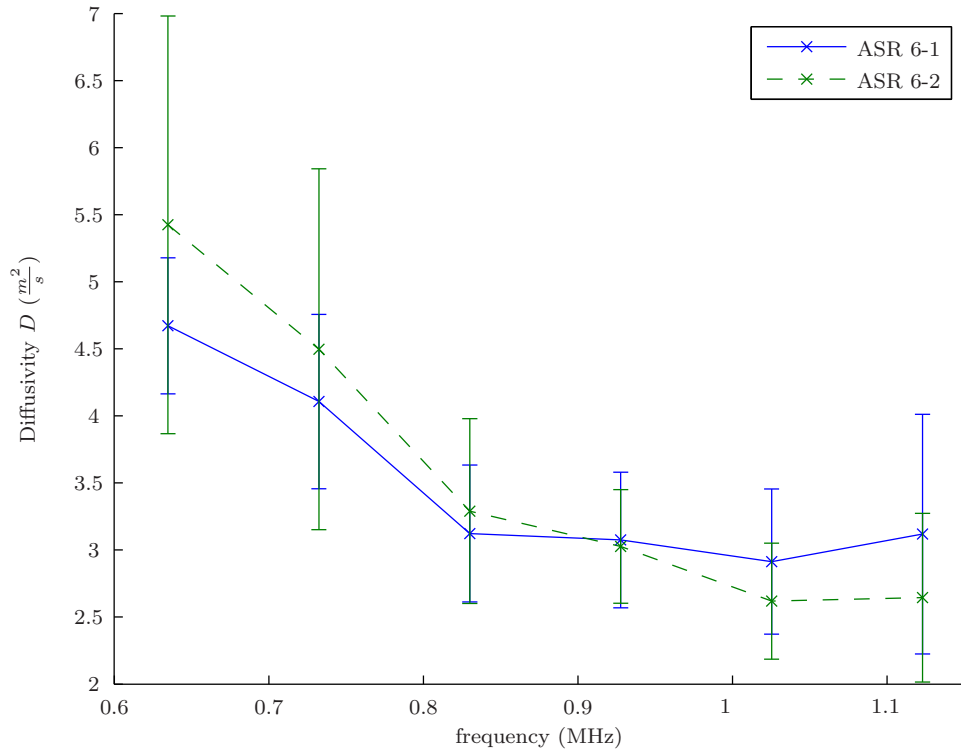


**Figure 7.9:** Diffusivity  $D$  for two ASR damaged samples with same damage level with 2D semi-infinite plate model

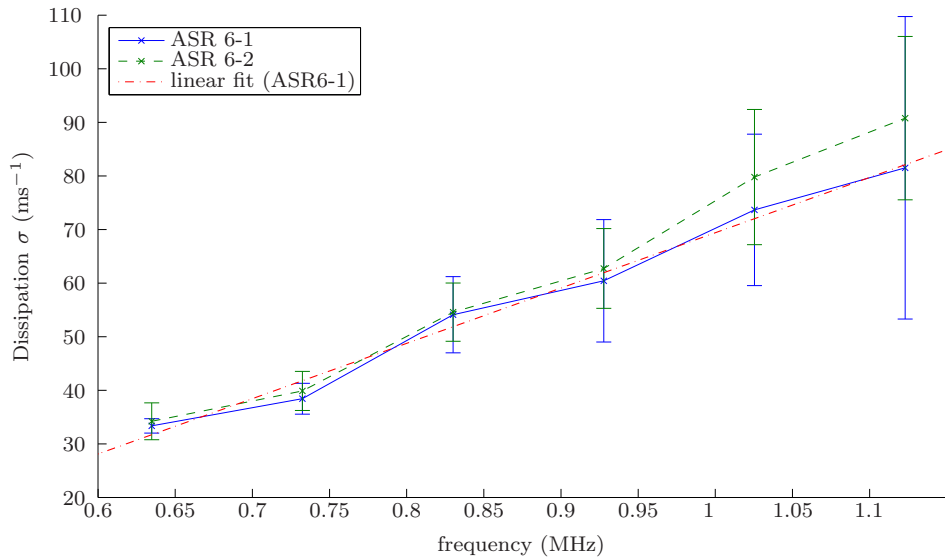


**Figure 7.10:** Dissipation  $\sigma$  for two ASR damaged samples with same damage level with 2D semi-infinite plate model

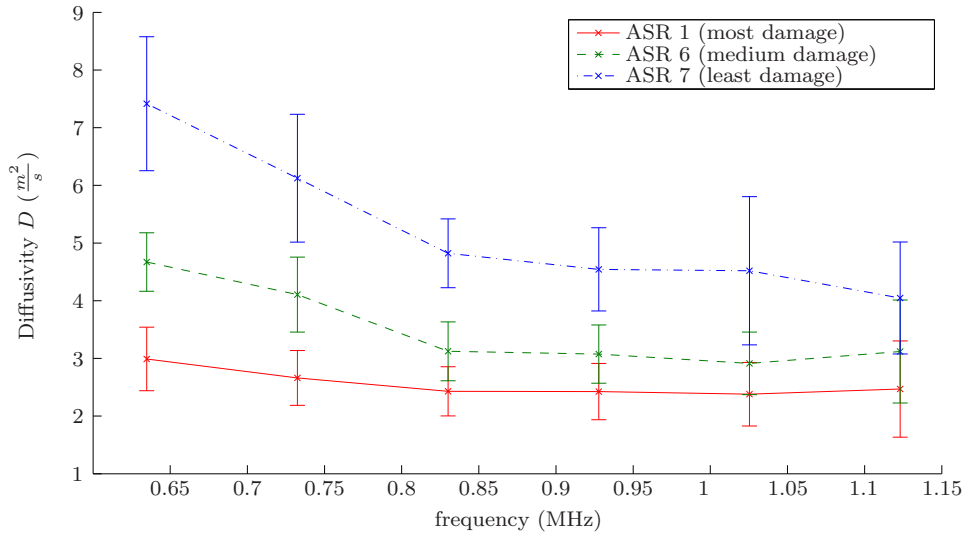


**Figure 7.11:** Diffusivity  $D$  for ASR damaged samples with 2D semi-infinite plate model

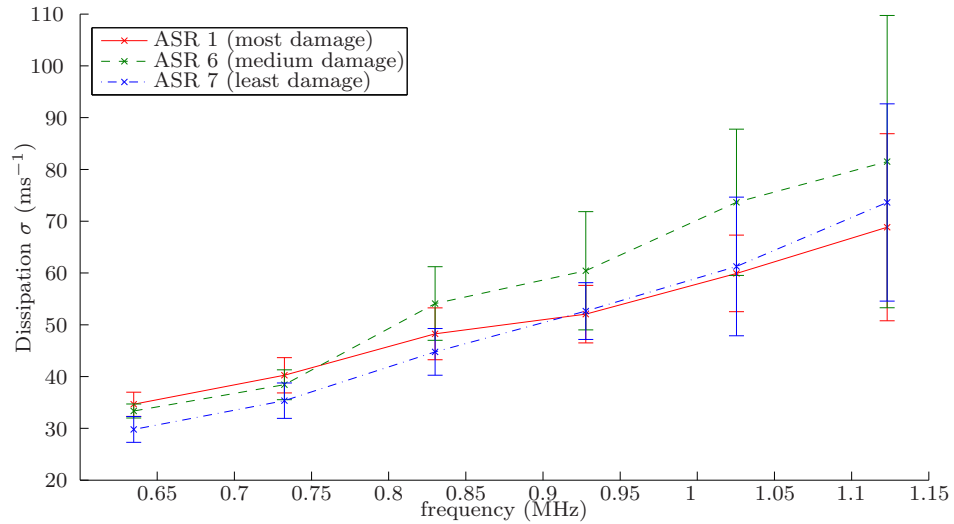


**Figure 7.12:** Dissipation  $\sigma$  for ASR damaged samples with 2D semi-infinite plate model

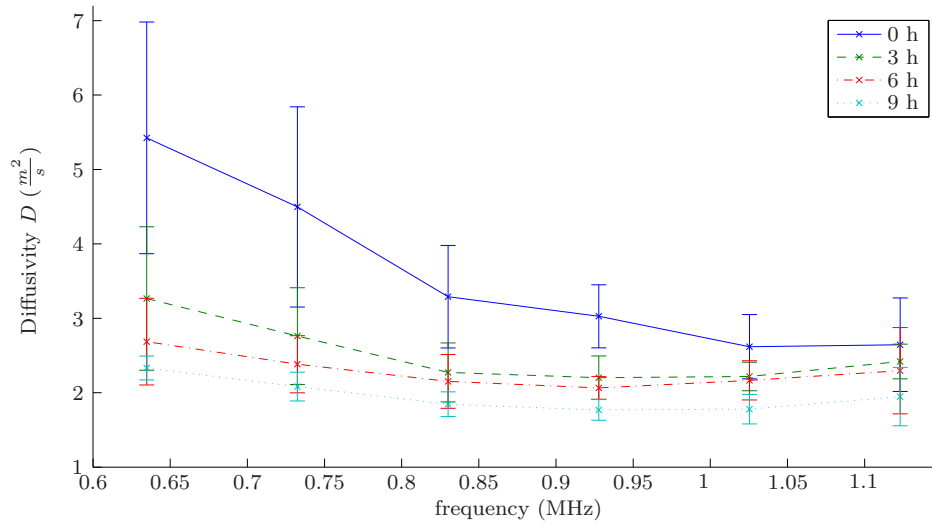


**Figure 7.13:** Diffusivity  $D$  for thermal damaged samples with 2D semi-infinite plate model

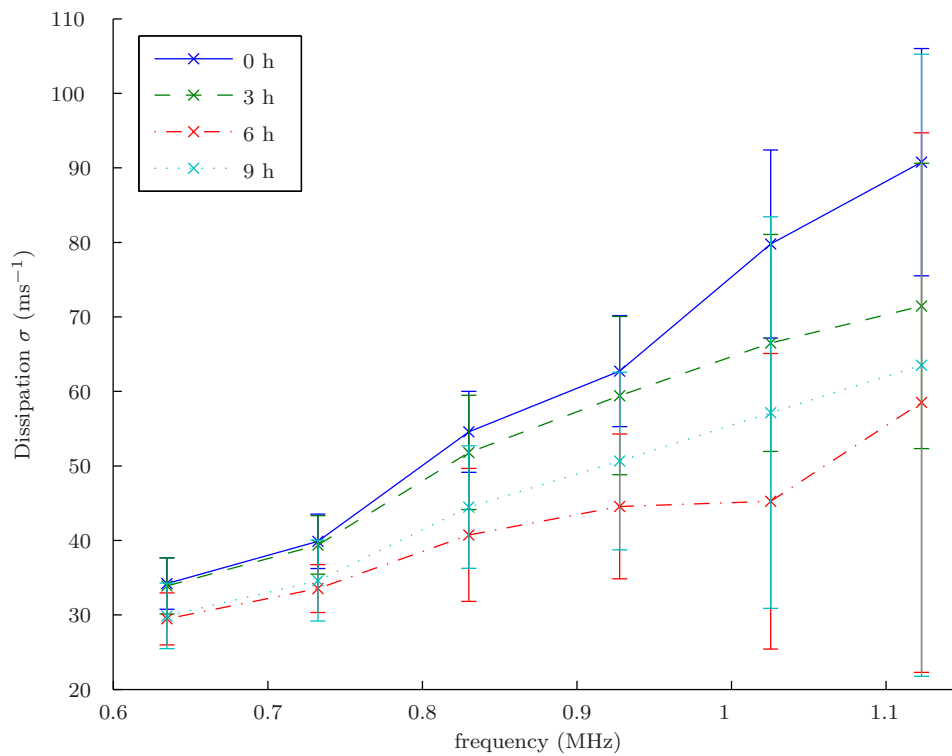


**Figure 7.14:** Dissipation  $\sigma$  for thermal damaged samples with 2D semi-infinite plate model

The regression is done using a least-square approximation in the curve fitting tool of the Matlab Curve Fitting Toolbox. The regression curve shows that the dissipation  $\sigma$  shows good linear behavior, there is however a horizontal offset ( $c \neq 0$ ) if the line is extended to  $f = 0$ .

The good agreement of the curves justifies actually comparing different samples after averaging parameters from several measurements per sample, despite the difficult transducer coupling conditions. The time-frequency analysis is conducted in the same way for all specimens and measurements. The fitting times are mentioned in Table 7.1, the time window is  $\Delta t = 6\mu s$ , the frequency window is  $\Delta f = 350$  MHz.

Next, consider Figs. 7.11 and 7.12. Again, these parameters are determined by averaging parameters from 10 - 14 separate measurements per sample to achieve better comparability. The diffusivity  $D$  shows a clear trend of lower  $D$  for more damaged samples. The dissipation for all three damage levels is almost identical. The diffusivity curves get closer for higher frequencies. The reason is probably higher measurement uncertainty due to lower signal-to-noise ratio and fewer usable data points for the curve fit.

For the thermal damage, one of the ASR damaged samples (ASR 6-2) is heated at 120° C. It is cyclically heated in intervals of 3 h for 9 h total; between every interval the sample cools down before the measurement is taken. The resulting extracted parameters are shown in Figs. 7.13 and 7.14. As mentioned in Section 2.2, heating at a temperature of 120° C leads to microcracking. It is expected that the heating and the resulting microcracking will cause more scattering, thus slowing down the diffusion process. It is clearly visible that with longer heating times, diffusivity decreases noticeably. Dissipation  $\sigma$  is not identical for all specimens, however a clear pattern in terms of damage is not recognizable which leads to the suspicion that the differences are due to measurement uncertainties.

### 7.1.7 Finite 3D cuboid

#### 7.1.7.1 Fit of an approximate solution

For the finite model, Eq. (4.10) is used. The coordinates of source and receiver are  $(x_0, y_0, z_0) = (0.0375 \text{ m}, 0.0375 \text{ m}, 0.046 \text{ m})$  and  $(x, y, z) = (0.012 \text{ m}, 0.012 \text{ m}, 0 \text{ m})$ . The  $(x, y, z)$  coordinate represents the position of the receiver that is close to the specimen corner. The specimen dimensions are  $a \times b \times c = 0.075 \text{ m} \times 0.075 \text{ m} \times 0.046 \text{ m}$ . The Matlab function `lsqnonlin` is used for the curve fitting procedure. The advantage of using this function is the possibility of setting weighting intervals. This allows to force the curve fitting function to maximize fit quality in important intervals. For a good fit of the diffusivity  $D$ , the early part of the signal (10-50  $\mu\text{s}$ ) is important, for the dissipation  $\sigma$  the later part is more important. Portions in the middle can be weighted less. The procedure minimizes the weighted square error

$$\epsilon = \sum_{t_i} w_i (\langle E(r, t) \rangle - \hat{E}(r, t))^2. \quad (7.16)$$

These weighting intervals depend on frequency and typical weighting intervals are given in Table 7.2; for every frequency two intervals are given (an early interval important for  $D$ , and a later interval important for  $\sigma$ ). It must be noted that the indices of the infinite series in Eq. (4.10) are limited to  $n = m = 1, 2$  and  $l = 1, 2, 3$ . These values are determined empirically. It is however expected that the propagation direction in thickness direction (represented by the index  $l$ ) is dominant so it is reasonable to include more terms for that direction. Also, a larger number of terms does not change the recovered parameters and thus would only increase computational effort.

Similar to Section 7.1.5.1, example plots of the 3D curve fits are given in the Figs. 7.15 to 7.17. They correspond to the same time signal shown in 7.4. Again, the fluctuations lie randomly above and below the modelled curve which suggests good quality of fit.

**Table 7.2:** Weighting intervals for 3D curve fit

$f_{\text{center}}$ (MHz)	$t_{\text{start}_1}$ ( $\mu\text{s}$ )	$t_{\text{end}_1}$ ( $\mu\text{s}$ )	$t_{\text{start}_2}$ ( $\mu\text{s}$ )	$t_{\text{end}_2}$ ( $\mu\text{s}$ )
0.634	8	40	220	330
0.732	8	40	220	330
0.830	8	40	200	280
0.927	8	40	150	250
1.025	8	40	100	200

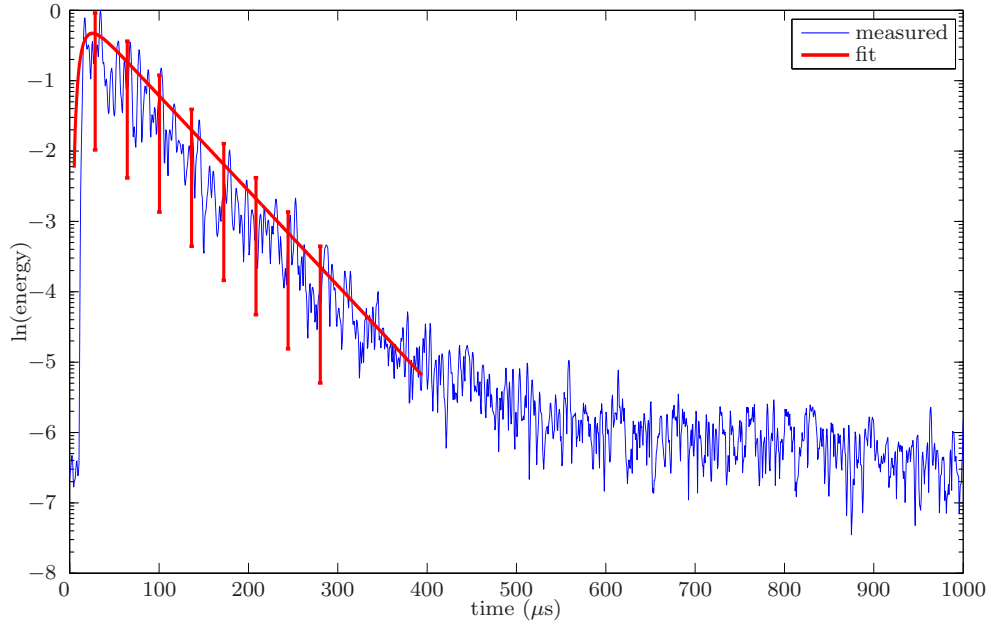
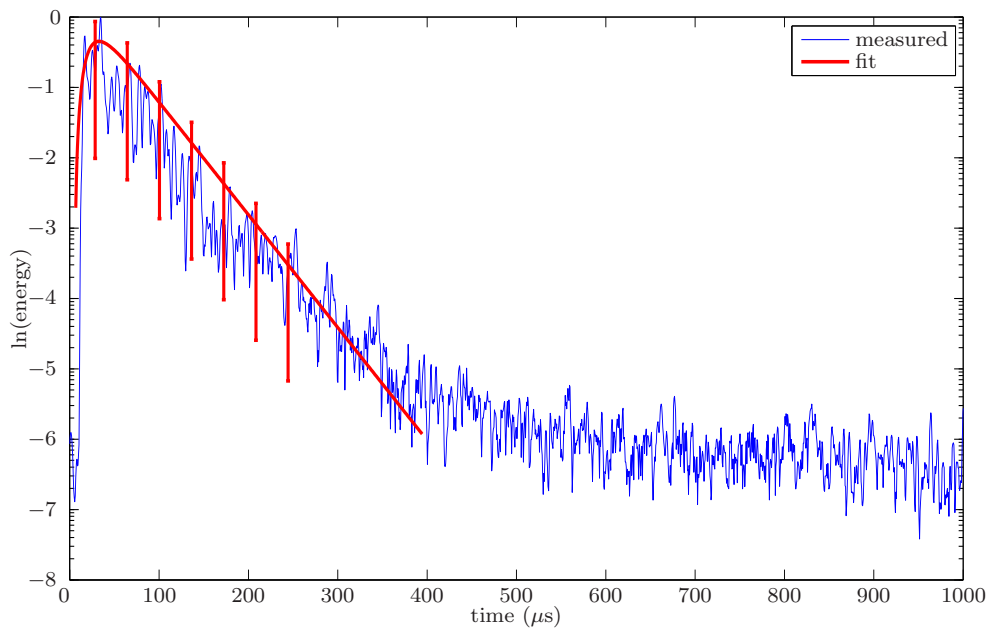
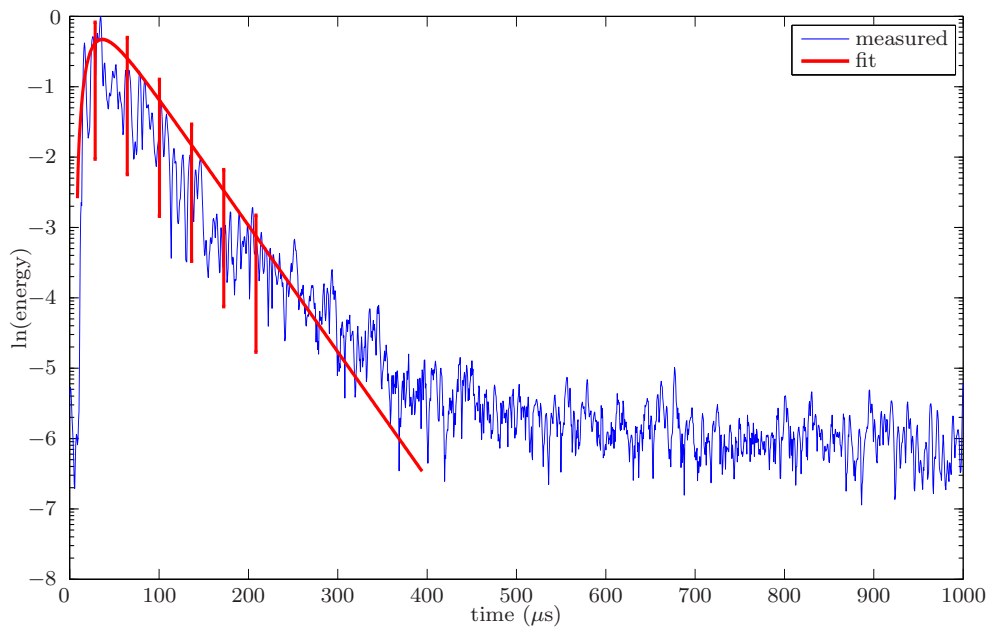


**Figure 7.15:** Curve fit with the finite model with the expected deviation as bars for 0.635 MHz

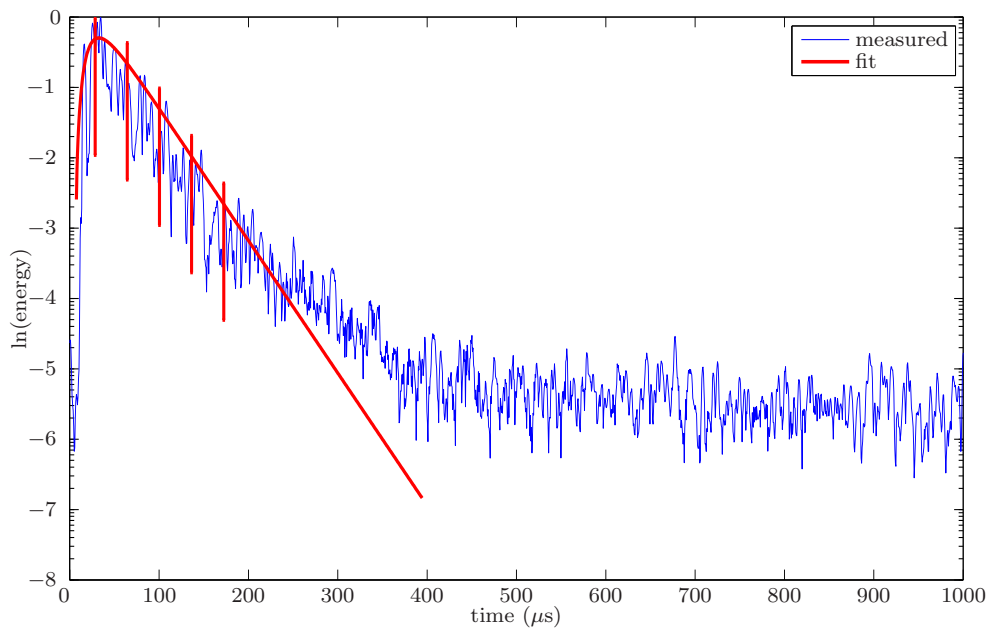


(a)  $f_c=0.732$  Mhz

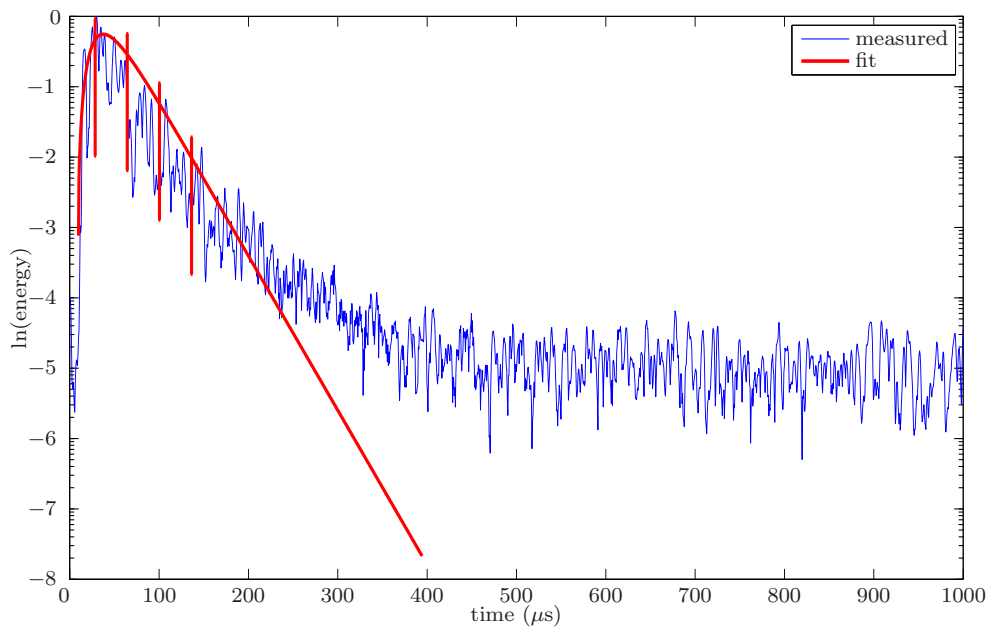


(b)  $f_c=0.830$  Mhz

**Figure 7.16:** Curve fit with the finite model with the expected deviation as bars



(a)  $f_c = 0.928$  Mhz



(b)  $f_c = 1.025$  Mhz

**Figure 7.17:** Curve fit with the finite model with the expected deviation as bars

### 7.1.7.2 Evaluation of the recovered parameters

As in Section 7.1.6.1, the parameters  $D$  and  $\sigma$  are plotted over frequency.

First, consider ASR damage. In Figs. 7.18 and 7.19, the parameters are plotted. The plotted parameters are results of averages of 8-10 measurements. A trend is visible that also for the complete 3D model the diffusivity  $D$  decreases with increasing damage while the dissipation remains almost unchanged. It has to be mentioned that the error bars are much larger than with the 2D model and that the curves for the measurements are closer together. These larger variations probably stem from the significantly larger number of degrees of freedom (and with that more uncertainties) in the model and the far more complicated nonlinear curve fitting method.

When one looks at Figs. 7.20 and 7.21, similar trends to the 2D model are visible. With increased heating time and with that more microcrack damage, diffusivity  $D$  decreases. The same flaws of bigger error bars and closer curves as with ASR damage are also observed.

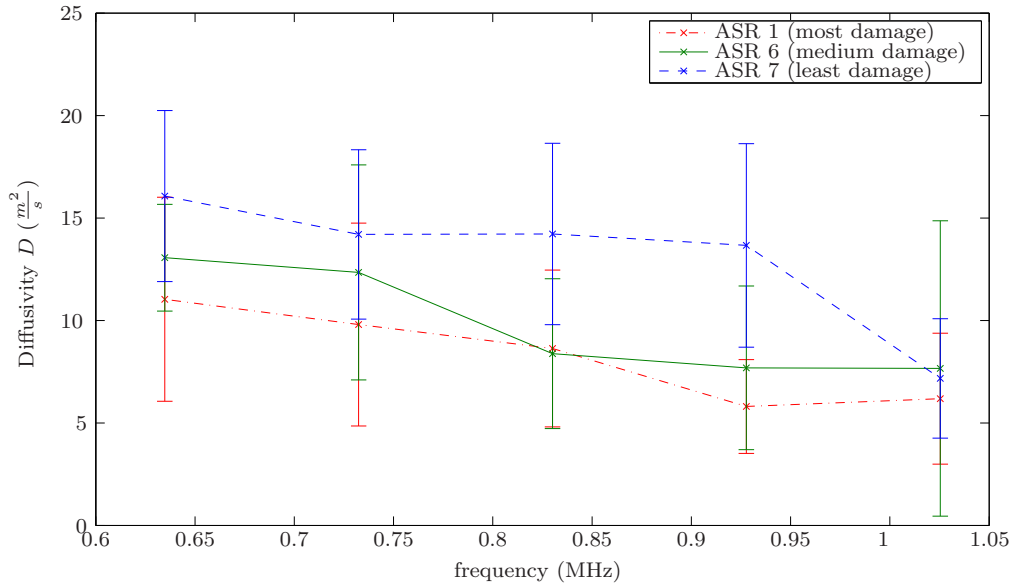


**Figure 7.18:** Diffusivity  $D$  for ASR damaged samples with 3D finite cuboid model

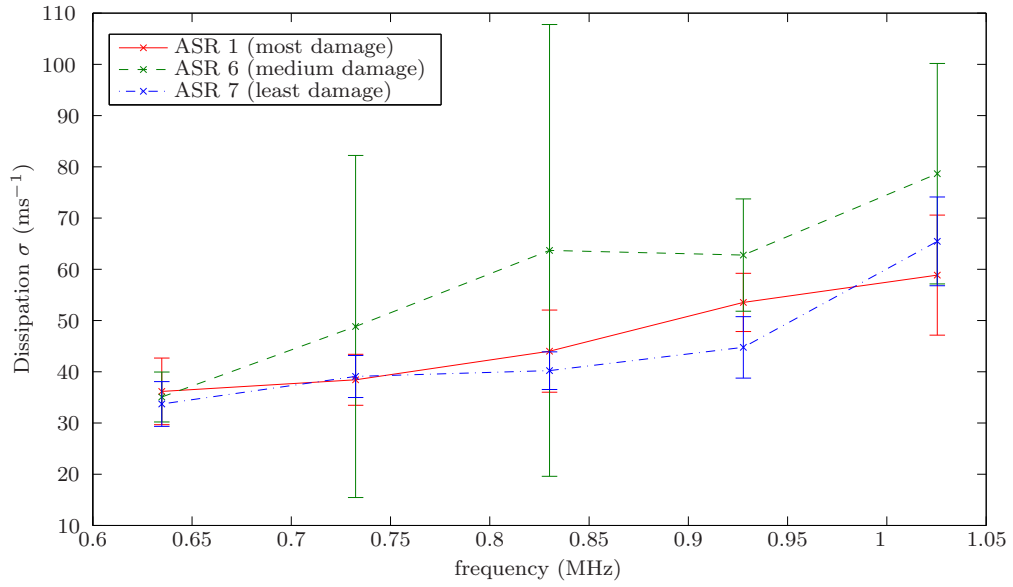


**Figure 7.19:** Dissipation  $\sigma$  for ASR damaged samples with 3D finite cuboid model

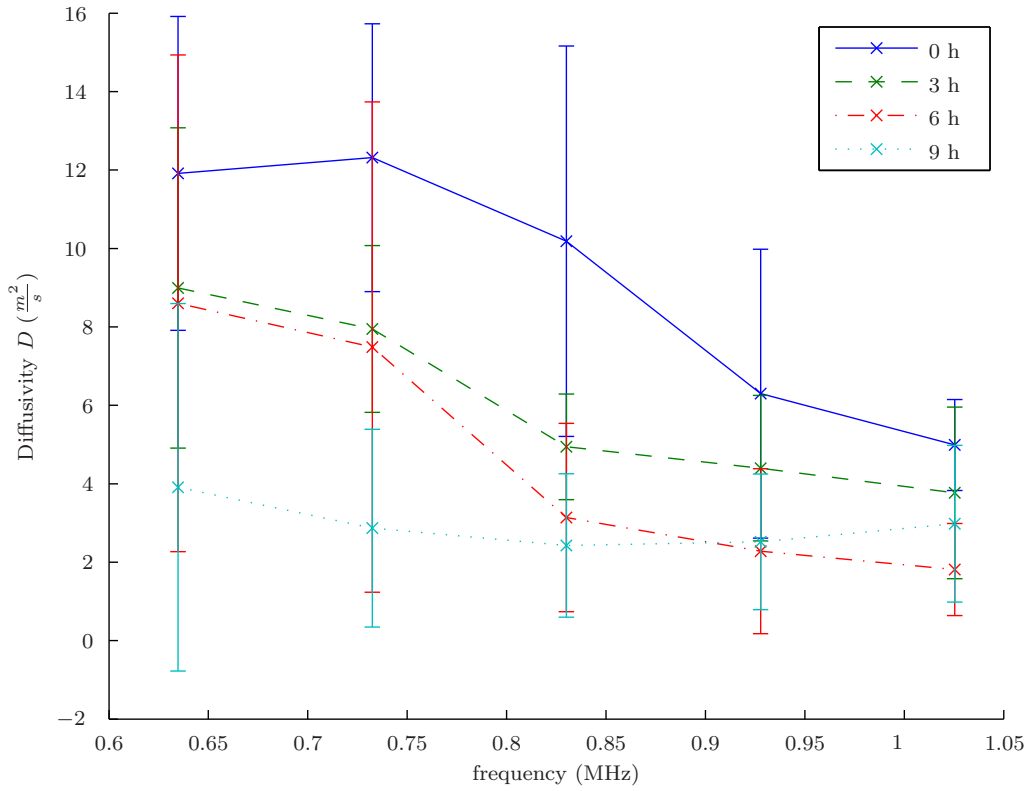


**Figure 7.20:** Diffusivity  $D$  for thermal damaged samples with 3D finite cuboid model

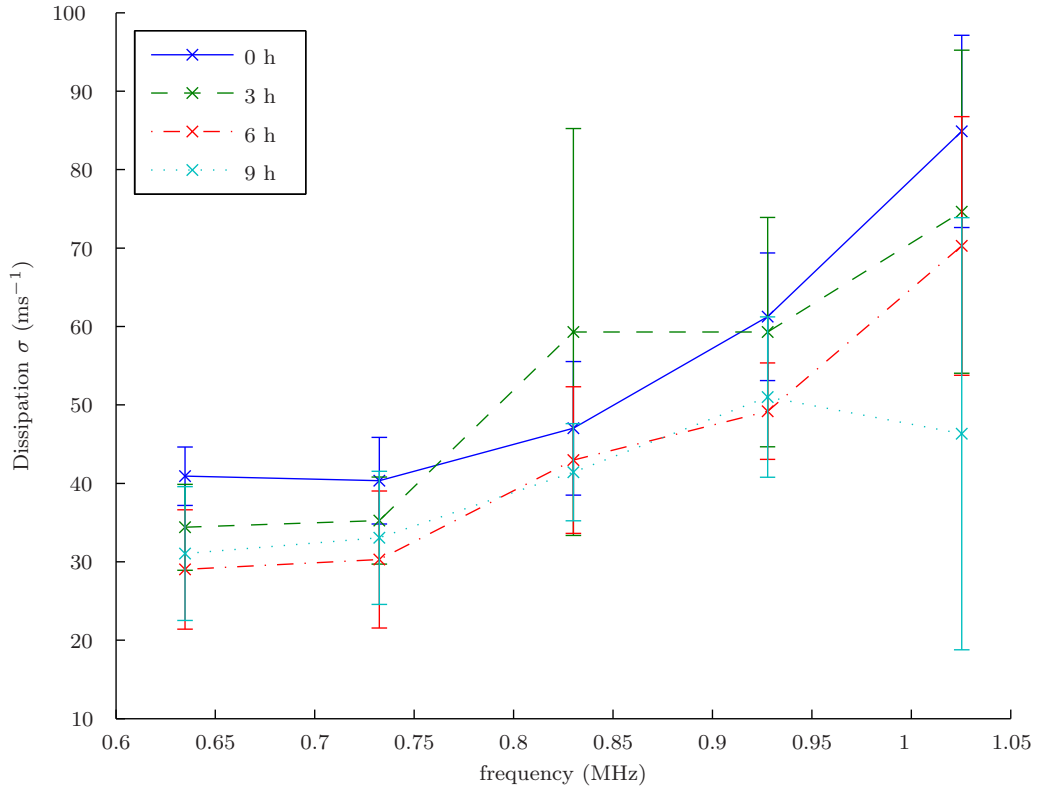


**Figure 7.21:** Dissipation  $\sigma$  for thermal damaged samples with 3D finite cuboid model

### 7.1.8 Conclusions

1. The recovered diffusivity and dissipation values are in the expected range of magnitude since they are in the same range as in [5] and [2].
2. The diffusivity clearly shows the trend of decreasing magnitude with increasing damage. The increased scattering caused by microcracks slows down the energy transport in the material which leads to a lower value of  $D$ .
3. The dissipation  $\sigma$  is almost identical for all different damage levels. This conforms with the theory that predicts that scattering has no influence on the intrinsic absorption of the material, primarily of the cement paste.

4. The ability to distinguish between intrinsic and extrinsic components of attenuation is clearly visible and proves an important advantage of the diffuse method over coherent methods.
5. The difference of absolute values in the diffusivity  $D$  between the 2D and the 3D solution can be explained by an underestimation of the source/receiver distance in the 2D model. The distance is assumed to be 38 mm (the projection of the distance into the plate plane) even though the travel path is longer because of the considerable thickness of the material and scattering in three dimensions instead of only two. Lower diffusivity values are the consequence of the 2D model.
6. The pulse excitation has the advantage that a broad range of frequencies can be excited at the same time which considerably decreases measurement times which would be needed for single frequency tone burst excitation.
7. The spatial averaging of the recovered parameters (which is made possible by the newly designed fixture) leads to far better results. Single measurements do not give a clear indication of damage because of high uncertainties.
8. The necessity of a high signal-to-noise ratio to reliably recover the parameters is a clear disadvantage of the method. The high attenuation in concrete limits the sample size even with the high voltage pulse generator used in this research.
9. The method is shown to work with the samples used in this research. To fully justify using a 2D model (which allows far easier curve fitting) it should be considered to cast samples that resemble a plate structure more than the samples used.

## 7.2 Velocity measurements

As a comparison to the diffuse method, a coherent method in the form of a velocity measurement is also applied to the samples. Usually this is done comparing the time of flight through one thickness of the sample using two transducers and the time

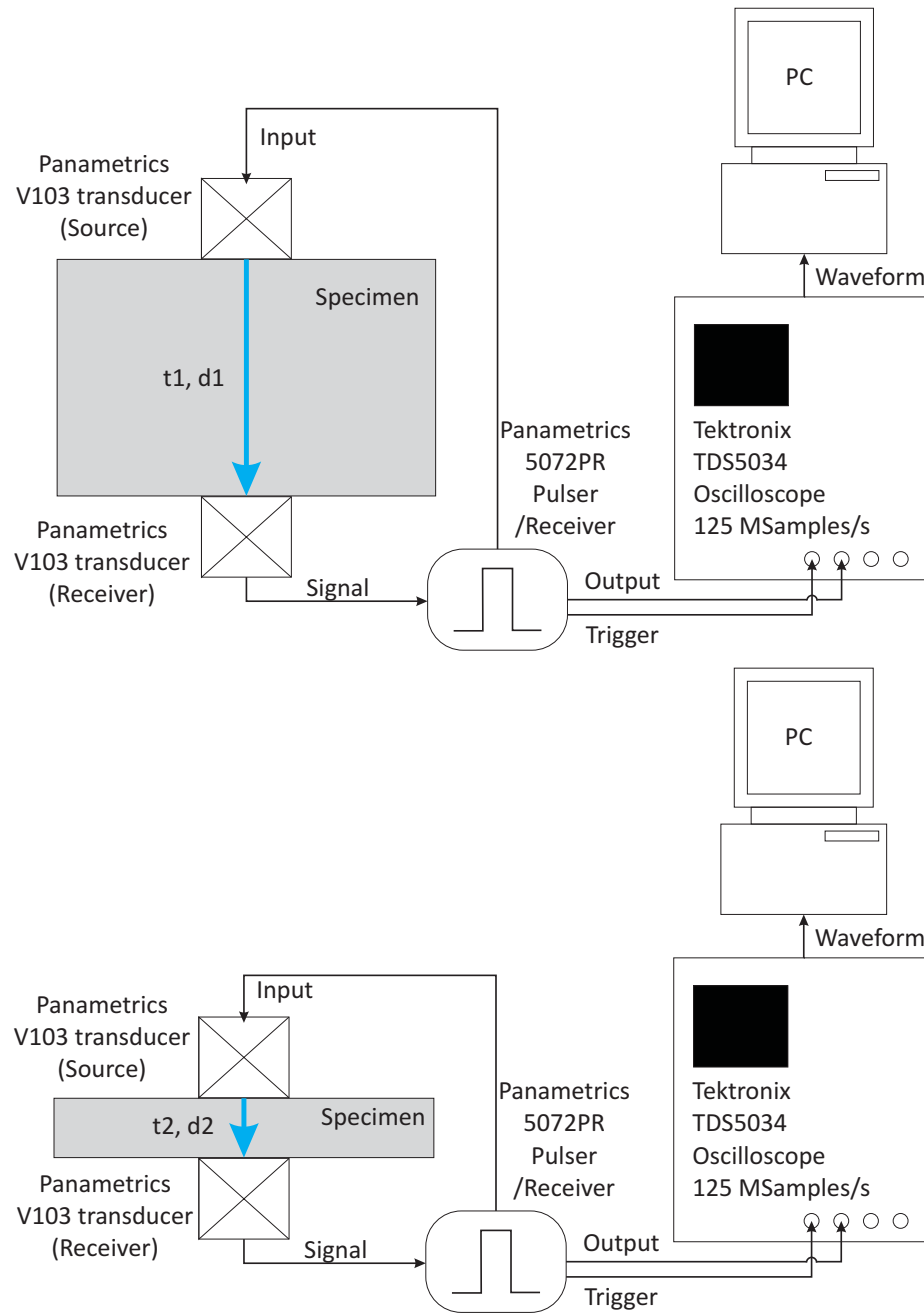


Figure 7.22: Setups for velocity measurement

of flight through twice the thickness using one transducer in pulse echo mode. The two measurements are necessary to systematically remove transducer delays. Since concrete is a highly dissipative and scattering medium, the pulse-echo part can not be used since no clear reflection can be identified in the time signal. Instead, two samples of different thickness are used. This way, only the time of flight through one thickness of the respective sample is necessary and it is still possible to minimize the transducer delays. The measurement setups are shown in Fig. 7.22. The source and receiver are aligned to avoid scattering effects as much as possible. Even though Fig. 7.22 only shows the epicenter setup of the transducers, five measurements at different points are actually conducted for each sample. This is necessary because of slight thickness variations ( $< 1$  mm) of the samples.

### 7.2.1 Measurement setup description

For the velocity measurement, the same transducers are used as for the diffuse field measurement (1 MHz broadband). The only difference is that the receiver is left in its original state and does not have an attached cone. The signal is recorded and amplified with 2500 record points at 125 MHz, which corresponds to  $20 \mu\text{s}$  of signal which is enough to see the first arrival of the wave on the opposing side.

### 7.2.2 Calculation of the velocity

After the time of flight for both specimens and the respective thicknesses are determined, the velocity can be determined with the formula

$$v = \frac{d_1 - d_2}{(t_1 + \tau_t) - (t_2 + \tau_t)} = \frac{d_1 - d_2}{t_1 - t_2} \quad (7.17)$$

where  $\tau_t$  are the combined transducer delays which obviously cancel out. To achieve the maximum amount of averaging, all combinations of the ten measurement points (five per sample) are used in Eq. (7.17) to determine velocities, which are then averaged to one velocity.

**Table 7.3:** Velocities of ASR damaged samples

Sample	velocity (m/s)
ASR 1 (most damage)	4703
ASR 6 (medium damage)	4632
ASR 7 (least damage)	4865

This procedure is done for concrete samples of different ASR damage levels, very similar to the diffuse section. The determined velocity are shown in Table 7.3.

### 7.2.3 Conclusion

The velocity measurements do not give any quantitative indications of damage. In fact, the specimens with the most damage have higher velocity than the ones with medium damage. This may be caused by uncertainties in the measurement, but indicates that the change of velocity is not large enough to be a quantitative measure of the microcracks associated with ASR damage.

## 7.3 *Effective medium theory*

In the following, the theory that was derived in Chapter 5 is used to determine effective parameters of composite materials.

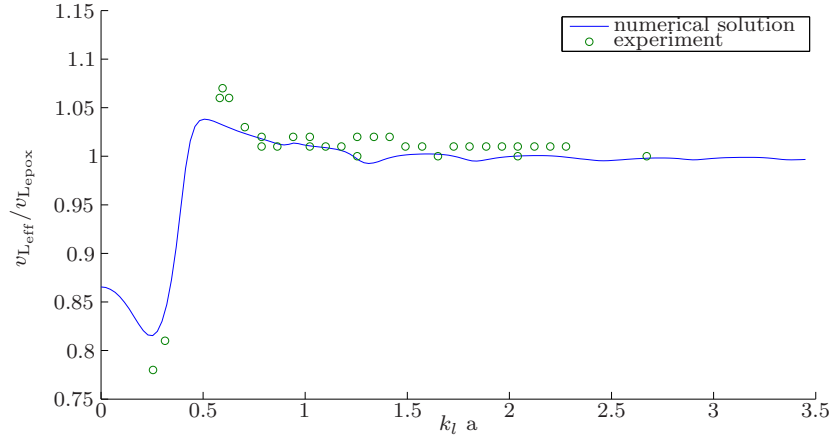
### 7.3.1 Two-phase composite

In a first step, a two-phase material is investigated. The material is a lead/epoxy composite. The material properties of both parts of the composite are given in Table 7.4. The attenuation in the materials is assumed to increase linearly with frequency, i.e.  $k''_{l,s} = m_{l,s}\omega$  (see Eq. (3.32)) [18]. Velocity and attenuation are determined numerically and the velocity is then compared to experimental data that was determined by Kinra et al. [20].

The comparisons are made for 5% volume fraction and 15% volume fraction. The results are plotted in Figs. 7.23 - 7.24. One can see that there is good agreement between the numerical solutions and the experimental results for the whole frequency

**Table 7.4:** Material properties for lead/epoxy composite

Material	Density (kg/m <sup>3</sup> )	$c_l$ (m/s)	$c_s$ (m/s)	$m_l$ (s/m)	$m_s$ (s/m)
lead	11300	2210	860	$0.38 \times 10^{-5}$	$0.99 \times 10^{-5}$
Epon 828z	1202	2640	1200	$0.64 \times 10^{-5}$	$0.14 \times 10^{-4}$

**Figure 7.23:** Effective longitudinal wave speed versus frequency for lead/epoxy (5% volume fraction) composite and experimental data by Kinra et al.

range of the provided experimental data. However, it has to be noted that numerical errors occur for higher volume fractions. First signs can already be seen in Figs. 7.25 and 7.26. The peak at  $ka = 0.966$  is entirely artificial. This problem (the solution diverges from the correct solution at some frequency and returns to the correct solution for a slightly higher frequency) is even more severe for higher volume fractions. It is likely that the problem is caused by the presence of multiple solutions to the dispersion equation (5.16) [15].

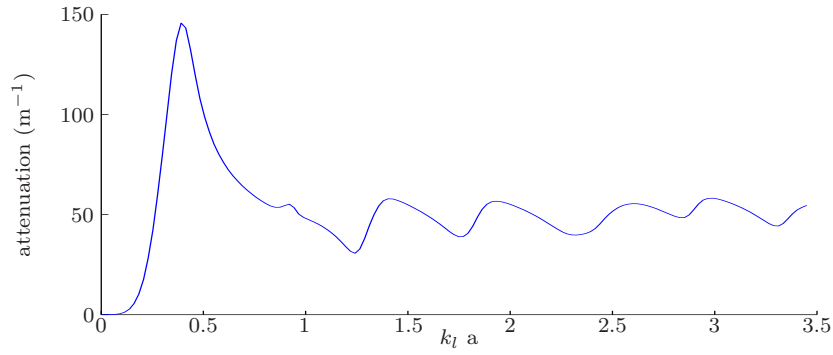


**Figure 7.24:** Coherent attenuation of longitudinal wave speed versus frequency for lead/epoxy (5% volume fraction) composite

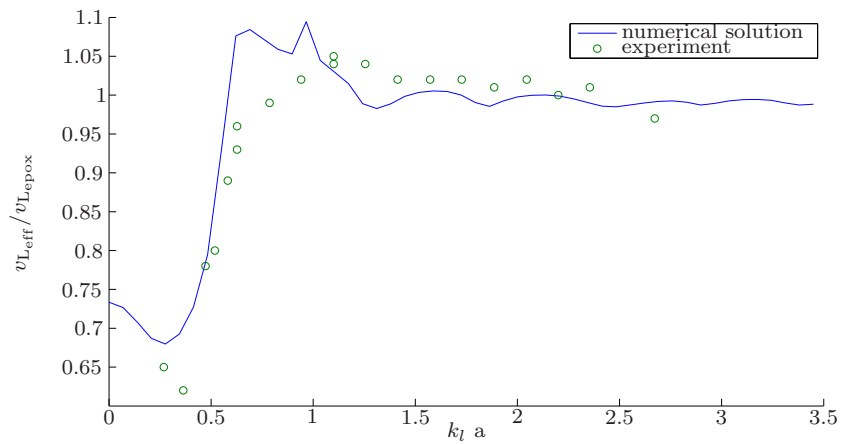


**Figure 7.25:** Effective longitudinal wave speed versus frequency for lead/epoxy (15% volume fraction) composite and experimental data by Kinra et al.

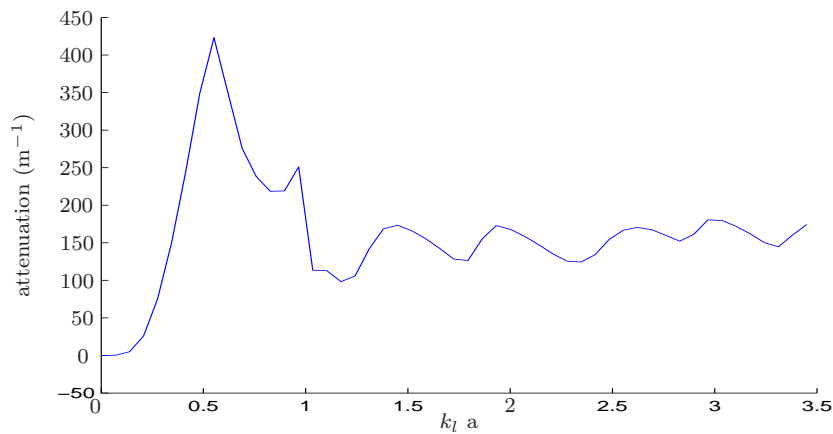


**Figure 7.26:** Coherent attenuation of longitudinal wave speed versus frequency for lead/epoxy (15% volume fraction) composite

### 7.3.2 Concrete as a multi-phase composite

In this section, the theory from Chapter 5 is applied to multi-phase materials. The material presented here is concrete as a classical and widely used composite. The numerical results are compared to experiments conducted in [17]. For these experiments, three different concrete specimens were used. The first specimen (Specimen 1) contained sieved coarse limestone aggregates with diameters between 9.5 and 37.5 and a volume fraction of 67%. The second one (Specimen 2) contained sieved fine limestone aggregates with diameters between 2.36 and 12.5 mm and a volume fraction of 65%. The third specimen (Specimen 3) contains graded aggregates with diameters between 1.18 and 37.5 mm and the total aggregate volume fraction is 76%.

The results are compared in Figs. 7.27 to 7.32. Effective longitudinal velocity  $v_{L_{\text{eff}}}$  and the attenuation are plot over frequency for all three concrete specimen. One can see that for specimen 1 (relatively large aggregates) the result is very satisfying. For the other two specimens there is a deviation between the numerical solution and the experiment, the trend of all curves however is correct. It should be noted that velocity measurements in concrete have a high uncertainty (see Section 7.2) so the deviations do not only stem from the model but also from the experimental difficulties. Note that the experimental data provided did not have error-bar information for specimen 2.

In summary, the functionality of the model can be attested in the investigated frequency range for limited volume fractions.

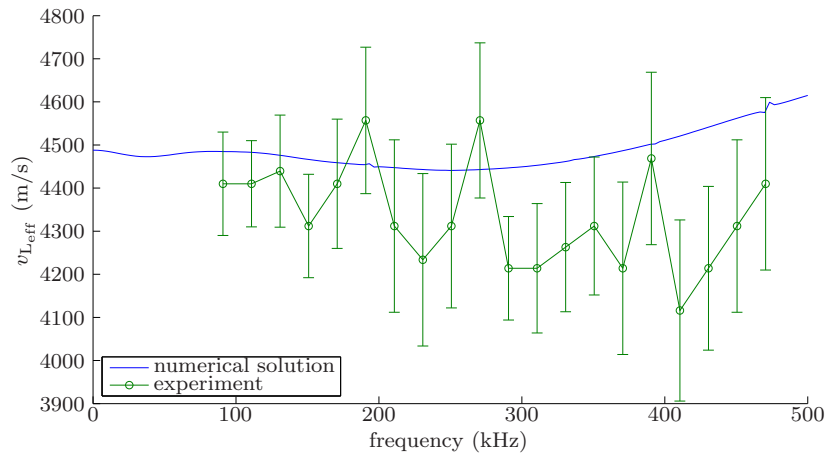


**Figure 7.27:** Longitudinal wave speed of concrete specimen 1

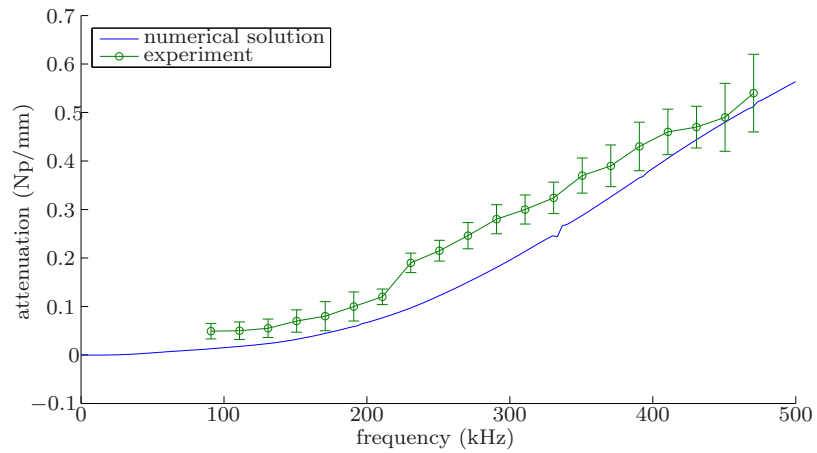


**Figure 7.28:** Attenuation of concrete specimen 1

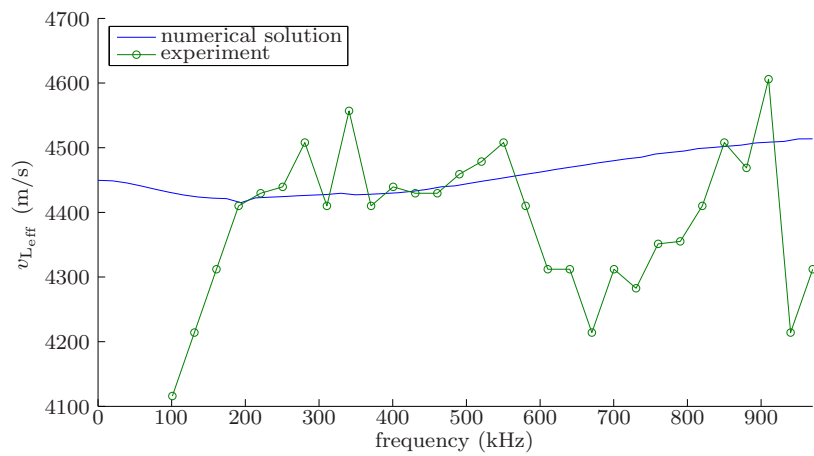


**Figure 7.29:** Longitudinal wave speed of concrete specimen 2

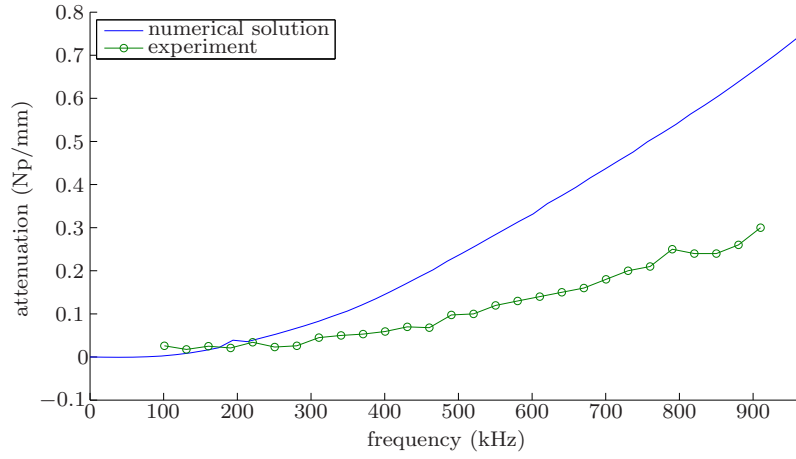


**Figure 7.30:** Attenuation of concrete specimen 2

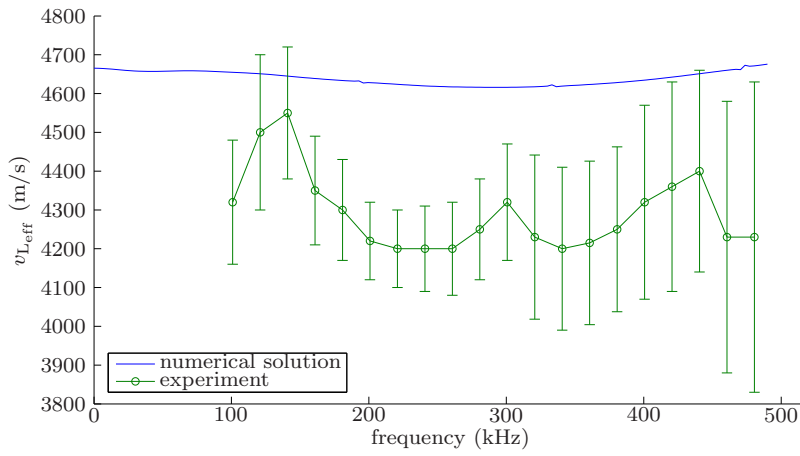


**Figure 7.31:** Longitudinal wave speed of concrete specimen 3

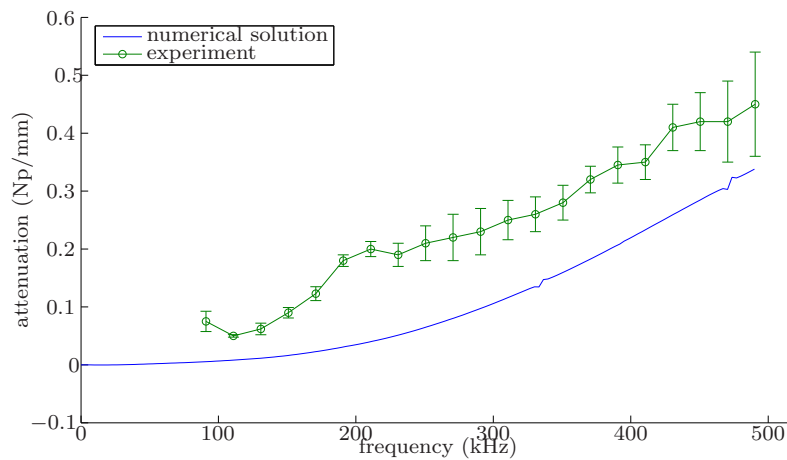


**Figure 7.32:** Attenuation of concrete specimen 3

## CHAPTER VIII

### CONCLUSIONS AND OUTLOOK

#### *8.1 Diffuse measurements*

##### 8.1.1 Conclusion

The research presented in this thesis shows that it is possible to determine diffusivity and dissipation in concrete samples in a reliable and reproducible way and to use the parameter  $D$  to detect microcrack damage. A fixture is designed that ensures consistent coupling conditions and enables spatial averaging of recovered parameters  $D$  and  $\sigma$  from several measurements with the same source-receiver distance.

Two different solutions of the diffusion equation are used for the recovery of the parameters via a curve fitting procedure. Both models show identical qualitative trends even though the simpler 2D model shows higher robustness, presumably due to its simplicity.

The diffusivity values show a clear trend of decreasing with increasing microcrack damage. At the same time, the dissipation stays always roughly the same. Both phenomena are in agreement with the theory that increased scattering slows down the diffusion process (decreasing  $D$ ), while the intrinsic absorption is not influenced by damage but only by the amount of paste material. This also shows one of the main advantages of the diffuse method: the ability to separate between dissipation losses from scattering attenuation. Becker [4] was not able to detect microcrack damage so the present investigation is an important new development, although it must be stated that this research had access to superior measurement equipment.

Several limitations of the diffuse method that are present so far have been observed. The successful application requires a high signal-to-noise ratio to guarantee

reliable curve fitting, a point-like receiver is necessary to avoid phase cancellation which in turn decreases the signal-to-noise ratio, and the geometry of the specimen has to be carefully chosen. The sample cannot be too large, otherwise intrinsic absorption will be too large, and it must not be too small or the wave field cannot be assumed to be fully diffuse. So far, this limits the method to short range detection of damage.

In contrast, due to insufficient sensitivity, this research was unable to detect microcrack damage in concrete.

In conclusion, this research provides first promising results in the detection of microcracks in concrete and gives an understanding of the important necessary steps and the difficulties that come with the method.

### **8.1.2 Outlook**

Since the method proves to be capable of detecting microcracks, future work should concentrate on improving the experiment and eventually take the experiment to the field.

The method should be applied to samples of different geometries to show a more general applicability. One possibility would be the use of plate like concrete samples which would fully justify the use of the simple 2D model. Also generally bigger samples should be employed. This will require improvements on the receiving side to still achieve a high enough signal-to-noise ratio, maybe in the form of the optimization of the cone material and geometry.

Attempts should be made to use a laser interferometer on the receiving side. This would enable true point-like detection and would also eliminate coupling effects that will always be present using ultrasonic contact transducers. Unfortunately, a laser system was not at hand for this research and therefore could not be tested yet.

Another interesting step would be the automatization of the measurements to increase the available data. This would primarily include an automatic detection of optimal curve fitting intervals and weighting intervals for the curve fitting procedure since the tweaking of these time intervals is difficult and cumbersome. Comparisons would have to be made to see if the use of laser interferometer – thus making it unnecessary to clamp the fixture for the transducer at every measurement point – might speed up taking multiple measurements at different points. The automatization would allow to drastically increase the measurement data for every sample to get even more reliable results and higher accuracy for the recovered parameters.

Improvements might also be possible for the curve fitting, e.g. a more realistic modelling of the source term, an optimized selection of the weighting intervals or investigating the influence of single terms in the 3D solution to optimize the number of terms used in the curve fitting procedure. All these might lead to smaller error bars for the nonlinear curve fits.

It would be very interesting to try to determine the diffusivity  $D$  using a different method. One method that has been proven to be able to do that is the coherent backscattering. Its applicability was shown in a 2D medium (parallel steel rods) [41] and a transfer to concrete samples should be attempted.

## ***8.2 Effective medium theory***

### **8.2.1 Conclusion**

The research presented in this thesis gives an extension of a two-phase theory to a multi-phase theory and shows that assuming the matrix material to be a source of scattering is valid. For two-phase materials and some multi-phase samples, there is good agreement between theory and experimentally determined data in the frequency range of the used experimental data. However, there are problems encountered when the inclusion volume fraction is increased above a certain level, which depends on

the material properties of matrix and inclusion material. Also, in some cases, only trends of effective parameters agreed between numerically determined data and the experiment. An exact reason has yet to be determined.

### **8.2.2 Outlook**

As mentioned before, the theory shows some numeric flaws, the source of which is unknown so far, so future research should concentrate on minimizing boundaries on volume fractions of inclusions. Also it should be attempted to improve the model to fit experimental data more closely. In addition, more experimental data of multi-phase materials besides concrete would be very useful to verify or enhance the derived model. Measurements for higher frequencies would be necessary to compare the frequency range of the theory of this research. An important goal should also be a physical interpretation of complex-valued material properties like density, shear modulus and bulk modulus.

## REFERENCES

- [1] ACHENBACH, J. D., *Wave propagation in elastic solids*. North-Holland, 1975.
- [2] ANUGONDA, P., WIEHN, J. S., and TURNER, J. A., “Diffusion of ultrasound in concrete,” *Ultrasonics*, vol. 39, pp. 429–435, 2001.
- [3] ASTM-INTERNATIONAL, “Standard test method for determination of length change of concrete due to alkali-silica reaction c 1293 08b,” 2008.
- [4] BECKER, J., JACOBS, L. J., and QU, J., “Characterization of cement-based materials using diffuse ultrasound,” *Journal of Engineering Mechanics*, vol. 129, pp. 1478–1484, 2003.
- [5] BECKER, J., “Investigation of the microstructure of heterogeneous materials using ultrasonic waves,” Master’s thesis, Georgia Institute of Technology, Aug. 2002.
- [6] BEDFORD, A. and DRUMHELLER, D. S., *Introduction to elastic wave propagation*. Wiley, 1994.
- [7] CARSLAW, H. S. and JAEGER, J. C., *Conduction of heat in solids*. Clarendon, Oxford, 1990.
- [8] CHEN, X. J., KIM, J.-Y., KURTIS, K. E., QU, J., SHEN, C. W., and JACOBS, L. J., “Characterization of progressive microcracking in portland cement mortar using nonlinear ultrasonics,” *NDT&E International*, vol. 41, pp. 112–118, 2008.
- [9] COWAN, M. L., BEATY, K., PAGE, J. H., LIU, Z., and SHENG, P., “Group velocity of acoustic waves in strongly scattering media: Dependence on the volume fraction of scatterers,” *Physical Review E*, vol. 58, no. 5, pp. 6626–6636, 1998.
- [10] DATTA, S. K., LEDBETTER, S. K., and SHINDO, Y., “Phase velocity and attenuation of plane elastic waves in a particle-reinforced composite medium,” *Wave Motion*, vol. 10, pp. 171–182, 1988.
- [11] DUGMORE, K., JONSON, D., and WALKER, M., “A comparison of signal consistency of common ultrasonic couplants used in the inspection of composite structures,” *Composite Structures*, vol. 58, pp. 601–603, 2002.
- [12] ERINGEN, A. C. and SUHUBI, E. S., *Elastodynamics, vol. II*. Academic Press, 1975.
- [13] GRAFF, K. F., *Wave motion in elastic solids*. Dover publications, 1975.

- [14] HILL, J. M. and DEWYNNE, J. N., *Heat conduction*. Blackwell Scientific Publications, 1987.
- [15] KANAUN, S. K. and LEVIN, V. M., “Propagation of longitudinal elastic waves in composites with a random set of spherical inclusions (effective field approach),” *Archive of Applied Mechanics*, vol. 77, pp. 627–651, 2007.
- [16] KANAUN, S. K., LEVIN, V. M., and SABINA, F. J., “Propagation of elastic waves in composites with random set of spherical inclusions (effective medium approach),” *Wave motion*, vol. 40, pp. 69–88, 2004.
- [17] KIM, B.-C. and KIM, J.-Y., “Characterization of ultrasonic properties of concrete,” *Mechanics Research Communication*, vol. 36, pp. 207–214, 2009.
- [18] KIM, J.-Y., “Extinction of elastic wave energy due to scattering in a viscoelastic medium,” *International Journal of Solids and Structures*, vol. 40, pp. 4319–4329, 2003.
- [19] KIM, J.-Y., IH, J.-G., and LEE, B.-H., “Dispersion of elastic waves in random particulate composites,” *Journal of the Acoustical Society of America*, vol. 97, no. 3, pp. 1380–1388, 1995.
- [20] KINRA, V. K., KER, E., and DATTA, S. K., “Influence of particle resonance on wave propagation in a random particulate composite,” *Mechanics Research Communications*, no. 9, pp. 109–114, 1982.
- [21] KURTIS, K. E. and MONTEIRO, P. J. M., “Chemical additives to control expansion of alkali-silica reaction gel: proposed mechanisms of control,” *Journal of Materials Science*, vol. 38, pp. 2027–2036, 2007.
- [22] KUTNER, M. H., NACHTSHEIM, C. J., NETER, J., and LI, W., *Applied Linear Statistical Methods Fifth Edition*. McGraw-Hill, 2005.
- [23] MAESS, J., “Attenuation models for material characterization,” Master’s thesis, Georgia Institute of Technology, Nov. 2004.
- [24] MALVERN, L. E., *Introduction to the Mechanics of a Continuous Medium*. Prentice Hall, 1969.
- [25] MAMLOUK, M. S. and ZANIEWSKI, J. P., *Materials for Civil and Construction Engineers Second Edition*. Prentice Hall, 2006.
- [26] MEHTA and MONTEIRO, *Concrete – microstructure, properties, and materials*. McGraw-Hill, 1993.
- [27] MOLYNEUX, J. B. and SCHMITT, D. R., “Compressional-wave velocities in attenuating media: A laboratory physical model study,” *Geophysics*, vol. 65, no. 4, pp. 1162–1167, 2000.

- [28] MURA, T., *Micromechanics of defects in solids*. Kluwer Academic Publishers, 1987.
- [29] OPPENHEIM, A. V. and SCHAFER, R. W., *Discrete-time signal processing*. Prentice Hall, 1999.
- [30] OWINO, J. O. and JACOBS, L. J., “Attenuation measurements in cement-based materials using laser ultrasonics,” *Journal of Engineering Mechanics*, vol. 125, no. 6, pp. 637–647, 1999.
- [31] PAGE, J. H., SCHRIEMER, H. P., BAILEY, A. E., and WEITZ, D. A., “Experimental test of the diffusion approximation for multiply scattered sound,” *Physical Review E*, vol. 52, no. 3, pp. 3106–3114, 1995.
- [32] PAGE, J. H., SCHRIEMER, H. P., JONES, I. P., SHENG, P., and WEITZ, D. A., “Classical wave propagation in strongly scattering media,” *Physica A*, vol. 241, pp. 64–71, 1997.
- [33] PAYAN, C., GARNIER, V., and MOYSAN, J., “Applying nonlinear resonant ultrasound spectroscopy to improving thermal damage assessment in concrete,” *Journal of the Acoustical Society of America*, vol. 121, no. 4, pp. EL125–EL130, 2007.
- [34] PUNURAI, W., JARZYNSKI, J., QU, J., KURTIS, K. E., and JACOBS, L. J., “Characterization of dissipation losses in cement paste with diffuse ultrasound,” *Mechanics Research Communications*, vol. 34, pp. 289–294, 2007.
- [35] RAMAMOORTHY, S. K., KANE, Y., and TURNER, J. A., “Ultrasound diffusion for crack depth determination in concrete,” *Journal of the Acoustical Society of America*, vol. 115, no. 2, pp. 523–529, 2004.
- [36] R.L.WEAVER, “Ultrasonic diffuse field measurements of grain size,” in *Non-destructive testing and evaluation in manufacturing and construction* (REIS, H., ed.), pp. 425–434, Hemisphere, New York, 1990.
- [37] ROSE, J. L., *Ultrasonic waves in solid media*. Cambridge University Press, 1999.
- [38] SCHRIEMER, H. P., COWAN, M. L., PAGE, J. H., SHENG, P., LIU, Z., and WEITZ, D. A., “Energy velocity of diffusing waves in strongly scattering media,” *Physical Review Letters*, vol. 79, no. 17, pp. 3166–3169, 1997.
- [39] SHENG, P., *Introduction to wave scattering, localization and mesoscopic phenomena*. Academic Press, 1995.
- [40] THOMAS, M. D. A., FOURNIER, B., FOLLIARD, K. J., IDEKER, J. H., and RESENDEZ, Y., “The use of lithium to prevent or mitigate alkali-silica reaction in concrete pavements and structures,” Tech. Rep. FHWA-HRT-06-133, U.S. Department of Transportation Federal Highway Administration, March 2007.

- [41] TOURIN, A., DERODE, A., ROUX, P., VAN TIGGELEN, B. A., and FINK, M., “Time-dependent coherent backscattering of acoustic waves,” *Physical Review Letters*, vol. 79, no. 19, pp. 3637–3639, 1997.
- [42] V.N.KOZLOV, V.G.SHEVALDYKIN, and N.N.YAKOVLEV, “Experimental determination of the attenuation of an ultrasonic wave in concrete,” *Scientific Research Institute for NDT, Moscow*, no. 2, pp. 67–75, 1988.
- [43] WEAVER, R. L., “Diffusivity of ultrasound in polycrystals,” *Journal of the Mechanics and Physics of Solids*, vol. 38, no. 1, pp. 55–86, 1990.
- [44] WEAVER, R. L., “Ultrasonics in an aluminum foam,” *Ultrasonics*, vol. 36, pp. 435–442, 1998.
- [45] WEAVER, R. L. and SACHSE, W., “Diffusion of ultrasound in a glass bead slurry,” *Journal of the Acoustical Society of America*, vol. 97, pp. 2094–2102, 1995.
- [46] ZHANG, Z. Q., JONES, I. P., SCHRIEMER, H. P., PAGE, J. H., WEITZ, D. A., and P.SHENG, “Wave transport in random media: the ballistic to diffusive transition,” *Physical Review E*, vol. 60, no. 4, pp. 4843–4850, 1999.